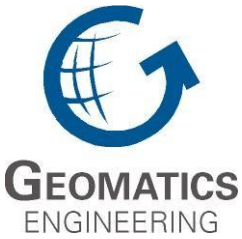

UCGE Reports
Number 20343

Department of Geomatics Engineering

WAAS Integrity Investigation for Canadian Latitudes

(URL: http://www.geomatics.ucalgary.ca/graduatetheses)

by

Oday Haddad

November 2011

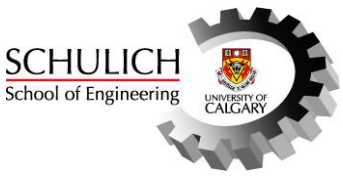

UNIVERSITY OF CALGARY

WAAS Integrity Investigation for Canadian Latitudes

by

Oday Haddad

A THESIS

SUBMITTED TO THE FACULTY OF GRADUATE STUDIES

IN PARTIAL FULFILMENT OF THE REQUIREMENTS FOR THE

DEGREE OF MASTER OF SCIENCE

DEPARTMENT OF GEOMATICS ENGINEERING

CALGARY, ALBERTA

November, 2011

Abstract

The WAAS provides satellite-based augmentation of GPS for commercial aviation applications over the CONUS, Hawaii, Puerto Rico, Alaska, Canada and Mexico. The WAAS provides satellite clock, satellite orbit and ionospheric corrections for GPS users. NAV CANADA is working to implement the Canadian WAAS which will offer seamless service with the current WAAS. A concern for Canadian implementation, however, is the overall limited number of stations in the Canada, and the nature of ionospheric phenomena which may develop at higher latitudes. Therefore, to be able to evaluate WAAS performance at the Canadian latitudes during highly active ionospheric periods, Canadian ionospheric conditions must be simulated to determine if WAAS methods will provide the necessary integrity at Canadian latitudes. The ionospheric delays from 29 WRSs provided as input to the WAAS algorithm to obtain estimated ionospheric delays and associated error bounds. Both the current planar fit and future kriging methods are used.

Acknowledgment

The work presented in this thesis could not have been possible without the technical advice and support from many people.

Special appreciation to my supervisor, Dr. Susan Skone, for her continued support and great counseling throughout my study period and for giving me the chance to work on this project. I would also like to thank Dr. Lawrence Sparks of NASA JPL for generating the WAAS output for the simulated ionospheric observations provided while resident at University of Calgary, and for his assistance and participation in this project.

I would like to thank my friend and my colleague, Ossama Al-Fanek, for all his support, help, and technical assistance during the past three years in any way I needed. You are awesome!

There are lots of people in different places over this world who never failed to support and encourage me every day during the past three years, Ghena Azar, Hisham Thainat, Tarek Kan'an, Rawad Haddad, Remi Saadoun, Qais Marji, Mohannad Al-Durgham, Eunju Kwak, Fatemeh Ghafoori, Hazim Haddad, Dhaedel Rashdan, Thaer Shunnar, Ala'a Kassab, Derar Alassi, Rajesh Tiwari, and Mohammed Sadeque. Thank you is not enough. You are unique!

At last but not least, three people, without them I would never be the one who I am, three people were with me all the time, holding my hands and supporting me in an ultimate and superb way, giving me love and friendship, my Mom, my Dad, and my brother Ala'a, everything belongs to you. Much love!

Dedication

To my parents Issam and Kamilia, and to my brother Ala'a.

Table of Contents

List of Tables

List of Figures

List of Abbreviations

Abbreviation	Definition
C/A	Coarse Acquisition Code
CONUS	Contiguous United States
DGPS	Differential Global Positioning System
DoD	Department of Defense
DOP	Dilution of Precision
FAA	Federal Aviation Administration
FC	Fast Correction
GDOP	Geometric Dilution of Precision
GEO	Geostationary Earth Orbit
GES	Ground Earth Station
GIVE	Grid Ionospheric Vertical Error
GPS	Global Positioning System
GNSS	Global Navigation Satellite System
HDOP	Horizontal Dilution of Precision
HPL	Horizontal Protection Level
IGP	Ionospheric Grid Point
IGS	International GNSS Service
IPP	Ionospheric Pierce Point
LADGPS	Local-Area Differential Global Positioning System
LTC	Long Term Corrections
MSC	Master Control Station
PDF	Probability Density Function
PDOP	Position Dilution of Precision
PPS	Precise Positioning Service
PRN	Pseudo Random Noise
PSD	Power Spectral Density
PVT	Positioning, Velocity, and Timing
P(Y)	Precision Code
RMS	Root Mean Square
SAPS	Sub-Auroral Polarization Stream
SBAS	Satellite Based Augmentation System
SED	Storm Enhanced Density
SPS	Standard Positioning Service
STEC	Slant Total Electron Content
TCN	Terrestrial Communication Network
TDOP	Time Dilution of Precision
TEC	Total Electron Content
UDRE	User Differential Range Error
VDOP	Vertical Dilution of Precision

VPL	Vertical protection Level
VTEC	Vertical Total Electron Content
WAAS	Wide Area Augmentation System
WADGPS	Wide Area Differential Global Positioning System
WGS-84	World Geodetic System 1984
WMS	Wide Area Master Station
WRS	Wide Area Reference Station

Chapter One: Introduction

1.1 Background

The Global Positioning System (GPS) is a space-based Global Navigation Satellite System (GNSS) developed since 1973 by the US Department of Defense (DoD) for military uses to provide precise positioning worldwide. The DoD expanded use of the GPS to be freely available for civilians and civil applications continuously worldwide in all weather conditions. The current GPS constellation consists of 31 satellites transmitting navigation signals continuously. GPS receivers receive and process such signals and provide users with positioning and navigation capabilities.

When the signal is transmitted from the satellite, it propagates through the Earth's atmosphere which affects the signal and in turn affects the geometric range measurement and degrades the positioning accuracy. One of the main error sources that degrade positioning accuracy arises from that part of the atmosphere extending approximately 50 to 1500 km above the Earth's surface and called the ionosphere. The ionospheric effect can lead to positioning errors exceeding 100 m. Many methods have been developed to remove the effect of the ionosphere including dual frequency ionospheric corrections, Differential GPS (DGPS), and GPS network modeling.

Due to the dispersive property of the ionosphere, its effect can be removed when using dual frequency GPS receivers by deriving the first order ionospheric delay corrections. Another method (for single frequency users) is DGPS where ionospheric corrections are

generated at a reference station and then transmitted to remote users for correction of the ionospheric effect. This method can be used in local areas (baseline lengths up to 500 km, for example the Canadian Coast Guard marine DGPS service) but not for wide areas. For this purpose, Wide Area DGPS (WADGPS) can be used to remove the ionospheric effect over larger areas of coverage. In WADGPS, a network of dual frequency GPS reference stations (distributed over this wide area) collect GPS observations and estimate spatial models of the ionospheric corrections; these model parameters are broadcast to users for estimation of their local ionospheric errors.

With the substantial growth of GPS use, nowadays great benefits are provided to aviation users for vertical and horizontal positioning. In aviation applications, vertical positioning is the most important consideration. In order to mitigate the effect of GPS ranging errors (such as ionospheric delays) and improve positioning accuracy, the Federal Aviation Administration (FAA) had developed a Satellite Based Augmentation System (SBAS) called the Wide Area Augmentation System (WAAS) with the purpose to augment the GPS and provide sufficient accuracy, reliability, continuity and availability for aviation users during flight phases.

WAAS is a form of WADGPS consisting of a ground based network that includes L1 (1575.42 MHz) and L2 (1227.6 MHz) dual frequency GPS receivers; these stations are referred to as Wide Area Reference Stations (WRSs). Currently, 38 WRSs are located across the Contiguous United States (CONUS), Hawaii, Puerto Rico, Alaska, Canada and Mexico. These WRSs monitor GPS satellites and collect GPS L1 and L2 signal

observations and transmit the measurements to a master station known as Wide Area Master Station (WMSs) through a Terrestrial Communication Network (TCN). These WMSs process the observations sent by WRSs to calculate clock, ephemeris, and ionospheric corrections. In addition to these corrections, WMSs calculate error bounds for the ionospheric corrections called Grid Ionospheric Vertical Errors (GIVEs). Currently the WAAS has three WMS and each one of these stations can perform the WAAS correction and error bound calculations. These correction data are forwarded to a Ground Earth Station (GES) to be uplinked to Geostationary Earth Orbit (GEO) satellites. WAAS currently relies on two GEOs where each one transmits the WAAS message in an L1-signal coded in a similar manner as a GPS satellite C/A code transmission. Aircraft systems which have WAAS receivers receive these corrections and apply them to GPS measurements to remove the ionospheric effect and improve positioning accuracy.

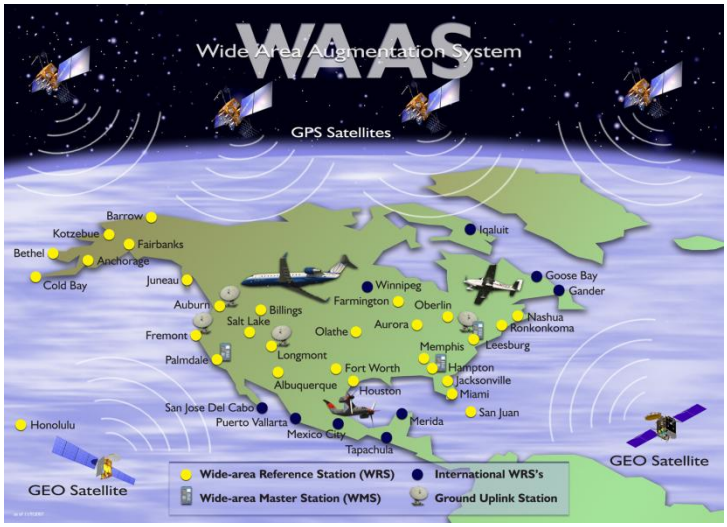

Figure 1.1: Wide Area Augmentation System (WAAS) [http://www.nstb.tc.faa.gov/images/Waaspic.jpg]

In 2004, NAV CANADA announced an agreement with the United States FAA to extend WAAS into Canada (NAV CANADA, 2004). In 2007, four WRS were integrated into the WAAS network (FAA, 2007) to improve the WAAS performance at Canadian and Northwest U.S. latitudes. These four stations located in eastern Canada allow significant improvement in performance during severe ionospheric conditions; users in western Canada however experience minimal benefit for WAAS applications (Yousuf and Skone, 2005).

1.2 Objectives

In October – November 2003, severe geomagnetic storm effects referred to as Storm Enhanced Density (SED) degraded WAAS availability. These ionospheric SED events had a direct impact on WAAS such that the service was not available for extended periods during these storms (Doherty et al., 2004).

In 2004 NAV CANADA announced the intention to extend the FAA operation of WAAS into Canada. The next solar maximum is expected to occur 2013-2014, and the WAAS extension and integrity must be validated under severe ionospheric conditions. The WAAS must be tested for service at Canadian latitudes to determine whether WAAS can meet its requirements during severe ionospheric events. Therefore, a detailed study of SED events (observed in October – November 2003) must be conducted, such that highly challenging ionospheric features similar to the observed SED events may be simulated at Canadian latitudes. Such simulations then allow WAAS accuracy and integrity to be investigated in the presence of severe ionospheric conditions.

It is the overall focus of this thesis to investigate WAAS performance at Canadian latitudes during severe ionospheric conditions. The work has the following primary goals:

1) Develop tools for realistic simulation of ionospheric events in the Canadian region.
2) Investigate and test WAAS performance under various ionospheric conditions within Canada.

1.3 Thesis Outline

This thesis contains seven chapters. Chapter 1 provides background and objectives.

Chapter 2 provides an overview of GPS, GPS observables, and the error sources that affect observations and degrade positioning accuracy.

In Chapter 3, a review of the ionosphere, the ionospheric phenomena and its physical properties is provided. This chapter also focuses on derivation of the ionospheric delay and the effect of the ionosphere on GPS observations.

Chapter 4 provides an overview of WAAS and its basic components. Description of WAAS delay and error bounds estimation is provided using planar fit and kriging models. Additionally, a review of undersampling threat and WAAS availability and integrity requirements are included.

Chapter 5 provides analysis of a specific ionospheric geomagnetic storm effect referred to as SED. A detailed study of this storm effect is conducted with estimation of spatial

characteristics and temporal evolution over Northern America. A simulation capability is developed. This tool is used to generate different ionospheric activities at different locations for investigation of WAAS performance.

Chapter 6 investigates WAAS performance for the simulated ionospheric activities over the Canadian latitudes. Planar fit and kriging models are used for this investigation. From each model, the estimated delays, the error bounds and the Vertical protection Level (VPL) are obtained and analysed for four different ionospheric activity scenarios.

Finally, Chapter 7 presents conclusions and recommendations of this work.

Chapter Two: Global Positioning System

2.1 GNSS Service

Global Navigation Satellite Systems (GNSS) are satellite navigation systems that provide autonomous geo-spatial positioning with global coverage. The United States developed its own GNSS which is called the Global Positioning System (GPS) and was declared operational in April 1995. Currently there are many GNSS which are operational or under development and deployment. For example, Russia developed an alternative to the GPS called The Russian Global Navigation Satellite System (GLONASS) launched in the early 1980s. The European Union is deploying a stand-alone navigation system that will be inter-operable with GPS and GLONASS called GALILEO. Indian Regional Navigational Satellite System (IRNSS) is another regional satellite navigation system being developed by the Indian Space Research Organization. Generally, many GNSS systems are in operation or deployed to provide accurate positioning for many civilian or military applications.

2.2 Global Positioning System (GPS)

Global Positioning System (GPS) provides two kinds of service: 1) Standard Positioning Service (SPS) for civil use and 2) Precise Positioning Service (PPS) which is intended for authorized users by DoD. GPS consists of three segments: Space segment, Control Segment, and User segment. The DoD is responsible for the first two segments while the user segment is controlled by market forces (Misra and Enge, 2006).

2.2.1 Space Segment

The space segment is the constellation of GPS satellites which are positioned in six nearly circular orbits around the earth at altitudes approximately 26,560 km. Each orbit inclined at 55^{o} to the equatorial plane and is separated by 60^{o}. Every orbit has an 11 hours and 58 minutes period such that each satellite orbits the earth twice every day. Currently, the GPS constellation consists of 31 active satellites (USNO, 2011) which guarantees that all users have a minimum of 4 satellites in view which is the minimum number of satellites required to calculate a three-dimensional positioning solution.

2.2.2 Control Segment

The control segment consists of three elements: Master Control Station (MCS), monitor stations, and ground antennas. The control segment has many functions including monitoring satellite orbits to maintain each satellite in its proper orbit, maintaining GPS time, predicting satellite ephemeris and clock parameters, and updating the GPS navigation message (Misra and Enge, 2006).

2.2.3 User Segment

This GPS segment is referenced to the GPS receiver which is the equipment used to determine position, velocity, and time. Each GPS receiver consists of five components: antenna, receiver, processor, input/output device, and power supply. The satellite signals are received by the antenna and the receiver extracts the navigation message which is used by the processor to compute PVT. Also, the processor controls the receiver through

its operations starting from signal acquisition to signal tracking and estimation of ranging observations. The input/output device is used to display the solution parameters (Kaplan and Hegarty, 2006).

2.3 GPS Signal Structure

Currently, GPS signals are transmitted on multiple radio frequency signals referred as L1 (f_{L1}=1575.42 MHz), L2 (f_{L2}=1227.6 MHz), and L5 (f_{L5}=1176.45 MHz). The GPS signal consists of three components transmitted on each GPS signal: the carrier wave with frequencies f_{L1}, f_{L2} or f_{L5}, the navigation data message which is uploaded from the MSC to the satellite, and the Pseudo Random Noise (PRN) code sequence modulated onto the carrier wave and the navigation message. Each satellite has two unique codes called the Coarse Acquisition Code (C/A) for civilian use and encrypted Precision Code referred to as P(Y) code for military signals.

The C/A code which is referred to as the PRN code is modulated onto L1 frequency signals. The C/A code is a sequence of 1023 chips repeated every 1 ms giving a chipping rate of 1.023MHz. Since each GPS satellite has its own PRN code, this will allow the receiver to determine the satellite that transmits the data. The P(Y) code is onto the L1 and L2 frequencies with a higher chipping rate of 10.23 MHz.

In late 1990's, GPS modernization was launched with plans called for new civil signals to benefit the civil users. The two new planned signals called L2C and L5. L2C signals have a carrier frequency of 1227.6 MHz as L2 signal with two inter-multiplexed codes. The

chipping rate of L2C signals is 1.023 MHz as the C/A code in L1 signals. Currently, there are eight satellites transmitting L2C signal on L2 frequency (USNO, 2011). The planned L5 signals have a carrier frequency of f_{L5}=1176.45 MHz with chipping rate of 10.23 MHz (Misra and Enge, 2006).

The L1 signal transmitted from the satellite can be written mathematically as:

$$S_{L1}^{(k)}(t) = \sqrt{2P_C}\; X^{(k)}(t)\, D^{(k)}(t)\; \cos(2\pi f_{L1} t + \theta_{L1}) + \sqrt{2P_Y}\; Y^{(k)}(t)\, D^{(k)}(t) \sin(2\pi f_{L1} t + \theta_{L1}) \quad (2.1)$$

where:

P_C, P_Y	are the C/A and P(Y) code power on L1 signal
$X^{(k)}$, $Y^{(k)}$	are the C/A and P(Y) codes of the k^{th} satellite
f_{L1}	is the L1 frequency (1575.42 MHz)
θ_{L1}	is the phase shift of the carrier wave
$D^{(k)}(t)$	is the navigation data message of the k^{th} satellite

The GPS navigation message consists of 25 frames and each frame consists of 5 subframes. Each subframe consists of 10 words and each word is 30 bits of data. Since the bit rate of the navigation message is 50 bps, 750 seconds are required to observe one navigation message. The first subframe in each frame contains GPS week number, satellite accuracy and health, age of data and satellite clock corrections. Subframe 2 and 3 contain the orbital parameters while subframes 4 and 5 (which have 25 pages) contain

almanac data, ionospheric model, satellite health, configuration flag for all the satellites, and other messages (IS-GPS-200, 2010).

2.4 GPS Observables

In general, GPS provides three types of observation measurements: pseudorange, carrier phase, and Doppler.

2.4.1 Pseudorange Measurements

The pseduorange measurements are derived from the PRN code by determining the time offset between the transmitted and the replica generated in the receiver. This time offset represents the propagation time of the signal (satellite to receiver). Multiplying this offset time by the speed of light in a vacuum defines the pseudorange. This measurement is called pseudorange because it is biased by the synchronization offset between satellite and receiver clocks.

Pseudorange observation equation is given by

$$P = \rho + d\rho + c(dt - dT) + d_{ion} + d_{trop} + \varepsilon_P \qquad \text{(in meter)} \tag{2.2}$$

where:

ρ is the geometric range between the satellite and receiver antenna (m)

$d\rho$ is the satellite orbit error (m)

c is the speed of light (m/sec)

dt is the satellite clock error (seconds)

dT is the receiver clock error (seconds)

d_{ion} is the ionospheric delay error (m)

d_{trop} is the tropospheric delay error (m)

ε_P is the receiver code noise and code multipath (m)

2.4.2 Carrier Phase Measurements

This measurement is determined by the phase difference between the received signal from GPS satellite to receiver and the signal generated in the receiver. The carrier phase range is derived by scaling carrier phase in cycles by the signal wavelength in a vacuum. Carrier phase measurements result in more precise observations than the pseudorange in terms of noise and multipath errors.

Since the receiver cannot distinguish between cycles of the received carrier wave, the receiver measures only the fractional phase. The absolute range measurement would be this measured fractional cycle plus the unknown number of whole cycles. This unknown number of cycles is an integer value and is referred to as the carrier phase ambiguity.

Carrier phase observable equation is given as

$$\Phi = \rho + d\rho + c(dt - dT) - d_{ion} + d_{trop} + \varepsilon_\Phi + \lambda N \qquad \text{(in meter)} \tag{2.3}$$

where:

ρ is the geometric range between the satellite and receiver antenna (m)

$d\rho$ is the satellite orbit error (m)

c is the speed of light (m/sec)

dt is the satellite clock error (seconds)

dT is the receiver clock error (seconds)

d_{ion} is the ionospheric delay error (m)

d_{trop} is the tropospheric delay error (m)

ε_{Φ} is the receiver carrier noise and carrier phase multipath (m)

λ is the carrier wavelength (m)

N is the integer ambiguity (cycles)

2.4.3 Doppler Measurements

The Doppler effect is defined as the frequency shift of the signal due to the relative motion between the transmitter and the receiver. Therefore, due to the relative motion between GPS satellite and receiver, the rate of change in the carrier phase can be measured. This measurement is called the Doppler measurement. In other words, the Doppler measurement is the time derivative of the phase observation.

The relative velocity between the satellite and the receiver can be evaluated by multiplying the Doppler measurement by the wavelength.

The Doppler observation equation is given as

$$\dot{\Phi} = \dot{\rho} + d\dot{\rho} + c\left(d\dot{t} - d\dot{T}\right) - \dot{d}_{ion} + \dot{d}_{trop} + \varepsilon_{\dot{\Phi}} \quad \text{(in meter per second)} \tag{2.4}$$

where:

$\dot{\rho}$ is the geometric range rate between the satellite and receiver antenna (m/s)

$d\dot{\rho}$ is the satellite velocity error (m/s)

c is the speed of light (m/s)

$d\dot{t}$ is the satellite clock drift error (s/s)

$d\dot{T}$ is the receiver clock drift error (s/s)

$\dot{d}_{ion}$ is the ionospheric error drift (m/s)

$\dot{d}_{trop}$ is the tropospheric error drift (m/s)

$\varepsilon_{\dot{\Phi}}$ is the Doppler multipath rate of change and other Doppler errors (m/s)

2.5 GPS Error Sources

GPS signals are affected by different error sources from the satellite, receiver, and the propagation medium. These errors can be classified as correlated errors such as the ionospheric error and non-correlated such as the clock biases, receiver noise, and multipath. The following sections discuss the main GPS errors.

2.5.1 Satellite Based Errors

Many errors at the satellite affect GPS measurements which then degrade computed position accuracies. Errors originating at the satellites include the ephemeris (or orbital) and satellite clock errors.

2.5.1.1 Ephemeris Errors

The GPS control segment broadcasts the ephemerides which are predicted based on previous GPS observations. This prediction may cause some errors in estimating the satellite positions and velocity which are known as ephemeris errors. The ephemeris data are included in subframes 2 and 3 of the navigation message to compute satellite position and velocity. Satellite ephemeris errors will affect the position accuracy. Nominally the ephemeris errors are less than 10 m (1σ) (Gleason and Gebre-Egziabher, 2009).

2.5.1.2 Satellite Clock Errors

Each GPS satellite has an atomic clock which is extremely accurate and controlled by the control segment of GPS system. However, the satellite clock suffers from a drift with

respect to the GPS time. The master control station calculates clock corrections which are transmitted to the satellite and rebroadcast in the navigation message. Satellite clock corrections are determined using Equation (2.5)

$$\delta t_{clk} = a_{f_0} + a_{f_1}(t - t_{oc}) + a_{f_2}(t - t_{oc})^2 + \Delta t_r \quad (2.5)$$

where:

a_{f_0} is the clock bias (s)

a_{f_1} is the clock drift (s/s)

a_{f_2} is the frequency drift (s/s^2)

t_{oc} is the clock data reference time (s)

t is the current time epoch (s)

Δt_r is the correction due to relativistic effects (s)

The above equation is used to estimate the actual satellite clock error; however, some residual error remains which varies from 0.3-4 m beside the clock type and the age of the broadcast data (Kaplan and Hegarty, 2006).

2.5.2 Propagation Errors

The GPS signal is an electromagnetic wave affected by the propagation medium. As the GPS signal travels towards the earth, it propagates through the earth's atmosphere. The atmosphere consists of two main regions of interest for GPS: the ionosphere and the neutral atmosphere (primarily troposphere). While the signal propagates through the atmosphere, the signal velocity changes due to the medium characteristics. This is characterized as refraction. Variations in the signal velocity change the propagation time

of the signal which is the basic GPS measurement used to calculate position. This variation in travel time (satellite to receiver) becomes an error in ranging observations and in positioning accuracy. This type of error is referred to as propagation error.

2.5.2.1 Tropospheric Errors

In GPS, the troposphere is the neutral part of the atmosphere that extends up 40 km above the earth's surface which causes attenuation, delay, and random rapid variation (scintillation) of the GPS signals. The magnitude of the tropospheric errors depends on many factors such as temperature, pressure, water vapour, time, and satellite elevation angle. The troposphere is a non-dispersive medium at GPS frequencies which means that the effect of the medium is independent of signal frequency.

The tropospheric propagation error is usually expressed as a function of the wet and dry delays. Mathematically, the tropospheric delay is given as

$$d_{trop} = d_{dry}.m_{dry} + d_{wet}.m_{wet} \tag{2.6}$$

where:

d_{dry} , d_{wet} are the dry and wet delays represented at zenith

m_{dry} , m_{wet} are the mapping function to map the zenith delay to the slant direction of satellite-receiver line-of-sight

The tropospheric path delay is calculated based on the refractive index of the troposphere and can be written as

$$d = \int (n-1) ds \tag{2.7}$$

where n is the refractive index of the troposphere and the integration is taken along the path of the signal.

The refractivity is defined as

$$N = 10^6 (n-1) \tag{2.8}$$

The tropospheric refractivity N is separated into dry and wet parts and can be written as

$$N = N_{dry} + N_{wet} \tag{2.9}$$

where:

N_{dry} is the dry refractivity

N_{wet} is the wet refractivity

The dry refractivity depends on the temperature and the partial pressure of the air due to dry gases, while the wet refractivity depends on the temperature and the water vapour pressure. The wet delay represents 10% of the total tropospheric delay where the dry delay represents 90% of the total delay. Therefore, Equation (2.6) becomes

$$d_{trop} = \left(10^{-6} \int N_{dry} ds\right).m_{dry} + (10^{-6} \int N_{wet} ds).m_{wet} \tag{2.10}$$

The tropospheric delay range error can be estimated using different tropospheric models developed for that purpose such as Hopfield model (Hopfield, 1969), Modified Hopfield model (Goad and Goodman, 1974), Black model (Black, 1978), and the Saastamoinen model (Saastamoinen, 1973). The Saastamoinen model performs best between different

models with typical accuracies of 2-4 cm (Skone, 2009) . Under standard atmospheric conditions, the tropospheric zenith delay for GPS signals reaches approximately 2.4 m at sea level, and the slant delay can approach up to 25 m at very low elevation angles (Wielgosz et al., 2011).

2.5.2.2 Ionospheric Errors

This region extends from approximately 50 to 1500 km above the earth's surface and consists of ionized gas (free electrons and ions).

The ionosphere affects propagation of radiowaves such as GPS signals. The dominant component affecting GPS signals is the total number of electrons along the path of propagation commonly known as Total Electron Content (TEC). TEC is defined as

$$TEC = \int_{Rx}^{SV} N_e dl \tag{2.11}$$

where N_e is the electron density along the signal path. The total electron content is measured by units of TEC Unit (TECU) where 1 TECU equals to 10^{16} electrons/m^2.

TEC affects the signal propagation time and causes ranging errors in the GPS measurements. This ranging error is equal in magnitude and opposite in sign for pseudorange and carrier phase measurements. Moreover, unlike the troposphere, the ionosphere is a dispersive medium which allows correction of the first order ionospheric range error. The ionospheric error can be written as

$$I_P = -I_\Phi = \frac{40.3 \cdot TEC}{f^2} \tag{2.12}$$

where:

I_P is the pseudorange ionospheric delay (m)

I_Φ is the carrier phase ionospheric advance (m)

TEC is the Total Electron Content (TECU)

f is the carrier frequency (Hz)

1 TECU becomes 0.16 m delay on L1 and 0.27 m on L2.

Typical values of the ionospheric range error vary from 2 to 10 m in the zenith direction (Misra and Enge, 2006). The magnitude of this error varies according to several factors such as time of the day, time of the year, solar cycle, elevation angle, and user's location.

In addition to the range error, the ionosphere has many other affects on GPS signals such as phase and amplitude scintillation. Ionospheric scintillation is a rapid fluctuation in the GPS signal amplitude and the phase observations due to the presence of irregularities in the ionosphere. Scintillation effects can cause errors in GPS receiver signal acquisition and tracking. Ionospheric scintillation increases errors in the receiver tracking loop causing (in extreme cases) loss of lock on the satellite signal (Humphreys et al., Psiaki and Kintner, 2010) (Béniguel et al., 2011). Scintillations are strongest in the equatorial ($\pm 10^o$-20^o geomagnetic latitude), auroral (65^o-75^o geomagnetic latitude), and polar cap ($>75^o$ geomagnetic latitude) regions (Skone and de Jong, 2000).

More details about ionospheric characteristics and effects on GPS are provided in Chapter 3.

2.5.2.3 Multipath Error

Multipath is the phenomenon where a GPS signal arrives at a receiver's antenna via more than one path. Multipath affects both the pseudorange and carrier phase observations (Xu, 2007).

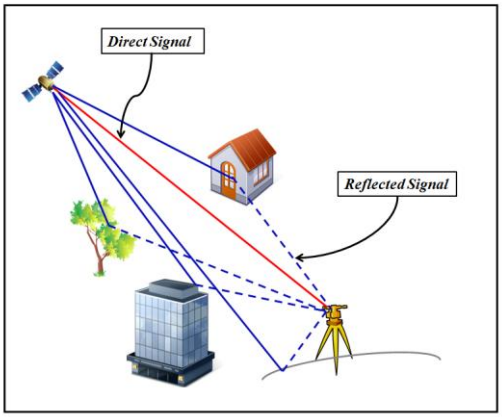

Figure 2.1: Multipath

The effect of multipath depends on the surrounding area where the signal is reflected from different surrounding objects. These objects could be smooth or rough which produce specular or diffuse multipath respectively. In the presence of multipath, the receiver receives a composite signal including the original signal (direct signal) and the reflected signals (indirect signals). The indirect signals are delayed and can suffer from phase shift and/or attenuation. Due to the change in phase and the delay, the signals will interfere resulted in multipath errors of 0.5 to1 m for code measurements and 0.5 to 1 cm for carrier phase measurements (Misra and Enge, 2006), however, multipath errors can

reach to 150 m for pseudorange measurements and 5 cm for the L1 carrier phase measurements (Lachapelle, 2008).

It is difficult to eliminate the effect of multipath; however, many techniques are available to mitigate its effect. Multipath mitigation could be perform by using improved GPS receiver technologies, proper antenna placement, correlations in time, and choosing appropriate site locations (Lachapelle, 2008).

2.5.3 Receiver Based Errors

These errors are receiver-dependent and can be categorized as receiver clock errors and receiver noise.

2.5.3.1 Receiver Clock Errors

The difference between true GPS time and time observed by the receiver oscillator is called receiver clock error. A GPS receiver estimates this timing difference as a fourth unknown parameter in addition to the three position parameters. This error is a function of time due to clock drift which is function of the quality of oscillator used in the receiver to control the clock (Lachapelle, 2008). Different oscillators with different accuracies could be used such as the low-cost quartz clock or more expensive but more accurate oscillators such as temperature compensated crystal oscillator (TCXO), an oven controlled crystal oscillator (OCXO), or Rubidium oscillators.

2.5.3.2 Receiver Noise

At the receiver the GPS observations include random noise generated from the receiver's components such as the antenna, amplifiers, cables, dynamic stress on tracking loops, and the thermal noise. The amount of noise in the receiver determines how precisely the pseudorange and the carrier phase can be measured.

Receiver noise can be estimated using a zero baseline test where the signal is split into two receivers connected to one antenna. Using this test, the precision of the receiver measurements can be verified. Typical values of receiver noise can reach to 0.5 m for pseudorange measurements and 0.2 mm in carrier phase measurement (Misra and Enge, 2006).

2.6 Satellite Geometry

In addition to range measurement error, satellite geometry has an impact on positioning accuracy. The distribution of GPS satellites relative to the user is important for positioning accuracy. The position estimate depends on range accuracy and a term depending on the satellite geometry called Dilution of Precision (DOP) which provides a simple description of the satellite geometry.

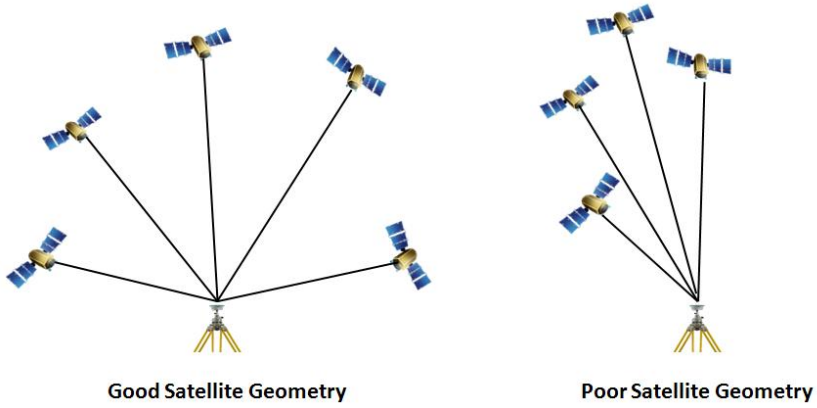

Figure 2.2: Good and poor satellite geometry

Several common DOP parameters are used to characterize the quality of the positioning accuracy such as the Position DOP (PDOP) for 3-D position error, and Time DOP (TDOP) for clock bias error. Combining the 3-D position and clock dilution of precision gives the Geometric DOP (GDOP). Another two terms called VDOP and HDOP are used to estimate error in the vertical (Height) and horizontal (East, North) position components respectively. For example, the RMS of the horizontal error is determined by multiplying the measured RMS error of the pseudorange by the horizontal dilution of precision (HDOP).

2.7 Differential GPS

Many GPS applications require high positioning accuracy such as for aviation and military users. Better positioning accuracy and quality can be achieved through mitigating measurement errors or by increasing the number of satellite observations for better geometry.

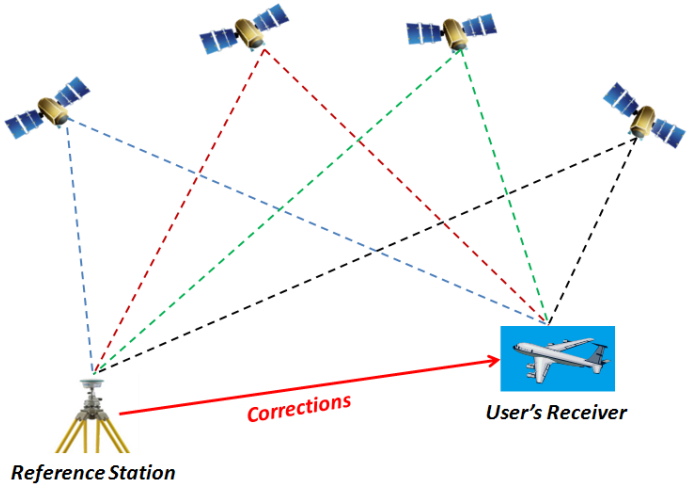

Figure 2.3: Differential GPS

Some of the measurement errors are spatially correlated; therefore, these errors can be mitigated and the positioning accuracy improved by using a technique called Differential GPS (DGPS).

DGPS uses reference stations at known locations where GPS ranging errors are estimated. A given reference station then provides local users information such as error corrections and integrity data; the user applies such information to obtain more accurate positioning estimates.

Two categories can be used to describe DGPS: Local-Area Differential GPS (LADGPS) and Wide-Area Differential GPS (WADGPS). LADGPS and WADGPS are used to describe DGPS systems covering large geographic areas with local-area systems covering areas up to 1000 km while wide-area covering more larger regions (Kaplan and Hegarty, 2006).

2.7.1 Local-Area Differential GPS

In this technique, a network of reference stations at known locations collects GPS measurements and computes ranging corrections for these measurements. These corrections are transmitted to users' receivers which apply these corrections in position computations. The corrections supplied to the user contain ionospheric, satellite clock, and ephemeris corrections which are likely highly correlated between reference and remote receivers. More information about LADGPS can be found in Kaplan and Hegarty, (2006) and Grewal et al., (2007).

2.7.2 Wide-Area Differential GPS

To apply the differential corrections over a continent-wide region, an alternative technique is used referred to as Wide-Area DGPS (WADGPS). As in LADGPS, WADGPS systems collect GPS measurements from a network of reference stations covering the area of interest. This network collects the measurements and computes differential corrections (i.e. the ionospheric, satellite clock, and ephemeris corrections) to be sent to GPS users. WADGPS systems often provide these corrections via geostationary satellite downlinks.

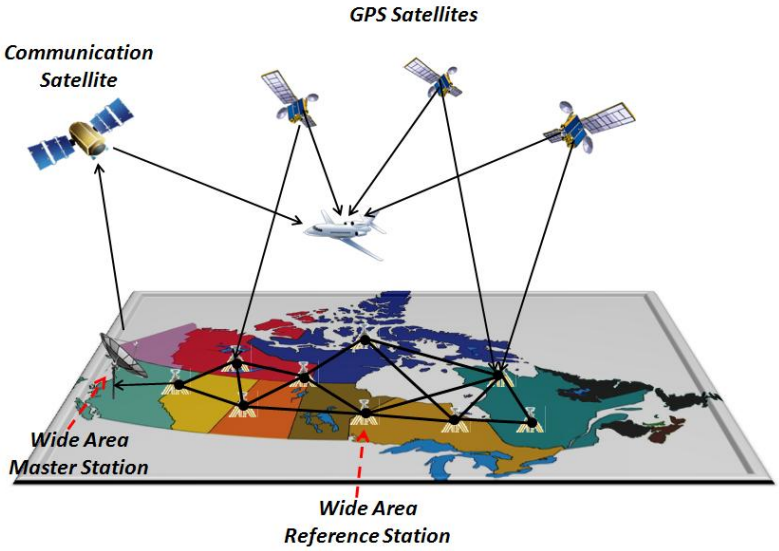

Figure 2.4: Wide Area Differential GPS System

In 2003, Federal Aviation Administration (FAA) developed a WADGPS system called the Wide Area Augmentation System (WAAS) to provide differential GPS corrections over North America via geostationary satellites (FAA, 2011). In order to apply WAAS corrections, the GPS receiver must have the capability to receive these corrections from the geostationary satellites. More details about WAAS system will be discussed in Chapter 4.

Chapter Three: The Ionosphere and Ionospheric Phenomena

3.1 The Ionosphere

The ionosphere is an ionized region of the atmosphere extending approximately 50 to 1500 km above earth's surface. This region contains charged particles which affect propagating radiowave signals. The charged particles are generated by ionization processes in which solar radiation ionizes the neutral atmosphere generating free electrons and positively charged ions. The amount of the ionization is influenced by the amount of sun radiation and properties of the solar wind. The solar wind is a stream of charged particles emitted from the sun at a very high speed. The number of electrons in the ionosphere is proportional to the ionization rate versus recombination rate where the electrons and ions recombine to reform molecules.

Since solar radiation affects the ionization process, the ionospheric electron density varies with time (daily and seasonal variations), solar cycle, and location on earth.

3.1.1 Regions of the Ionosphere

The ionosphere consists of different regions. These regions are classified as D, E, F1, and F2 layers. The lowest region called the D region extends from 50 to 90 km above the earth's surface. This region exists during the day-time and vanishes at night due to recombination of the ions and electrons. This region has minimal impact on GPS users.

The E region extends from 90 to 150 km altitude and has typically lower electron density than the F layers. This region does not vanish at night but remains with lower electron density. Irregularities may develop within this region caused by energetic electron precipitation and it can be called sporadic E layer.

The upper part of the ionosphere is the F layer which extends 150 to 1000 km altitude. This region is divided into two sub-layers: the F1 and F2 sub-layers. The F2 sub-layer has the largest concentration of electrons compared to D, E, and F1 layers. Also, F2 region is the most variable, anomalous, and difficult to predict (Hargreaves, 1992). Because F2 has the largest electron concentration, ionospheric models based on GPS data usually approximate the ionosphere as a thin shell at 350 km altitude. Due to recombination processes, the F1 sub-layer disappears at night and the two sub-layers become one at about the level of the F2 sub-layer.

3.1.2 Solar Cycle

Ionosphere activity is dependent on the sunspot number. Sunspots are dark patches on the Sun's surface caused by intense magnetic fields. The number of sunspots reaches a maximum approximately every 11 years; this periodicity is known as the solar cycle. The solar cycle for the past 50 years is shown in Figure 3.1. The last solar cycle peak occurred in 2001-2002 and the next solar cycle peak expected to be in 2013-2014.

The sunspot variations influence solar emissions and solar flares (enormous releases of electromagnetic energy and particles from the sun). Ionospheric electron density profiles

are therefore highly dependent on the solar cycle. During solar maximum, solar flares increase the density and thickness of the ionosphere which also increases the electron density. This enhancement in the ionospheric electron density will directly affect GPS measurements.

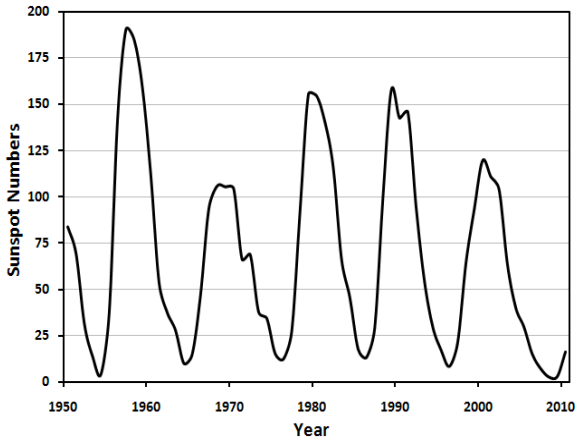

Figure 3.1: Solar cycle sunspot numbers progression

3.1.3 Geomagnetic Storms

During solar maximum, enhanced solar flares increase the occurrence of geomagnetic storms. The geomagnetic storm is a disturbance of the Earth's magnetosphere caused when the solar wind and interplanetary magnetic field interact with the Earth's magnetic field. These geomagnetic storms result in ionosphere perturbations in the low and mid-latitudes - which has a direct impact on GPS measurements. The severity of geomagnetic storms is monitored by geomagnetic indices such as *K, Kp, Ap* and *Dst*.

The *K* index is a number between 0 and 9 scaled from the range of observed fluctuations that indicates the level of disturbance in a given three-hour time interval (Gonzalez et al., 1994) with 0 representing the lowest level of ionospheric activity. The global *Kp* index is

the mean value of all *K* indices derived from all globally distributed stations. The average of all *Kp* values for one day gives the *Ap* index. The *Dst* (disturbance storm time index) index is also used to monitor the severity of a geomagnetic storm and it is a direct measure of the hourly average of the ionospheric perturbation and is available in near real time (Basu et al., 2010). During the geomagnetic storm, the low and mid-latitude ionosphere are perturbed and an enhancement of ionospheric TEC occurs. This enhancement of the TEC transport from the lower latitudes to higher latitudes and redistributed in latitude and longitude forming a plume of enhanced TEC. This is referred to as Storm Enhanced Density (SED). The SED feature has been observed and reported over North America (Coster et al., 2003). More information about the SED will be provided later in this chapter.

3.2 Ionospheric Impact on GPS Signals

As mentioned in Chapter 2, GPS observables are used for positioning and navigation. The ionosphere is the main source of error for GPS measurements and ionospheric effects must be mitigated to obtain high positioning accuracy.

According to the dispersive characteristic of the ionosphere, the propagating signals through the ionosphere could be refracted, reflected, or absorbed. The ionospheric effect on GPS signals is reflected in the group delay of the pseudorange and in the phase advance of the carrier phase. This effect is quantified by the refractive index. In the following sections, the ionospheric impact on GPS signals is presented

3.2.1 Ionospheric Refractive Index

Index of refraction is the most important parameter to study the propagation of signals in the ionosphere. The ionospheric phase refractive index is given in the Appleton-Hartree formula as (Davies, 1990)

$$n_p^2 = 1 - \frac{X}{1 - iZ - \frac{Y_T^2}{2(1 - X - iZ)} \pm \left[\frac{Y_T^4}{4(1 - X - iZ)^2} + Y_L^2\right]^{\frac{1}{2}}} \tag{3.1}$$

where

$X = \frac{Ne^2}{\varepsilon_o m\omega^2} = \frac{f_n^2}{f^2}$

$Y_L = \frac{eB_L}{m\omega} = \frac{f_H \cos\theta}{f}$

$Y_T = \frac{eB_T}{m\omega} = \frac{f_H \sin\theta}{f}$

$Z = \frac{v}{\omega}$

$\omega = 2\pi f$

f is the carrier frequency

f_H is the electron gyrofrequency

f_n is the electron plasma frequency

N is the electron density (el/m^3)

e is the electron charge (-1.605x10^{-19} Coulomb)

ε_o is the permittivity of free space (8.854x10^{-12} Farads/m)

θ is the angle between the wave direction and the Earth's magnetic field

m is the mass of an electron (9.107x10^{-31} kg)

v is the electron neutral collision frequency

B is the ambient magnetic field

During solar maximum, the higher order terms contribute only 1 to 2 mm of range error (Brunner and Gu, 1991), and Equation (3.1) is therefore often reduced to

$$n_p = 1 - \frac{X}{2} = 1 - \frac{Ne}{2m\varepsilon_o(2\pi)^2 f^2} \tag{3.2}$$

Substituting values for the constants *e*, *m*, and ε_o, the phase index of refraction becomes

$$n_p = 1 - \frac{40.3\ N}{f^2} \tag{3.3}$$

Thus, the phase index of refraction depends only on the electron density N and the frequency of the radiowave signal.

The group velocity is the propagation velocity of the code envelope and the group index of the refraction can be derived from the following relation (Rao, 2010):

$$n_g = n_p + f\frac{d}{df}(n_p) \tag{3.4}$$

Differentiating Equation (3.3) and substituting Equation (3.4), the group index of refraction is given as

$$n_g = 1 + \frac{40.3\ N}{f^2} \tag{3.5}$$

By deriving the ionospheric index of refraction, it becomes possible to calculate the group and phase velocities which are essential to evaluate the ionospheric effects on GPS measurements.

3.2.2 Group Delay and Phase Advance

Due to the physical properties of the ionosphere, the ionospheric index of refraction is not a unit value and the assumption that GPS signals travel at the speed of light in a vacuum (as assumed in deriving GPS pseudorange and carrier phase observations) is incorrect. Therefore, it is important to determine the velocities of the code and the carrier phase. These velocities are given as follows

$$v_p = \frac{c}{n_p} = c\left(1 + \frac{40.3\ N}{f^2}\right) \tag{3.6}$$

$$v_g = \frac{c}{n_g} = c\left(1 - \frac{40.3\ N}{f^2}\right) \tag{3.7}$$

where c is the speed of light in a vacuum.

From Equations (3.6) and (3.7) it can be noted that the phase velocity exceeds the speed of light and is referred to as phase advance while the group velocity is less than the speed of light and is referred to as group delay.

The group delay (ΔR) and phase advance ($\Delta\Phi$) produce range errors which can be expressed in units of metres and are given as

$$\Delta R = \int_{path} (c - v_g)dt = \int_{path} \left(\frac{c}{v_g} - \frac{v_g}{v_g}\right)dl = \int_{path} (n_g - 1)dl = +\frac{40.3}{f^2}\int_{path} N dl \tag{3.8}$$

and

$$\Delta\Phi = \int_{path} (c - v_p)dt = \frac{1}{\lambda}\int_{path} (n_p - 1)dl = -\frac{40.3}{f^2}\int_{path} Ndl \quad (3.9)$$

The pseudorange and carrier phase ionospheric range errors are the same in magnitude but opposite in sign.

The quantity $\int_{path} Ndl$ is the integration of the electron density along the satellite-receiver signal path. This quantity represents the Total Electron Content (TEC) along the signal path. Therefore the ionospheric range error along the signal path is expressed as

$$I = \pm\frac{40.3}{f^2}TEC \quad \text{(in metres)} \quad (3.10)$$

where (+) denotes the group delay and (−) denotes the phase advance.

3.2.3 Total Electron Content (TEC)

The main parameter that describes the ionospheric effects on GPS is the measure of the total amount of electrons along the line of sight between the satellite and the receiver; this is referred to as the Total Electron Content (TEC). The TEC is expressed in TEC unit (TECU) which is equals to 10^{16} electrons per square metre. According to Equation (3.10), one TECU results in range error of 0.16 meters delay on L1 and 0.27 meters delay on L2.

TEC varies as a function of local time, season, geographic location, and solar cycle. TEC daily maximum occurs at 14:00 local time and the minimum occurs before sunrise.

Seasonally, the maximum TEC occurs at the Spring Equinox. Also, TEC geographic variations include peak values at $\pm 10^{o}$ geomagnetic latitude (the equatorial anomaly).

Using a dual frequency receiver, absolute TEC can be derived using a linear combination of L1 and L2 frequency range observations (R_1 and R_2 respectively):

$$TEC_R = \frac{1}{40.3}\frac{f_1^2 f_2^2}{f_1^2 - f_2^2}(R_1 - R_2) \tag{3.11}$$

The derived TEC from the code measurements are noisy and biased. If these biases are not removed, GPS generates relative TEC rather than absolute TEC. The noise in the absolute TEC derived from code measurements can be smoothed using the more precise carrier phase measurements. Relative TEC derived from carrier phase measurements depends on the L1 and L2 ambiguities and biases and is given by

$$TEC_\Phi = -\frac{1}{40.3}\frac{f_1^2 f_2^2}{f_1^2 - f_2^2}\left[(\Phi_1 - \Phi_2) - \varepsilon_{\Phi,12} - b_r - b_s - \lambda_1 N_1 - \lambda_2 N_2\right] \tag{3.12}$$

where

$\varepsilon_{\Phi,12}$ is the carrier phase noise

b_r , b_s are the receiver and satellite biases respectively, and

N_1, N_2 are the integer ambiguities on L1 and L2 carrier phase measurements respectively

3.3 Ionospheric Modeling

Ionospheric ranging errors degrade GPS positioning accuracies. In order to remove the ionospheric effect, different methods are used to determine the ionospheric corrections

and apply them to the measurements. There are several ways to remove the ionospheric range errors such as single frequency ionospheric modeling, applying dual frequency corrections, and wide area ionospheric modeling.

The Klobuchar broadcast model is an ionospheric corrections model for single frequency GPS users where 50 percent rms ionospheric range error reduction can be obtained (Klobuchar, 1987). Based on the dispersive property of the ionosphere, dual frequency GPS receivers can be used derive to ionospheric-free observation from a linear combination of L1 and L2 measurements (Lachapelle, 2008).

For a large geographical area, wide area ionospheric modeling can be used to generate ionospheric range error corrections. This ionospheric model is based on observations from a network of reference stations distributed within the geographical area of interest that provides high level positioning accuracy. There are many existing wide area ionospheric model approaches such as a functional model, grid model, and spherical harmonics model. For the purpose of this work, the grid model is described briefly here.

The grid model consists of a network of dual frequency GPS reference stations that calculate ionospheric TEC observations and map them to an ionospheric shell at approximately 350 km altitude. The TEC observations are generated at ionospheric pierce points (IPP) where the satellite-receiver lines-of-sight intersect the ionosphere shell. More details about the IPP definition and the ionospheric shell model are discussed in the next section. The grid model uses the TEC values (ionospheric delays) to estimate ionospheric corrections at fixed predefined points called grid points. At the user location,

local ionospheric corrections are generated by interpolating the corrections from the surrounding grid points. This type of two-dimensional model is applied for the WAAS where the ionospheric delays are estimated at grid point spacings of $5^o \times 5^o$ in latitude and longitude over North America.

3.4 Ionospheric Delay Observation

The ionospheric pierce point (IPP) is the intersection between the receiver-satellite line of sight and the ionosphere modeled as a thin shell chosen at 350 km altitude above earth's surface. This altitude of the ionospheric shell is chosen because the majority of electron density affecting GPS signals is concentrated in the F region. Figure 3.2 illustrates the thin shell and the IPPs.

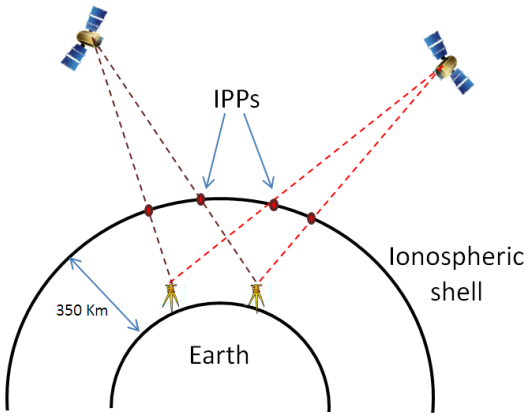

Figure 3.2: The Ionospheric Shell and the IPPs

The latitude of the IPP is calculated as follows (U.S. DOT, 1999):

$$\emptyset_{pp} = \sin^{-1}\left(\sin\phi_u \cdot \cos\psi_{pp} + \cos\phi_u \cdot \sin\psi_{pp} \cdot \cos A\right) \quad radians \tag{3.13}$$

where A is the azimuth angle, ϕ_u is the user latitude, and ψ_{pp} is earth's central angle between the user position and the earth projection of the pierce point (shown in Figure 3.3) calculated as

$$\psi_{pp} = \frac{\pi}{2} - E - \sin^{-1}\left(\frac{R_e}{R_e + h_i} \cdot \cos E\right) \quad radians \tag{3.14}$$

where R_e is the earth radius, E is the satellite elevation angle, and h_i is the shell height. The longitude of the pierce point is calculated as

$$\lambda_{pp} = \lambda_u + \sin^{-1}\left(\frac{\sin\psi_{pp} \cdot \sin A}{\cos\phi_{pp}}\right) \quad radians \tag{3.15}$$

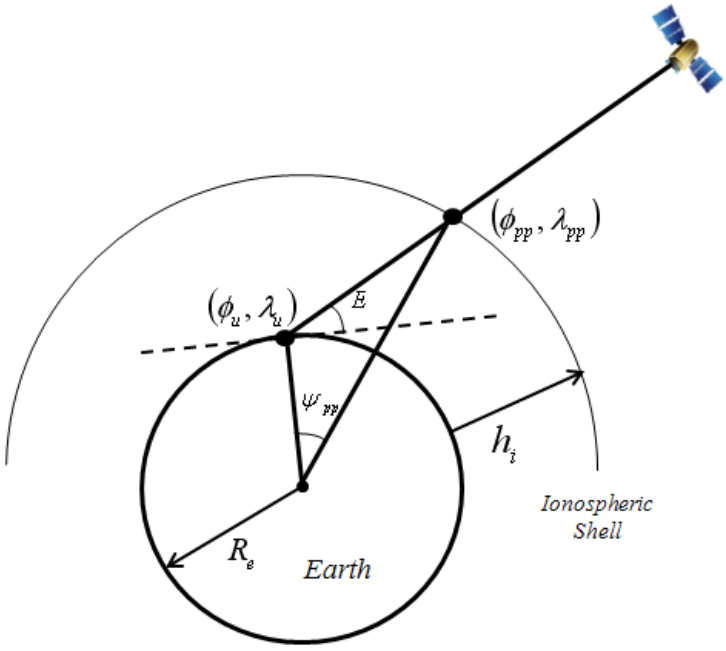

Figure 3.3: Ionospheric Pierce Point Geometry

Since the GPS measurements are made for slant paths, the ionospheric delay measured at the IPP is referred to as the slant delay or slant TEC (STEC). These STECs are usually projected into Vertical TEC using an obliquity factor. At the IPPs, the STEC is related to the VTEC as

$$STEC = VTEC \times M(E) \tag{3.16}$$

where $M(E)$ is the obliquity factor dependent on satellite elevation angle E, Earth radius R_e and the ionospheric shell altitude h_i as given by

$$M(E) = \left[1 - \left(\frac{R_e \cos E}{R_e + h_i}\right)^2\right]^{-\frac{1}{2}} \tag{3.17}$$

Figure 3.4 below illustrates how IPP, STEC, and VTEC are related for the thin shell model.

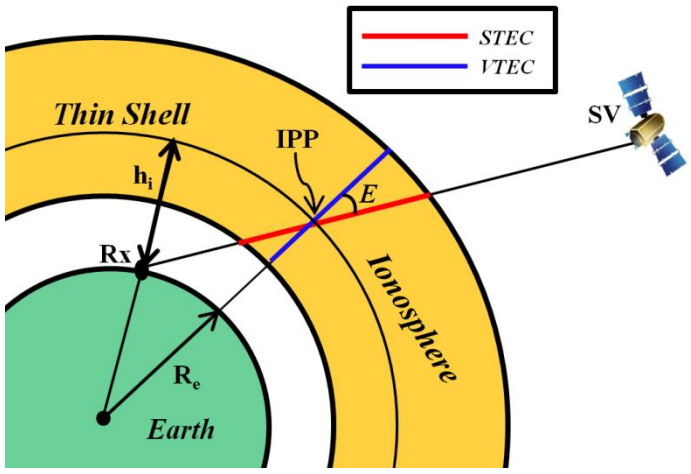

Figure 3.4: STEC vs. VTEC

3.5 Storm Enhanced Density (SED)

High solar activities result in geomagnetic storms and associated ionospheric phenomena. In the initial stage of geomagnetic storm, the ionosphere at low and mid-latitudes can be highly disturbed with a plume of enhanced electron density forming. During this geomagnetic disturbance, the plume of the enhanced electron density may evolve and extend to the higher latitudes. This phenomenon is called Storm Enhanced Density (SED).

3.5.1 SED Characteristics

The SED forms during geomagnetic storms near the dusk sector at latitudes near the main ionospheric trough - in a region where the ionospheric plasma overlaps with the poleword directed electric field. This Sub-Auroral Polarization Stream (SAPS) (Foster and Bruke, 2002) drives the plasma within the SED in a northward and westward (poleward and sunward) direction. The enhanced mid-latitude TEC at the base of the plume is likely related to the storm–time penetration electric fields. These penetration electric fields are responsible for the uplift of mid- and low latitude plasma and the redistribution of this plasma to the mid- and high-latitude ionosphere. Additional forces such as neutral winds and internally generated electric fields (those produced within the ionosphere) also contribute to the SED formation (Coster and Skone, 2009). The electrons in the SED plume have velocities of 800 m/s giving the plasma an approximately two-hour transit time from its source at low latitudes to polar cap (Foster, 1993).

The SED magnetic conjugacy effects have been studied (Foster and Rideout, 2007). It has been concluded that the SED plume occurs in magnetically conjugate regions in both hemispheres; however the TEC enhancement at the base of the SED plume exhibits localized and longitude-dependent features which are not strictly magnetically conjugate although the SED plumes streaming away from these source regions closely follow magnetic conjugate paths.

Very large TEC gradients are associated with the SED plume. Within the plume edges sharp drops and increases in TEC values are observed within short time periods. For example, a moderate storm occurred October 2001 with SED over North America and TEC values for a single satellite-receiver line-of-sight decreased from 60 TECU to 15 TECU in approximately 10-15 minutes. These TEC gradients can significantly degrade GNSS precise positioning capabilities (Coster and Skone, 2009).

3.5.2 SED Storm Events

Over the past decade, many SED storms have occurred with varying strengths in different regions of the globe. On 15-16 July 2000, solar flares led to severe SED effects in the nightside South Atlantic Anomaly (SAA) region (Dmitriev and Yeh, 2008). In Europe different SED events were observed 3 October 2001 and on 18 April 2002 (Coster et al., 2007). Most importantly for this work, three SED events have been observed with high resolution over North America. Two of these SED events were superstorm events during the previous solar maximum: 20 November and 29-30 October 2003. The third strong SED event was observed on 31 March 2001 (Skone et al., 2004) (Foster and Rideout,

2007) (Coster and Skone, 2009). This work focuses on the two 2003 severe storms which reflect worst-case challenges for GPS/WAAS applications. Figure 3.5 shows two-dimensional TEC maps for 20 November and 30 October 2003 SED storms. These maps are derived from more than 500 GPS reference station observations in North America. Impact of the 2003 SED events on WAAS and a detailed analysis of these storms will be presented in Chapters 4 and 5 respectively.

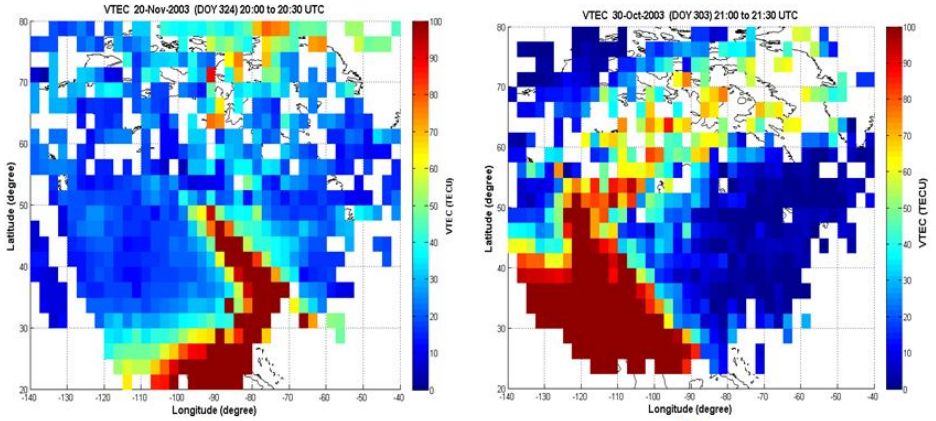

Figure 3.5: VTEC maps of the SED features over the Canadian Latitudes. (a) TEC map of SED feature on 20 November 2003 between 2000 and 2030 UT, and (b) is TEC map of SED feature on 30 October 2003 between 2000 and 2030 UT

3.5.3 SED Impact on DGPS and WADGPS

The impact of ionospheric effects on GPS positioning accuracy can be mitigated using DGPS or WADGPS techniques – in particular to provide better performance in terms of accuracy, reliability, and availability. However, during SED periods, a considerable degradation in DGPS and WADGPS positioning accuracy can occur. These degradations

in positioning accuracy are observed near the SED plume, near large TEC gradients, where positioning errors can exceed 20 m (Coster and Skone, 2009).

Many studies have investigated the impact of SED phenomena on DGPS and WADGPS such as WAAS. For example, in (Skone and Yousuf, 2007) it has been shown that horizontal DGPS errors increased by factors of 10-30 during the 29-30 October 2003 storm. Moreover, in comparing DGPS with WADGPS it has been determined that WADPGS positioning errors exceed those for DGPS during SED events; this is attributed to the sparse WADGPS reference network and associated limitations in resolving the severe ionospheric gradients. SED impact on WAAS is discussed in the next chapter.

Chapter Four: Wide Area Augmentation System

4.1 Augmenting GPS

GPS uses the measurements transmitted from the satellite to the receiver to calculate positions. These measurements propagate through the atmosphere which refracts the signal and affects positioning accuracy. The major source of GPS ranging error is the ionosphere, which is the focus of this research; ionospheric ranging error varies with electron density which is a function of solar activity. It is very hard to model the ionospheric effects during high ionospheric activity and geomagnetic storms and the ionospheric impact is severe during storms. Therefore, many techniques (e.g. DGPS) are employed to augment GPS and mitigate the ionospheric effect in ranging measurements in order to obtain high positioning accuracy. But such methods are not sufficient to capture ionospheric features during severe geomagnetic storms over wide regions. Thus, another technique is employed for this purpose called Wide Area DGPS (WADGPS).

A Satellite Based Augmentation System (SBAS) is a WADGPS system used to augment GPS and compensate for certain limitations in GPS in terms of accuracy, integrity, and availability. SBAS employs a network of reference stations distributed over a wide area to collect GPS observations and generate GPS corrections uplinked and broadcast to users through geostationary satellites.

The Federal Aviation Administration, which is responsible for civil aviation in the United States, has implemented their own SBAS called the Wide Area Augmentation System

(WAAS) to provide GPS corrections and integrity information for aviation users in the CONterminous United States (CONUS). Currently WAAS is used in air navigation and supports all phases of flight (en route navigation and landing) to meet high accuracy, integrity, continuity, and availability for aviation users.

4.2 WAAS Structure

WAAS consists of a ground-based network that includes L1 (1575.42 MHz) and L2 (1227.6 MHz) dual frequency GPS receivers known as wide area reference stations (WRSs). These WRSs monitors GPS satellites and collect GPS L1 and L2 signals (L2 signal processing accomplished using a semi-codeless tracking technique to derive code measurements). WRSs collect GPS measurements and send them to a master station known as wide area master station (WMSs) through a Terrestrial Communication Network (TCN). These WMSs process the observations sent by the WRSs to estimate satellite clock and ephemeris errors and ionospheric delay. Three types of corrections are calculated: (1) Fast Corrections (FC) for each GPS satellite, (2) Long Term Corrections (LTCs) for each satellite's slow clock drift and slow ephemeris errors and (3) ionospheric corrections calculated at pre-defined globally distributed grid points. Along with the corrections, WMSs calculate error bounds for ionospheric corrections called Grid Ionospheric Vertical Errors (GIVEs) and a combined error bound for the clock and the ephemeris corrections called User Differential Range Errors (UDREs).

Currently WAAS has 38 WRSs and three WMSs and each one of these master stations can perform the WAAS corrections and error bounds. These correction data are

forwarded to a Ground Earth Station (GES) to be uplinked to Geostationary Earth Orbit (GEO) satellites. WAAS currently relies on three GEOs where each one transmits the WAAS message in an L1 signal coded is a similar manner as a GPS satellite C/A code transmission.

Aircraft systems equipped with WAAS-certified receivers apply these corrections to the GPS pseudorange observations to improve positioning accuracy. The GIVE and UDRE error bounds are used to calculate the confidence bounds of position error called Vertical Protection Level (VPL) and Horizontal Protection Level (HPL) (GPS WAAS PS, 2008). The VPL is half the length of a segment on the vertical axis (perpendicular to the horizontal plane of WGS-84 ellipsoid), with its centre being at the true position, which describes the region that is assured to contain the indicated vertical position. VPL based on the error estimates provided by WAAS. The HPL is the radius of a circle in the horizontal plane (the plane tangent to the WGS-84 ellipsoid), with its centre being at the true position, which describes the region that is assured to contain the indicated horizontal position. HPL is also based on the error estimates provided by WAAS (Yousuf and Skone, 2005).

The focus of this research is validity of the ionospheric corrections and error bounds, for reliable vertical positioning in aviation application.

4.3 WAAS Ionospheric Corrections

WAAS offer corrections for ionospheric, clock, and ephemeris errors. This study focuses on WAAS ionospheric corrections at Canadian latitudes. In general, WAAS estimates ionospheric delay along with GIVE error bound at each Ionospheric Grid Point (IGP) that are broadcast by the WAAS. These IGPs have $5^{o}x5^{o}$ spacing between latitudes S55 and N55 and larger spacings beyond this region (U.S. DOT, 1999). The spatial distribution of WAAS IGPs over the globe is shown in Figure 4.1.

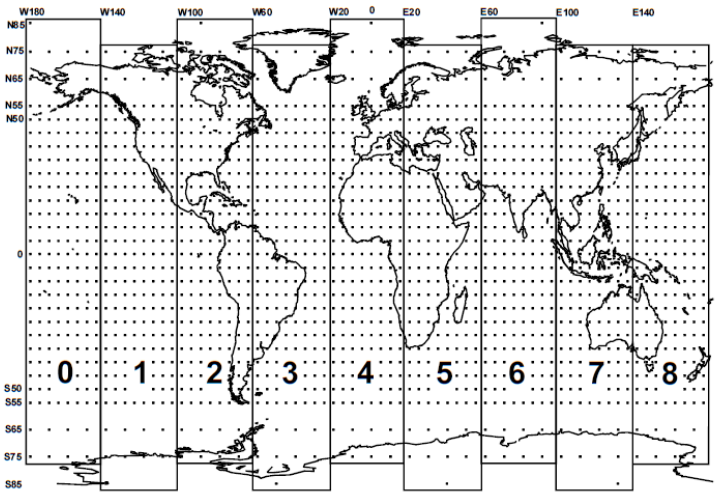

Figure 4.1: Global WAAS IGPs (U.S. DOT, 1999)

4.3.1 Ionospheric Delay Estimation

As introduced in Chapter 3, each ionospheric measurement is mapped to an ionospheric pierce point (IPP) on an ionospheric shell. WAAS collects the vertical ionospheric delays for all visible satellites within the network at the IPPs and a planar fit algorithm is applied to estimate ionospheric delays (corrections) at the IGPs. In a future WAAS upgrade,

another estimation technique called Kriging will be used. More details about these two estimation techniques are provided later in this chapter.

The ionospheric delays at each IPP are calculated using dual frequency L1 and L2 pseudorange measurements from WRSs. The absolute ionospheric slant delay in metres is calculated as

$$I_{slant} = \left(\frac{f_2^2}{f_1^2 - f_2^2}\right)(\rho_{L1} - \rho_{L2}) \tag{4.1}$$

where f_1 and f_1 are L1 and L2 signal frequencies respectively, ρ_{L1} and ρ_{L2} are pseudorange measurements from L1 and L2 respectively.

The slant delay at each IPP is converted to vertical delay using a mapping function:

$$I_v = \frac{1}{M(E)} \cdot I_{slant} \tag{4.2}$$

where I_v the ionospheric vertical delay and $M(E)$ is the mapping function discussed in Chapter 3 and given by

$$M(E) = \left[1 - \left(\frac{R_e \cos E}{R_e + h_i}\right)^2\right]^{-\frac{1}{2}} \tag{4.3}$$

All IPPs with observation elevation angles greater than or equal to 5^o and which reside within a minimum radius R_{min} of the given IGP are included in the planar fit. If the number of IPPs within this fit radius is less than N_{target}, the fit radius R_{fit} is extended until

it encompasses N_{target} IPPs. If the radius extended to a maximum value R_{max} without encircling the N_{target} IPPs, the fit is done by using the available IPPs provided that the available IPPs are not less than a specific number of IPPs N_{min}. If the numbers of the IPPs within R_{max} are fewer than N_{min}, no estimation is computed. Currently the values used for R_{min}, R_{max}, N_{target}, and N_{min} are 800 km, 2100 km, 30, and 10 respectively (Sparks et al., 2005).

The ionospheric delays measurements at the IPPs within the cutoff radius around the IGPs and their variances can be represented by vector notation (Walter et al., 2000):

$$I_{v,IPP} = \begin{bmatrix} I_{v,IPP_1} \\ I_{v,IPP_2} \\ \vdots \\ I_{v,IPP_N} \end{bmatrix} \tag{4.4}$$

$$\sigma^2_{v,IPP} = \begin{bmatrix} \sigma^2_{v,IPP_1} \\ \sigma^2_{v,IPP_2} \\ \vdots \\ \sigma^2_{v,IPP_N} \end{bmatrix} \tag{4.5}$$

The variances of the vertical delays at each IPP in the variance vector represent the noise, multipath and bias uncertainty for the i^{th} IPP.

Initially, WAAS uses a planar fit estimation technique of the neighbouring vertical delays to calculate the vertical delay at each IGP. In a future release of WAAS, estimation of the ionospheric delay will be performed with a kriging method. Both estimation approaches are discussed in the following two sections.

4.3.1.1 Planar Fit Estimation

Currently, WAAS employs a planar fit algorithm to generate the correction at each IGP. Planar fit estimation assumes that the vertical delay at the IGP is a linear combination of the vertical delays at all IPPs within the cutoff radius. Using a local Cartesian frame with origin at the IGP and *x*-axis aligned East and *y*-axis aligned North, the vertical delay at the IGP is modeled as follows (Walter et al., 2000; Sakai et al., 2008)

$$\hat{I}_{v,IGP}(\mathrm{x}, y) = \hat{a}_0 + \hat{a}_1 \cdot x + \hat{a}_2 \cdot y \tag{4.6}$$

Planar coefficients can estimated as

$$\begin{bmatrix} a_0 \\ a_1 \\ a_2 \end{bmatrix} = (G^T \cdot W \cdot G)^{-1} \cdot G^T \cdot W . I_{v,IPP} \tag{4.7}$$

where W is the weighting matrix given by

$$W^{-1} = \begin{bmatrix} \sigma^2_{I_v,IPP_1} + \sigma^2_{decorr} & \sigma_{bias,1,2} & \cdots & \sigma_{bias,1,N} \\ \sigma_{bias,1,2} & \sigma^2_{I_v,IPP_2} + \sigma^2_{decorr} & \cdots & \sigma_{bias,2,N} \\ \vdots & \vdots & \ddots & \vdots \\ \sigma_{bias,1,N} & \sigma_{bias,2,N} & \cdots & \sigma^2_{I_v,IPP_N} + \sigma^2_{decorr} \end{bmatrix} \tag{4.8}$$

The decorrelation function σ_{decorr} denotes the inherent uncertainty of the fit plane and currently its value is set to 35 cm. The terms $\sigma_{bias,i,j}$ are covariances that specify the correlation of bias errors between vertical delay measurements made with common

satellites or common receivers (Walter et al., 2000; Sparks et al., 2005; Sakai et al., 2008).

The observation matrix G is given by

$$G = \begin{bmatrix} 1 & d_{IPP_1,IGP} \cdot \hat{E} & d_{IPP_1,IGP} \cdot \hat{N} \\ 1 & d_{IPP_2,IGP} \cdot \hat{E} & d_{IPP_2,IGP} \cdot \hat{N} \\ \vdots & \vdots & \vdots \\ 1 & d_{IPP_N,IGP} \cdot \hat{E} & d_{IPP_N,IGP} \cdot \hat{N} \end{bmatrix} \tag{4.9}$$

where $d_{IPP_N,IGP}$ is the distance between the N^{th} IPP and the IGP in the East and North directions.

The ionospheric delay estimated at the IGP is given by

$$\hat{I}_{v,IGP} = a_0 \tag{4.10}$$

and the formal error on the estimated delay at the IGP is given by

$$\hat{\sigma}^2_{\hat{I}_{v,IGP}} = [(G.W.G^T)^{-1}]_{1,1} = \begin{bmatrix} 1 \\ 0 \\ 0 \end{bmatrix}^T (G \cdot W \cdot G^T)^{-1} \begin{bmatrix} 1 \\ 0 \\ 0 \end{bmatrix} \tag{4.11}$$

4.3.1.2 Kriging Estimation

In a future release of WAAS, vertical delay estimation at the IGPs will be implemented using Kriging estimation method. Using Kriging technique, the ionospheric measurements at an IPP assumed to be of the form (Blanch, 2002)

$$I_{v,meas}(x_k, y_k) = a_0 + a_1 x_k + a_2 y_k + R(x_k, y_k) + N_k \quad (4.12)$$

With N_k the measurement noise and R is the scalar field describing small irregularities that are superimposed on the planar trend. Kriging technique takes advantage from the random structure of the ionospheric delays to define the covariance structure among the measurements and between the measurements and the IGP where the delay is to be estimated to find the optimal estimator in a least squares sense (Blanch and Walter, 2004). Kriging estimate of the ionospheric vertical delay at the IGP is given by (Sparks et al., 2010)

$$\hat{I}_{IGP=} \lambda_v^T \, I_{IPP} \quad (4.13)$$

where I_{IPP} is the set of measurements and λ_v is the vector of coefficients given by

$$\lambda_v = [W_v - W_v G_v (G_v^T W_v G_v)^{-1} G_v^T W_v] c_v + W_v G_v (G_v^T W_v G_v)^{-1} [1 \quad 0 \quad 0]^T \quad (4.14)$$

where c_v is an N-vector whose elements specify the covariance between the scalar field at a position Δx near the IGP and the detrended delays at the measurement locations, G_v and W_v are the observation matrix and the weight matrix given by Equations (4.15) and (4.16) respectively.

$$G = \begin{bmatrix} 1 & \Delta x^T_{IPP_1,IGP} \cdot \hat{E} & \Delta x^T_{IPP_1,IGP} \cdot \hat{N} \\ 1 & \Delta x^T_{IPP_2,IGP} \cdot \hat{E} & \Delta x^T_{IPP_2,IGP} \cdot \hat{N} \\ \vdots & \vdots & \vdots \\ 1 & \Delta x^T_{IPP_N,IGP} \cdot \hat{E} & \Delta x^T_{IPP_N,IGP} \cdot \hat{N} \end{bmatrix} \tag{4.15}$$

$$W_v = [M + C]^{-1} \tag{4.16}$$

where Δx is the vector describing the distance between the IPP and the IGP, M is the $N \times N$ measurements noise covariance matrix, and C is the $N \times N$ nominal ionosphere covariance matrix at the IGP. More details about ionospheric delay estimation using kriging method are provided in Blanch, (2002), Blanch et al., (2003), and Blanch et al., (2004).

4.3.2 WAAS Reliability

Along with the estimated delay at the IGP, WAAS provides an associated error bound called Grid Ionospheric Vertical Error (GIVE). The GIVE values are a measure of the error confidence bound at each IGP. GIVE confidence bounds are computed as (Sakai et al., 2008)

$$\sigma^2_{GIVE} = R^2_{irreg}\sigma^2_{IGP} + max\left(R^2_{irreg}\sigma^2_{decorr}, \sigma^2_{undersampling}\right) + \sigma^2_{rate\ of\ change} \tag{4.17}$$

where $\sigma^2_{undersampling}$ denotes the undersampling threat, R^2_{irreg} is the inflation factor calculated from the ionospheric regularity detector, and $\sigma^2_{rate\ of\ change}$ is the term

describing rate of change of the ionosphere. These component contributions in the error bound calculations are discussed later in this chapter.

WAAS provides GIVE indicators in WAAS message which range from 0 to 15. Each value of the GIVE indicator associated with a specific error and σ^2_{GIVE} value can be obtained from a look-up table. These indicators and the associated errors and variances are shown in Table 4-1 (U.S. DOT, 1999).

Table 4-1: GIVE indicators and their associated errors and variances

GIVE Indicator	GIVE (m)	σ^2_{GIVE} (m^2)
0	0.3	0.0048
1	0.6	0.0333
2	0.9	0.0749
3	1.2	0.1331
4	1.5	0.2079
5	1.8	0.2994
6	2.1	0.4075
7	2.4	0.5322
8	2.7	0.6735
9	3.0	0.8315
10	3.6	1.1974
11	4.5	1.8709
12	6.0	3.3260
13	15.0	20.7870
14	45.0	187.0826
15	Ionosphere Not Monitored	Ionosphere Not Monitored

The maximum error value is 45 coupled with indicator value of 14; this is used as a threshold to account for reliability in aviation. When the indicator is 15, the service will be denied because the ionosphere is not monitored.

The FAA website provides a real time WAAS IGP status. Figure 4.2 shows the estimated ionospheric delays (corrections) and the GIVE values for 6 June 2011.

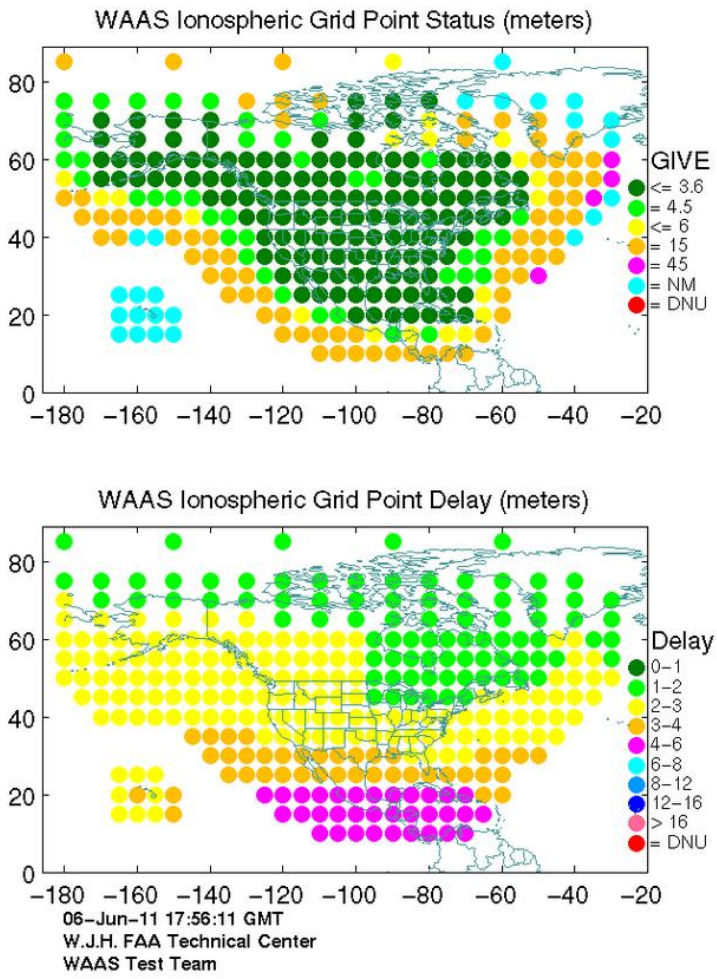

Figure 4.2: WAAS GIVE (Top) and Ionospheric Delays (Bottom)
[http://www.nstb.tc.faa.gov/Full_WaasIGPStatus.htm]

Another index used for reliability is called User Ionospheric Vertical Error (UIVE) which is the bound on the vertical ionospheric delay error computed by the user and calculated at a user's IPP by interpolating GIVE values surrounding the user's IPP.

4.4 Ionospheric Irregularity Detection

Unfortunately, the ionosphere is not smooth and varying slowly. There are conditions where the ionosphere is disturbed and irregular. This ionospheric behaviour may violate the simple model used to estimate ionospheric vertical delays at IGPs. Therefore, it is important to implement additional algorithms that detect such behaviours and bound them properly. For irregularity detection, any ionospheric effect or event that invalidates the model must be taken into consideration regardless of the nature of the effect (i.e., ionospheric storm, irregularities, or scintillation). For this purpose, WAAS uses an irregularity detector based upon the chi-square χ^2 statistic of the planar fit; this test is known as a chi-square consistency check or "goodness-of-fit" test (Walter et al., 2000; Sparks et al., 2005).

For planar fit ionospheric model, the χ^2 statistic can be defined as

$$\chi^2 = I_{v,IPP}^T \cdot W \cdot \{I - G^T \cdot (G.W \cdot G^T)^{-1} \cdot G \cdot W\} \cdot I_{v,IPP} \tag{4.18}$$

When χ^2 exceeds a specific threshold, then the model assumption is violated and the presence of ionospheric irregularity is declared. However, χ^2 below this threshold does not guarantee that the model is valid. Moreover, if the estimated variances have increased beyond their assumed values, the chi-square value will be affected statistically and for both cases (the model is incorrect or the variances increased) the event will be undetected. Therefore, the probability of missing this event must be determined and the

error bound inflated as necessary. The inflation factor (R^2_{irreg}) can be determined using the expected χ^2 distribution and the χ^2 distribution of the failure model.

4.4.1 Inflation Factor (R^2_{irreg})

As discussed, the confidence bound must be inflated with a certain value to avoid undetected events. Since the measurements and their variances are known, then the expected distribution for the chi-square (χ^2) variable is known also. When the variances are increased, χ^2 distribution will remain unchanged except it will be stretched along the chi-square axis.

For the failure model distribution (presence of irregularity or increased variances), the distribution exceeds the threshold, but there is a small part of this distribution below this threshold which will indicate that the model is not violated and this part will cause a problem in detecting the failure; this part below the threshold should be as small as possible. The probability of this part of the distribution is the integration of the distribution's Probability Density Function (PDF) below the threshold; this is called missed detection probability (P_{md}) and this probability should be as small as possible. For the expected distribution, a small part is above the threshold which will cause the test to declare presence of irregularities in the absence of such events. This part of the distribution is called false alarm probability (P_{fa}) and should also be as small as possible. Figure 4.3 below illustrates the expected χ^2 distribution and the distribution of the failure model (Walter et al., 2000) .

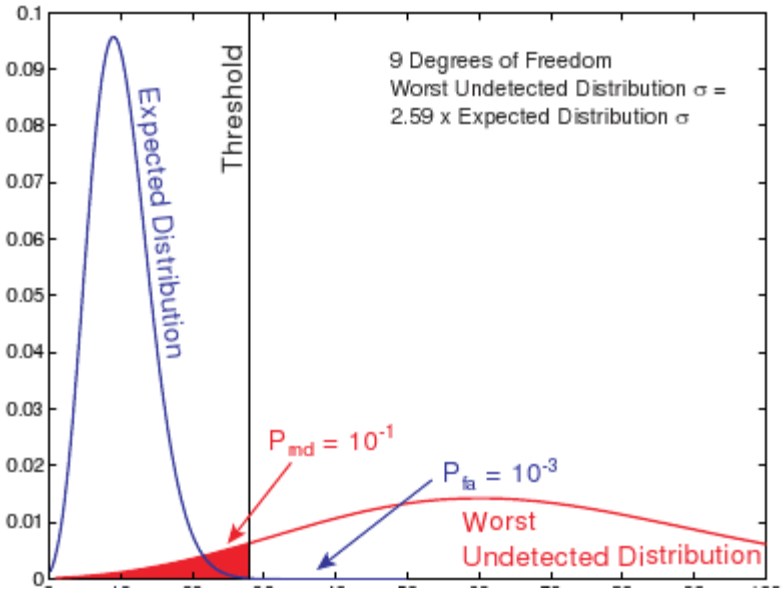

Figure 4.3: Chi-square expected distribution and the worst undetected distribution (Walter et al., 2000)

To determine the inflation factor, values are set for P_{md} and P_{fa} and the ratio of the upper threshold to the lower bound is calculated:

$$R^2_{irreg} = \frac{\chi^2_{1-P_{fa}}}{\chi^2_{P_{md}}} \tag{4.19}$$

where χ^2_p is the chi-square value that has probability P of the distribution.

Figure 4.3 shows an example using nine degrees of freedom with $\mathrm{P_{md}} = 10^{-1}$ and $P_{fa} = 10^{-3}$, where $\chi^2_{P_{md}=10^{-1}} = \chi^2_{0.1} = 4.7$, and $\chi^2_{1-P_{fa}} = \chi^2_{1-10^{-3}} = \chi^2_{0.999} = 27.9$, and therefore, $R^2_{irreg} = 6.69$. Under the failure model, the distribution with variances inflated by the value R^2_{irreg} is called worst undetected distribution and this is the worst distribution that can pass the test without detecting irregularities (i.e., the worst

distribution the chi-square can protect against). For any inflation in the variances above this value of R^2_{irreg} the chi-square value will fail to protect against irregularities and will pass the test. Since the chi-square test protects against this distribution, the confidence bound must be generated according to it. Therefore, the variances in the GIVE error bound at a given IGP must be multiplied by $R^2_{irreg}$to ensure that it guards against all distributions that pass the chi-square check (Walter et al., 2000).

4.5 Ionospheric Threat Model

WAAS estimates the ionospheric delay at each IGP using the IPPs within the fit radius. In some cases, the irregularity region is not sampled (not monitored) by WRSs and, at the same time, some users may have IPPs inside the irregularity region (not observed by the WRSs). This condition is called undersampling threat as illustrated in Figure 4.4.

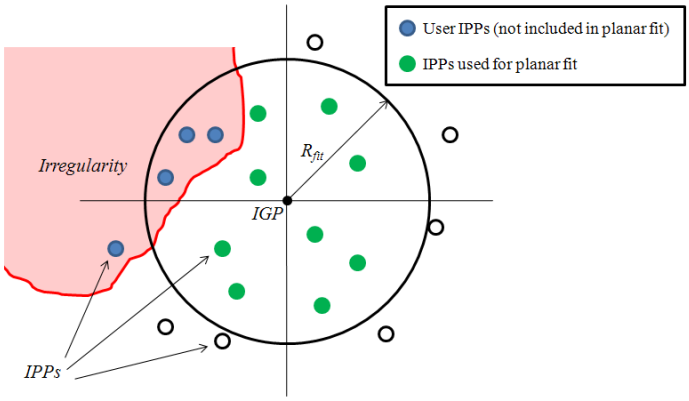

Figure 4.4: Undersampling threat

WAAS relies on an ionospheric threat model to protect against the undersampling threat, and to generate a correction that is added to the confidence bound of the delay estimates.

The threat model contributes $\sigma^2_{undersampling}$ to the confidence bound which is calculated using a data deprivation technique.

Data Deprivation

To examine the effect of a threat, WAAS has to examine the data affected by this threat. First, the effect must be sampled and then the effect of undersampling simulated. This can be achieved using data deprivation. Different schemes of data deprivation have been implemented. The first method is called geometric deprivation where IPPs or WRSs are removed based on their geographic location. The second method is missing station deprivation where either a WRS or a satellite is removed and a virtual user measurement is used (Pandya et al., 2007). In (Walter et al., 2004) another method is proposed called malicious deprivation. This method provides worst case undersampling conditions to alert WAAS to the presence of ionospheric features; IPPs affected by the feature and having the highest residuals are removed, leaving the undisturbed IPPs in the data set that fail to detect the disturbance. The remaining IPPs represent the worst possible sampling of the ionosphere. Another variation of malicious deprivation is called continued malicious deprivation where the IPPs are removed until there are insufficient IPPs to perform the fit resulting in a worse ionospheric threat (Walter et al., 2004). These methods to determine undersampling threat update the GIVE to guard against undetectable features.

4.6 Rate of Change

The ionospheric correction and the confidence bound calculated at each grid point is sent to users at a slow rate (maximum 5 minutes). The ionosphere can change quickly, and in this case WAAS must increase the update rate. To perform this, the threat model provides a histogram of the ionospheric delay changing over a period of time based on the χ^2 check and the spatial decorrelation. Based on this information, the rate of WAAS updates changes and another term is added to the confidence bound called $\sigma^2_{rate\ of\ change}$ to protect against the ionospheric change. During high ionospheric activity, WAAS may update grid information at a faster rate such as less than one minute (Walter et al., 2000; El-Arini et al., 2001).

4.7 WAAS Integrity

WAAS was developed by the FAA and DOT to be used in aviation applications to support flight operations in different stages. During low visibility conditions, pilots rely on a type of air navigation called Instrument Approach to land or to reach visual conditions permitting landing. Depending on navigation aid accuracy and capabilities, Instrument Approach is divided into Precision approach (PA) which provides both horizontal and vertical guidance to the runway or Non-Precision approach (NPA) which gives only horizontal guidance. PA has different types of operations including Lateral NAVigation (LNAV) and Vertical NAVigation (VNAV) approach with vertical guidance (APV), and WAAS Category I (CAT I) precision approach flight operation.

WAAS integrity can be defined as the ability to provide timely warnings to users when the system should not be used for navigation. Integrity requirements are specified in terms of the probability of misleading information in a flight operation. WAAS guarantees that the user's actual position error will be bounded by the protection levels (i.e., HPL and VPL) with probability ≥ 99.99999% of the time (i.e., having one chance in 10^7 of the GPS being in error by more than the HPL and VPL.). The two protection levels are calculated in real time by the user's GPS and compared with thresholds called Alert Limits which are the maximum values allowed for safe operation. Alert Limits are classified as Horizontal Alert Limit (HAL) and Vertical Alert Limit (VAL). The values of VAL and HAL are fixed, predefined and chosen depending on the operation. If the VPL exceeded the VAL and/or the HAL exceeded the VAL, WAAS provides warnings to users that the system should not be used for navigation (Walter and Enge, 2004; El-Arini et al., 2001). The navigation integrity requirements for different flight operations are shown in Table 4-2 (GPS WAAS PS, 2008).

Table 4-2: WAAS integrity requirements

Operation	***Integrity***	***Time to Alert***
En Route	10^{-7} per hour	15 seconds
Terminal	10^{-7} per hour	15 seconds
LNAV	10^{-7} per hour	10 seconds
LNAV/VNAV	2×10^{-7} per approach	10 seconds
LPV	2×10^{-7} per approach (150 seconds)	6.2 seconds
LPV 200	2×10^{-7} per approach (150 seconds)	6.2 seconds

4.8 WAAS Availability

Availability is defined as the probability that the navigation and fault detection are operational and that GPS/WAAS Signal-in-Space (SIS) accuracy, integrity and continuity of function requirements are met (U.S. DOT, 1999): i.e., the time that WAAS provides usable service, required function and performance.

For PA flight phase, availability requires that VPL and HPL are less than predefined parameters VAL and HAL, respectively, for more than 99% of the time during one approach. For enroute, terminal, and NPA phases, WAAS availability requires HPL less than HAL for 99.999% of the time during one hour (GPS WAAS PS, 2008; El-Arini et al., 2001).

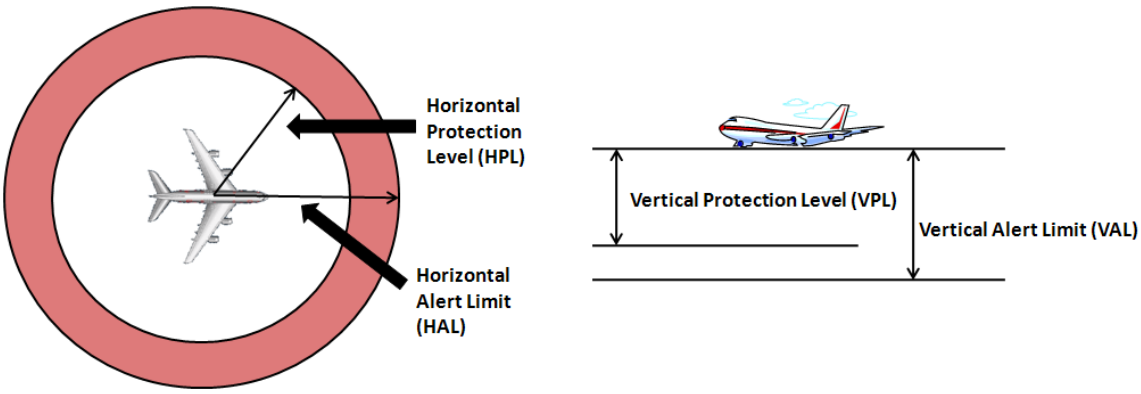

Figure 4.5: Definition of (a) HAL and (b) VAL

Table 4-3 summarizes WAAS availability requirements and VAL and HAL values for different flight operation.

Table 4-3: WAAS availability requirements

Operation	*HAL*	*VAL*	*Availability*
En Route	2 nm	N/A	$Pr\{HPL \leq HAL\} \geq 0.99999$
Terminal	1 nm	N/A	$Pr\{HPL \leq HAL\} \geq 0.99999$
LNAV	556 m	N/A	$Pr\{HPL \leq HAL\} \geq 0.99999$
LNAV/VNAV	556 m	50 m	$Pr\{VPL \leq VAL, HPL \leq HAL\} \geq 0.999$
LPV	40 m	50 m	$Pr\{VPL \leq VAL, HPL \leq HAL\} \geq 0.999$
LPV 200	40 m	35 m	$Pr\{VPL \leq VAL, HPL \leq HAL\} \geq 0.999$

Because the vertical component is more challenging for GPS accuracy, the research presented herein focuses on evaluating the VPL during flight operations. VAL = 50 m is considered for WAAS evaluation. Calculation of the VPL is shown in APPENDIX A.

4.9 User Delay Determination

As described earlier in this chapter, WAAS estimates the ionospheric corrections and the GIVE values at the IGPs. To determine the ionospheric delay at the user's location, the user must select the surrounding IGPs and interpolate the delay values at these IGPs to compute local ionospheric delays. The IGPs selected for this calculation are based on the user's IPPs as shown in Section 3.4; information sent in a WAAS message allows the user to identify the surrounding IGPs. The selection of IGPs is conducted as follows (U.S. DOT, 1999).

Case I: User's IPP between latitudes of -55^o and 55^o:

Based on the WAAS message, three surrounding IGPs that define a triangle (as shown in Figure 4.6a) or four surrounding IGPs that define a grid (Figure 4.6b) will be selected; otherwise no ionospheric corrections are available. Note that the three-IGP selection

might have four orientations based on IPP longitude. IGP spacing in latitude and longitude is 5^{o}x5^{o}.

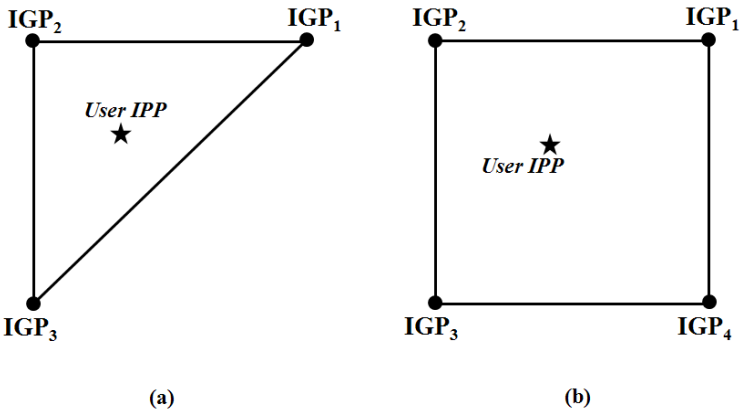

Figure 4.6: IGP selection (a) three IGPs and (b) four IGPs

Case II: User's IPP between latitudes of -55^{o} and -75^{o} or latitudes of 55^{o} and 75^{o}

Identical to Case I except IGP spacing in latitude and longitude is 10^{o}x10^{o}.

Case III: User's IPP at latitudes north of 75^{o} or south of -75^{o}

No ionospheric corrections are available at these latitudes.

To calculate the ionospheric delay and correction at a user's IPP, the user should interpolate the ionospheric corrections from the selected IGPs. The interpolation is accomplished by multiplying the delays at the surrounding IGPs by different weighting functions then summing these weighted delays as follows.

$$\tau_{v_{IPP}} = \sum_{i=1}^{q} W_i \cdot \tau_{v_i} \tag{4.20}$$

where q is number of the surrounding IGPs ($q = 3\ or\ 4$), W_i is the weighting function of the i^{th} IGP, and τ_{v_i} is the vertical ionospheric delay at the i^{th} IGP. The weighting functions and the algorithm for IGP interpolation are shown in APPENDIX B.

To obtain the ionospheric correction (IC), the user multiplies the vertical delay calculated at a given local IPP by the mapping function $M(E)$ given in Equation (4.3).

$$IC = M(E) \cdot \tau_{v_{IPP}} \tag{4.21}$$

where $\tau_{v_{IPP}}$ is the interpolated vertical delay at user's IPP. The ionospheric correction is then added to the user`s GPS pseudorange observation to remove the ionospheric propagation error and improve positioning accuracy.

The User Ionospheric Vertical Error (UIVE) bounds the residual (post-correction) pseudorange error associated with the user`s computed vertical ionospheric delay for a given satellite. It is interpolated to the user`s IPP from the GIVE defined at each IGP as follows (U.S. DOT, 1999).

$$UIVE = \sum_{i=1}^{q} W_i \cdot GIVE_i \tag{4.22}$$

where q is number of the surrounding IGPs ($q = 3\ or\ 4$) and W_i is the weighting function of the i^{th} IGP which is the same weighting function used in Equation (4.20).

4.10 Canadian WAAS

In 2004, NAV CANADA announced an agreement with the FAA to extend WAAS into Canada with the construction of four new Canadian reference stations (NAV CANADA, 2004). This service is called the Canadian WAAS (CWAAS)

In 2007, the four Canadian WRS were integrated into the WAAS network. These stations are located in Goose Bay, Gander, Winnipeg, and Iqualuit (FAA, 2007). The locations of these stations and the other WRSs within North America are shown in Figure 4.7.

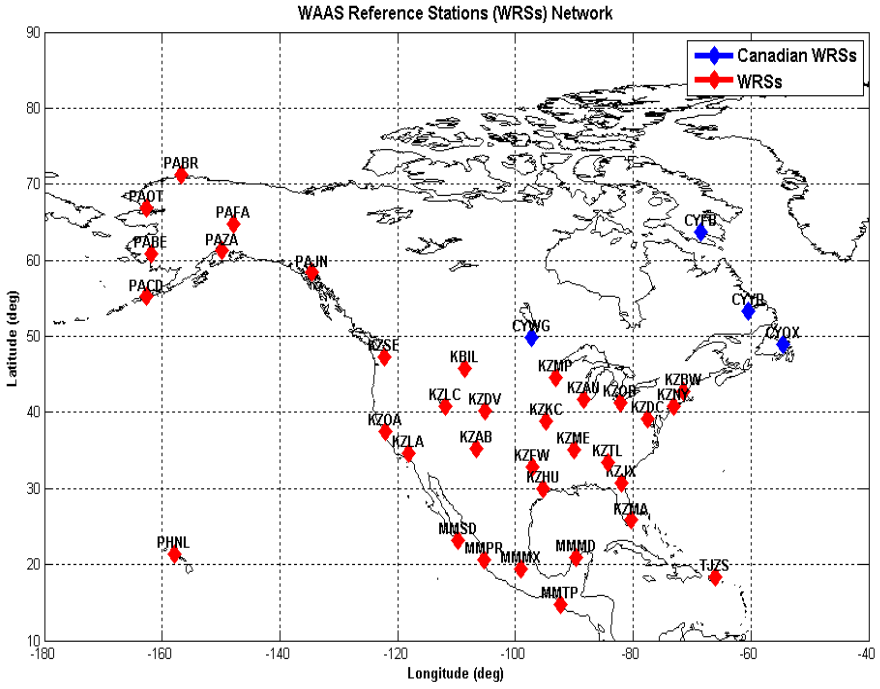

Figure 4.7: WRSs network over North America

Adding these stations into the WAAS network improves WAAS performance in the eastern part of Canada but users in the western part do not experience significant improvement (Yousuf and Skone, 2005). Therefore it is important to evaluate WAAS

performance over Canada before declaring the availability of the service especially under severe ionospheric activities. This is the major goal of this work.

4.11 Impact of Ionospheric Storms on WAAS Availability

As discussed in Chapter 3, high solar activity occurred during the periods 29 – 30 October and 20 November 2003, resulting in the development of severe SED features (Figure 4.8). During the SED periods of October and November 2003, WAAS availability was degraded (Doherty et al., 2004). Such SED effects have therefore been identified as a major challenge for WAAS, particularly in Canada where the SED plume extends through all latitudes and over the pole. Based on detailed studies of the previously observed SED events from October and November, 2003, challenging scenarios are used to test WAAS performance along with moderate and nominal ionospheric conditions.

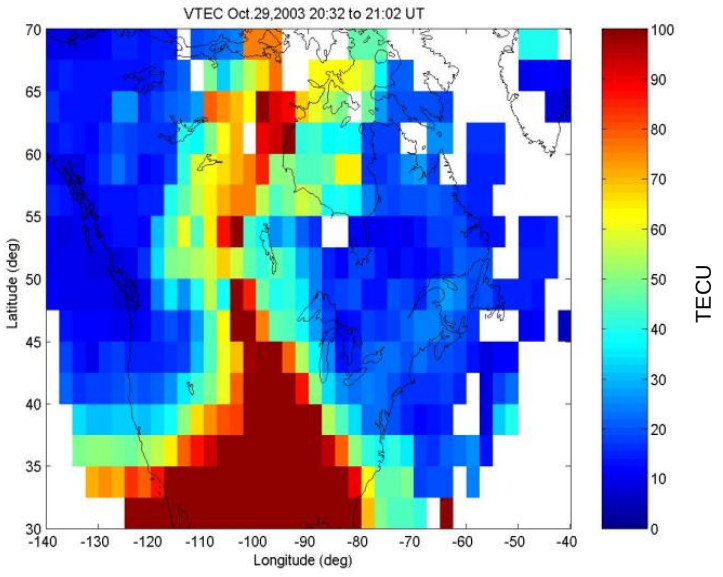

Figure 4.8: Delay map of Oct 29, 2003 SED event

WAAS availability during the SED storm of 29-30 October 2003 is shown in Figure 4.9. It can be observed that WAAS availability (green line) was degraded due to the rapid changes and the strong spatial gradients in the ionosphere (Doherty et al, 2004).

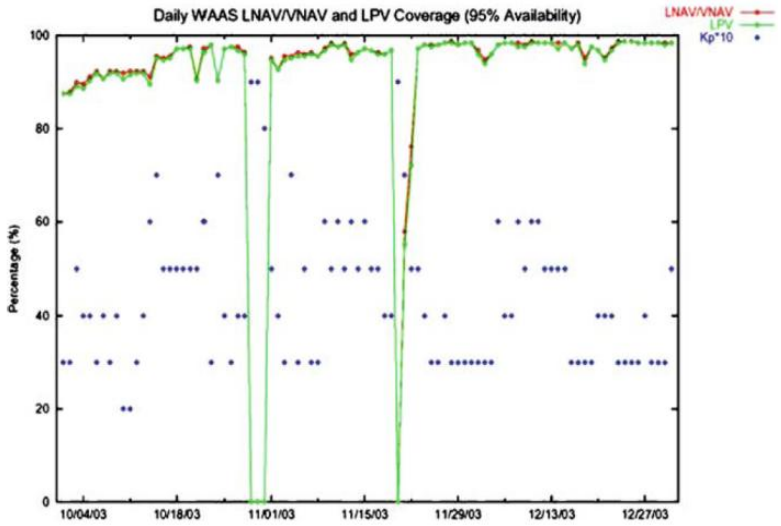

Figure 4.9: Daily WAAS coverage for the period 4 Oct. to 27 Dec., 2003 (Doherty et al, 2004)

More details about geomagnetic storm impact on WAAS for different applications can be found in Skone and Yousuf, (2007); Komjathy et al., (2004); Datta-Barua et al., (2005); Coster et al., (2007). These studies showed that SED events had a significant impact and degraded WAAS performance consistently.

Therefore, in order to investigate WAAS performance at Canadian latitudes a detailed study must be conducted of previous SED events. In Chapters 5 and 6 flexible capabilities are developed to simulate similar challenging ionospheric features over the latitudes of interest and to evaluate WAAS performance in the presence of these features using the existing WRS configuration.

Chapter Five: Data Analysis and Ionospheric Simulation

As defined previously, the Storm Enhanced Density (SED) is an ionospheric phenomenon characterized by a plume of large TEC with values exceeding 100 TECU. During SED events, WAAS availability can be degraded due to the rapid changes and the high spatial gradients in the ionosphere. In order to test the WAAS under such conditions, characteristics of the SED must first be investigated. In this chapter studies of the SED events on 29-30 October and 20 November 2003 are conducted. Approximately 500 GPS ground reference stations over North America are selected to calculate TEC values and monitor spatial and temporal characteristics of the ionosphere over Canada during the SED events. Detailed analyses of GPS TEC observations are also conducted to determine ionospheric characteristics inside the plume of the SED and quantify gradients at the edges of the plume; spatial variations from the quiet ionospheric regions (outside the SED) to the plume (inside the SED) are also evaluated. Single GPS satellite observations are selected to monitor the temporal evolution and spatial correlation of VTEC during these events.

All the VTEC series used in this study are generated using TEC MODEL© software (Skone, 2000), which was developed at the University of Calgary. Moreover, a study of high-frequency variations of TEC values is presented. Spectral analysis is applied to TEC series and the frequency components (low and high frequency components) are separated. For this purpose, a fourth-order Butterworth filter was chosen. From the high frequency

component, magnitudes of variations are determined to establish a range of behaviour expected during different stages of ionospheric activity. From such results TEC observations can be simulated for various ionospheric event scenarios.

5.1 SED during 29-30 October 2003

One of the most severe SED events affecting CONUS and part of south-western Canada took place on 29-30 October 2003 (DOY 302-303). As discussed earlier, during this storm WAAS service was degraded. Therefore, studying this event is important to assess WAAS performance evaluation under similar future events.

Figure 5.1and Figure 5.2 show the sunspot numbers and the planetary Kp indices for this period. From both figures it is observed that the sunspot numbers increased during this period which means the sun became highly active and affected the earth's ionosphere. The Kp index reached a value of 9 in response to the solar activity.

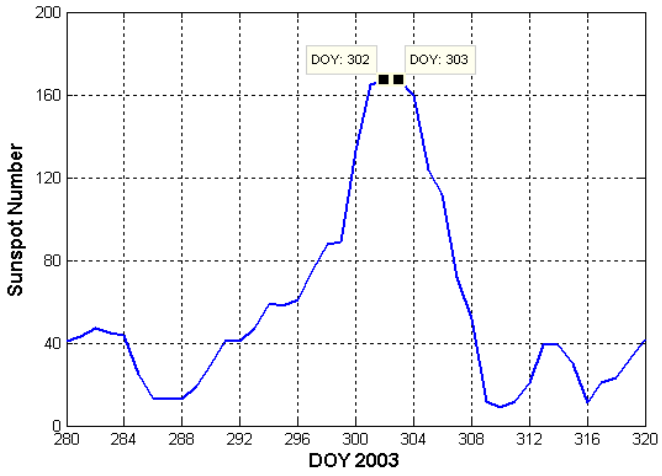

Figure 5.1: Sunspot numbers between DOY 208 and DOY 320

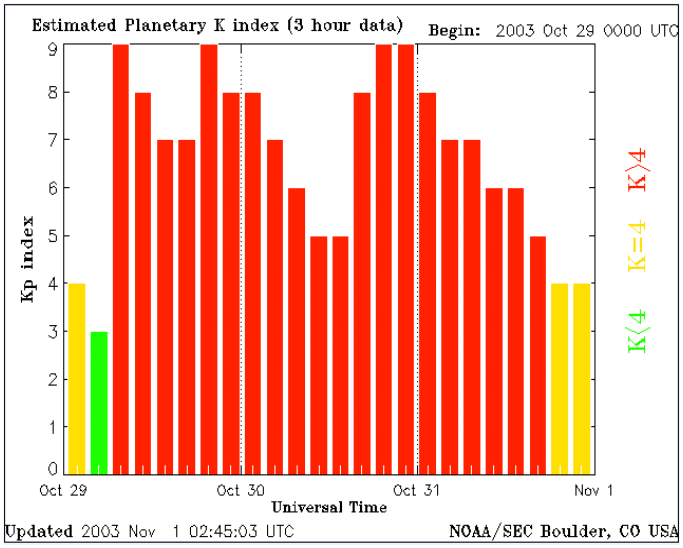

Figure 5.2: Planetary Kp indices between 29 Oct and 1 Nov 2003

These events started approximately 1100 UT on 28 October and commenced in the earth's environment at 0600 UT on 29 October. Further coronal mass ejections at approximately 2100 UT on 29 October and 1600 UT on 30 October resulted in a continuous effect for several days (Yousuf and Skone, 2005).

Figure 5.3 and Figure 5.4 show the TEC maps of SED during DOY 302 and 303 (29-30 October 2003). These TEC maps were derived with $2.5^{o}\times2.5^{o}$ grid size resolution and were generated from dual frequency GPS observations at more than 500 reference stations distributed over North America. The TEC maps were not smoothed and the details observed are due to the large amount of data used in the processing. The two SED events developed over the CONUS and southwestern Canada for extended periods 1800 UT 29 October to 0100 UT 30 October and 1800 UT 30 October to 0200 UT 31 October.

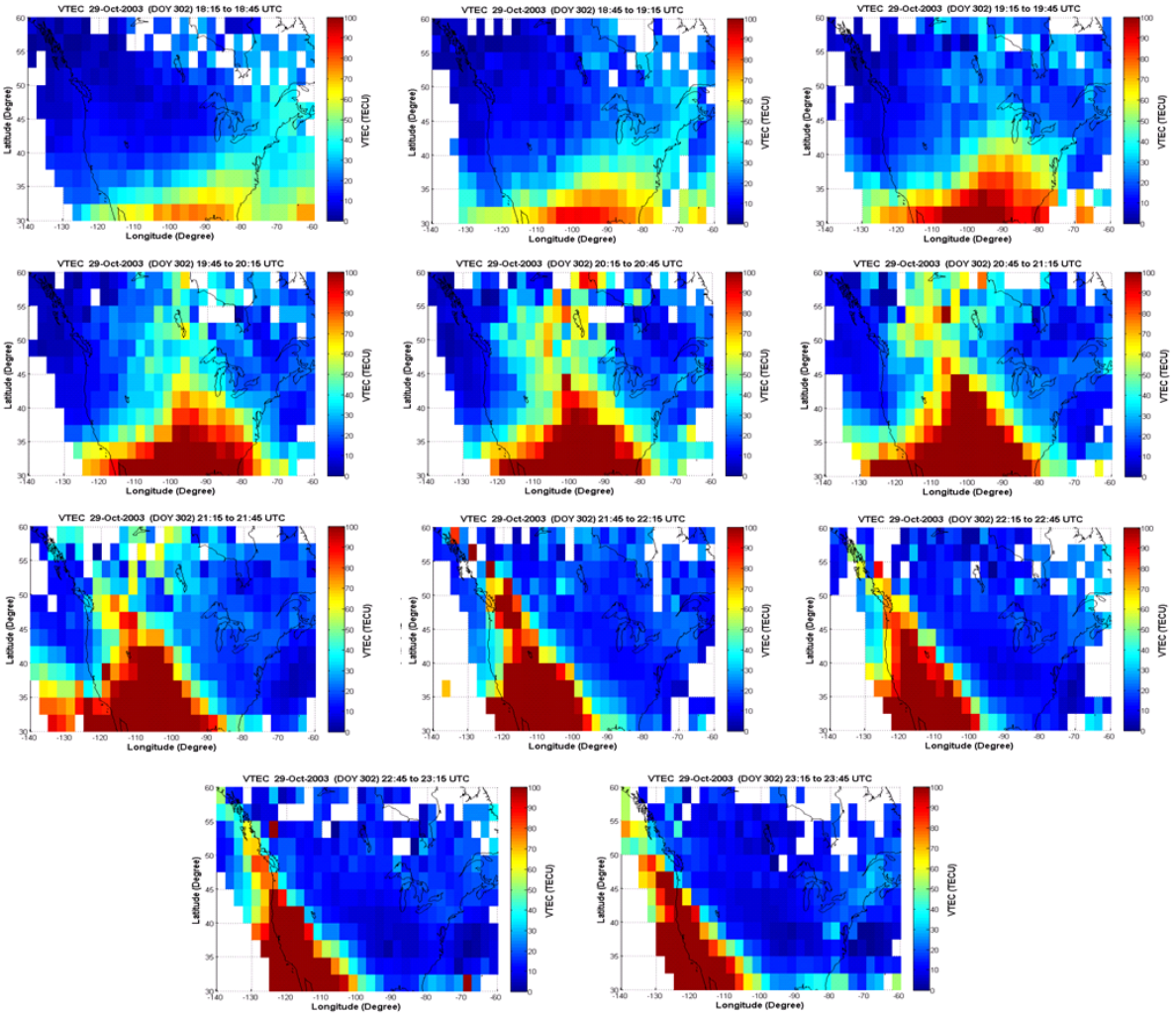

Figure 5.3: SED on 29 October 2003 between 1815 UT and 2345 UT

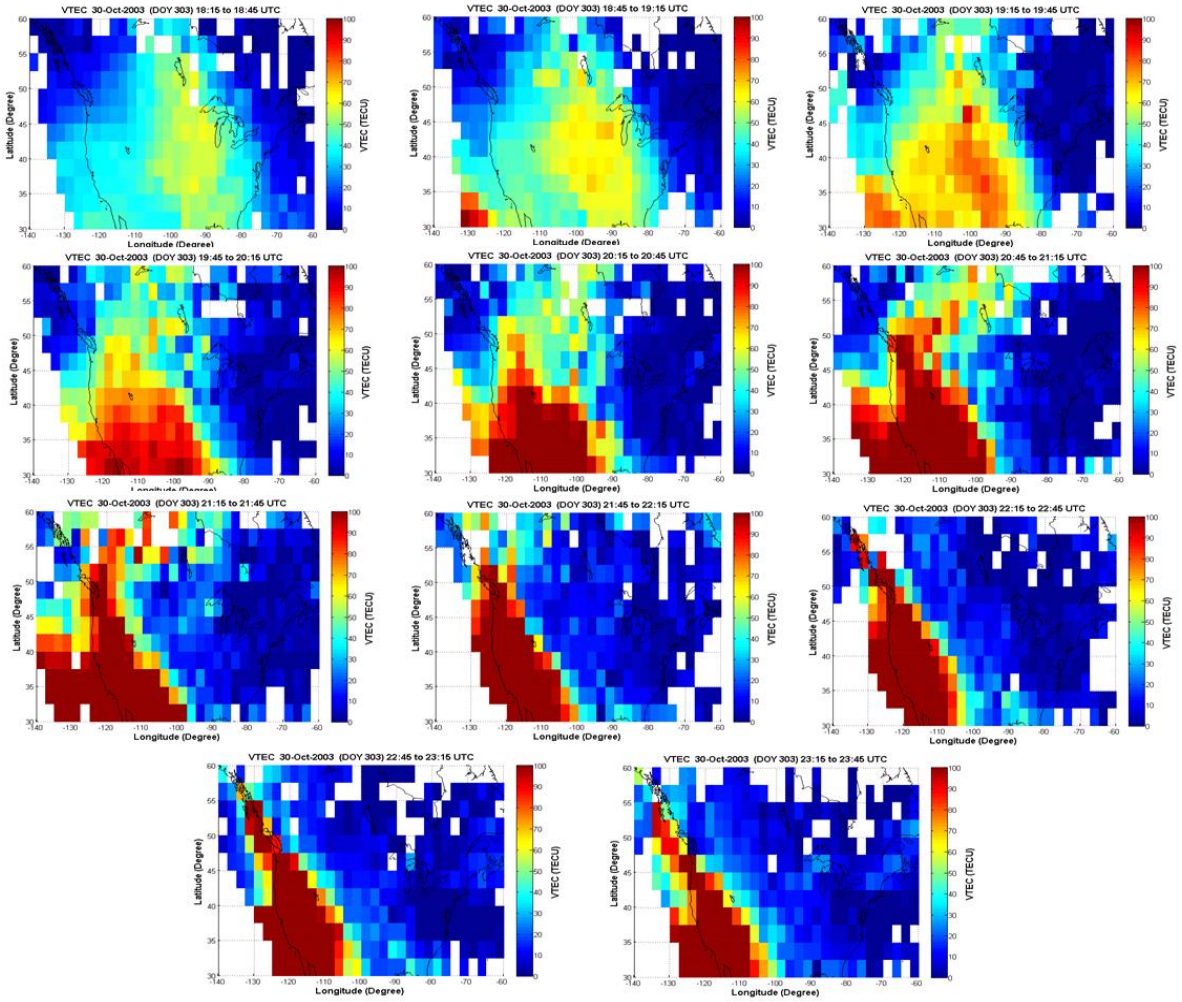

Figure 5.4: SED on 30 October 2003 between 1815 UT and 2345 UT

In the following sections, a study of each day is conducted separately. The studies are for the time periods 2045 to 2115 UT on 29 and 30 October when severe SED gradients developed across the CONUS and southwestern Canada.

5.1.1 SED on 29 October 2003

To study the spatial characteristics of the SED observed on 29 October, the period of 2045 UT to 2115 UT was chosen due to the severe gradients in this period. Two GPS

reference stations from The International GNSS Service (IGS) network have been chosen to study TEC variations.

Figure 5.5 shows the SED for the period 2045 to 2115 UT. The base of the SED plume over North America was about 50 degrees in width extending from longitude -80^{o} to -130^{o}. Large gradients at the edges of the SED plume extend approximately 10 degrees in width westward and northward over the Canadian latitudes.

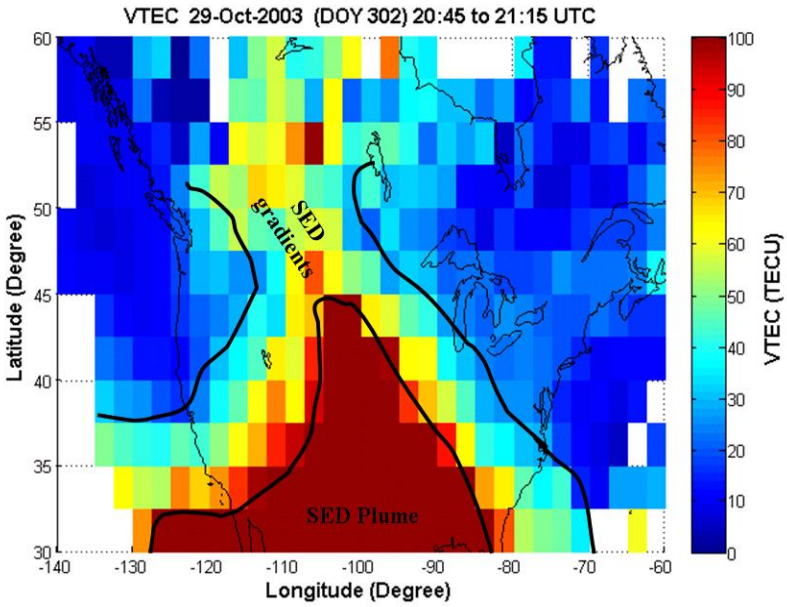

Figure 5.5: TEC map of the SED on 29 October 2003 between 2045 UT to 2115 UT

To study the TEC variations, two IGS stations had been chosen; "ALBH" station (Latitude: 48.3897^{o} and Longitude: -123.4874^{o}) and "AMC2" (Latitude: 38.8031^{o} and Longitude: -104.5246^{o}). From these two stations, different satellite lines-of-sight are chosen to derive and study individual TEC values. The IPPs corresponding to these satellite lines-of-sight are plotted superposed on the SED map to identify appropriate

observations for this study. PRN 8 for ALBH and PRNs 13 and 17 for AMC2 are chosen in this manner. The IPPs for these satellite observations are shown in Figure 5.6. A cut-off elevation angle of 15^{o} is used for the analysis.

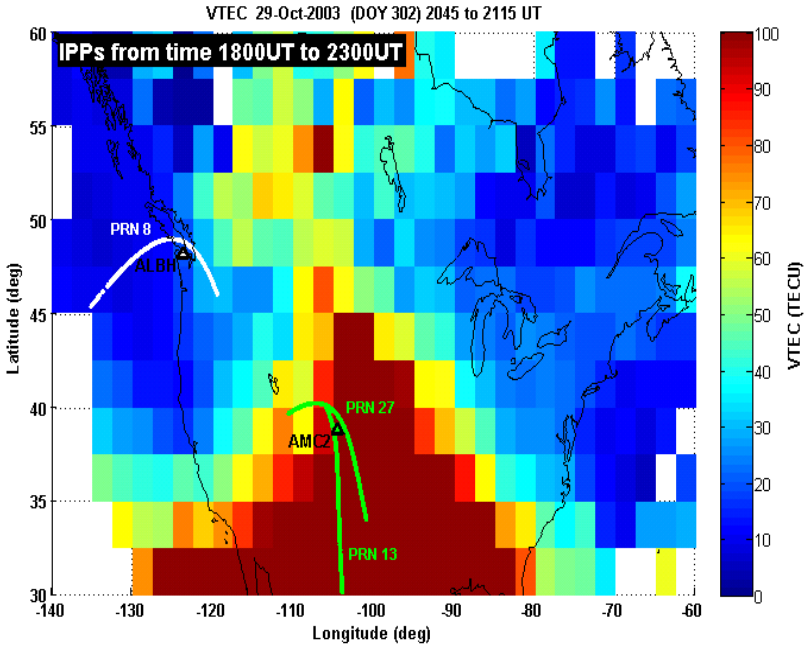

Figure 5.6: IPPs corresponding to PRN 8 at ALBH station and PRNs 13 and 27 at AMC2 station

5.1.1.1 ALBH Station – PRN 8

The VTEC series corresponding to PRN 8 at ALBH station is shown in Figure 5.7. The effect of the SED started at 2100 UT with a sharp increase in TEC values due to SED gradients; TEC values increased from ~25 TECU to ~120 TECU in one hour. At 2200 UT, the line-of-sight entered the SED plume with TEC values near 120 TECU until the line-of-sight moved out the plume at 2215 UT and the values decreased to ~25 TECU again in approximately one hour.

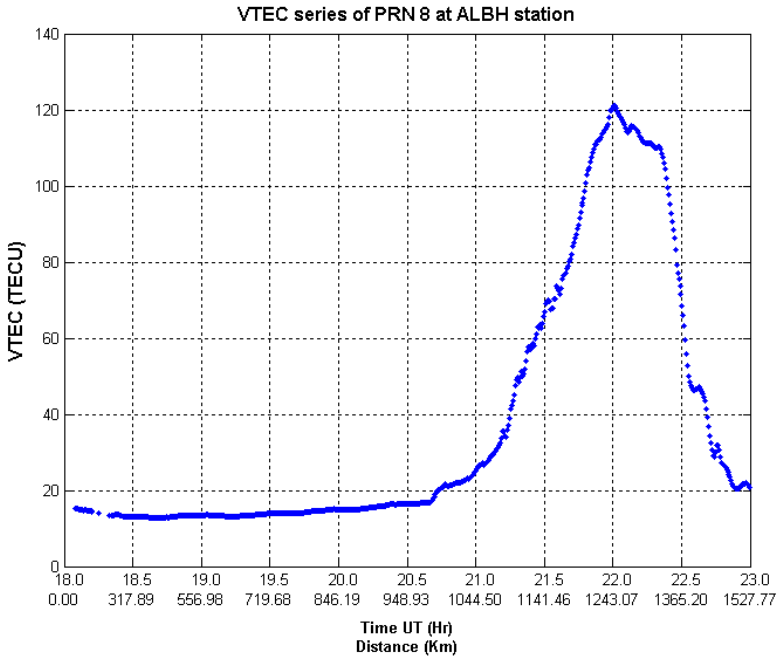

Figure 5.7: VTEC series of PRN 8 at ALBH station

The IPPs corresponding to this VTEC series are shown in Figure 5.8a-c. It is observed that the IPPs enter the plume (Figure 5.8a and 5.8b) consistent with the increase in VTEC values; then the IPPs move through a large gradient into a quiet region, consistent with the decrease in VTEC values (Figure 5.8c).

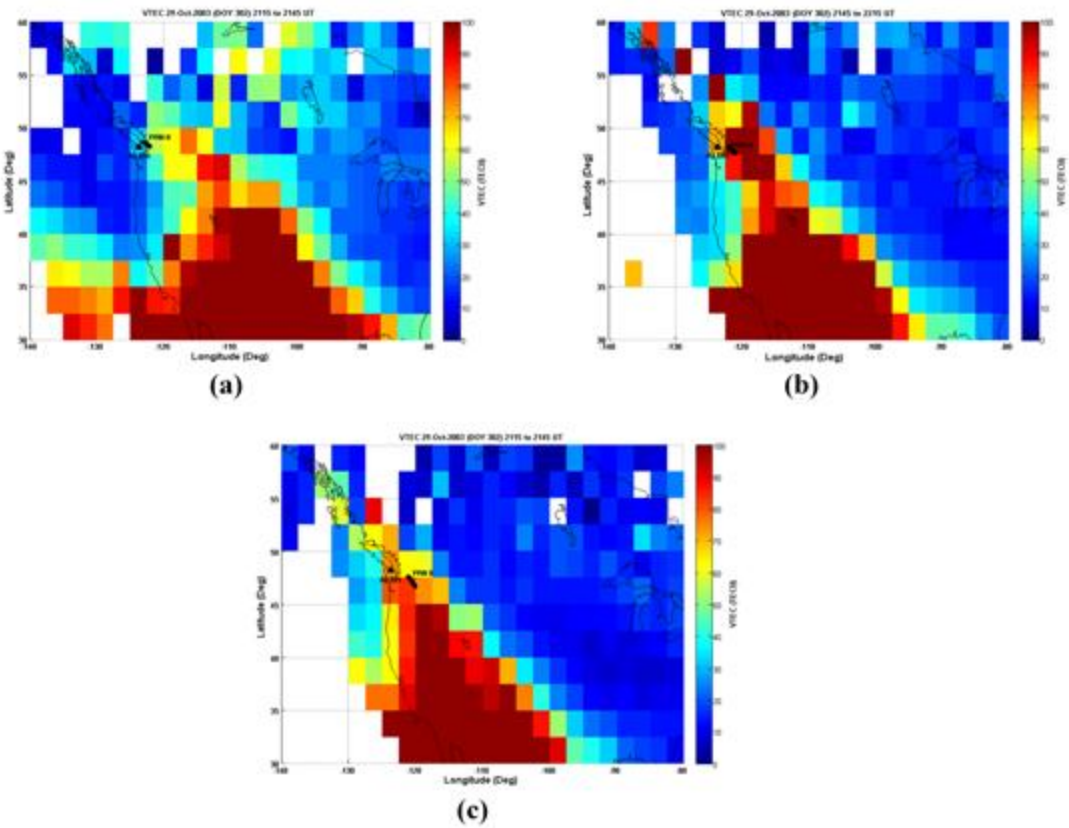

Figure 5.8: IPPs trajectories of the LOS between PRN 8 and ALBH station

Spectral analysis is conducted to further study the TEC variations. A Butterworth filter is implemented and High Pass (HP) and Low Pass (LP) filtering is conducted. The filter cut-off frequency is chosen based on the Power Spectral Density (PSD) for the VTEC series which provides information about the power of the signal as a function of the wavelength. As the VTEC series is not evenly spaced (as a function of distance), the Lomb-Scargle Algorithm (see APPENDIX C) is used to calculate the PSD shown in Figure 5.9. From this figure, a cutoff wave number of 0.005 km^{-1} (wavelength 200 km) is chosen and implemented in the filter. The LP and HP components of the VTEC series are shown in Figure 5.10. It is observed that the SED gradients cause high frequency

variations with amplitudes of approximately 10 TECU for the HP component; in this case the Root Mean Square (RMS) value is 3.62 TECU.

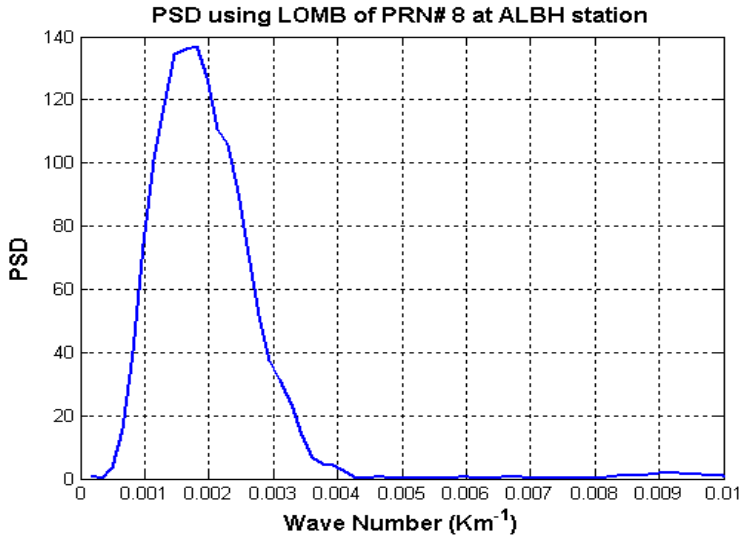

Figure 5.9: PSD of the VTEC series of PRN 8 at ALBH station

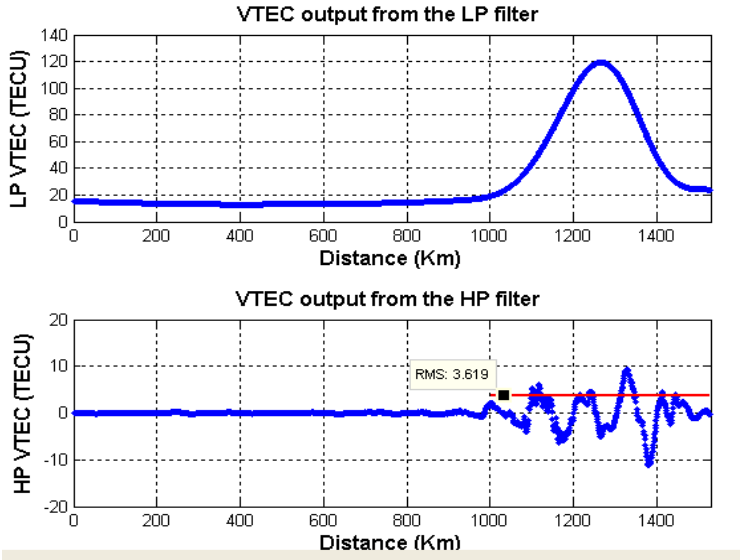

Figure 5.10: LP and HP components of PRN 8 VTEC series at ALBH station

5.1.1.2 AMC2 – PRN 27

Two satellites at AMC2 were chosen to further study the SED gradients and the plume effects. In this section, PRN 27 observations are analysed.

PRN 27 observations at AMC2 are affected by ionospheric gradients between 2000 and 2100 UT; high TEC values in the plume are observed at approximately 2115 UT with the line-of-sight passing through large gradients again between 2130 and 2230 UT. The IPPs for PRN 27 between 2015 and 2215 UT are shown in Figure 5.11(a)-(d).

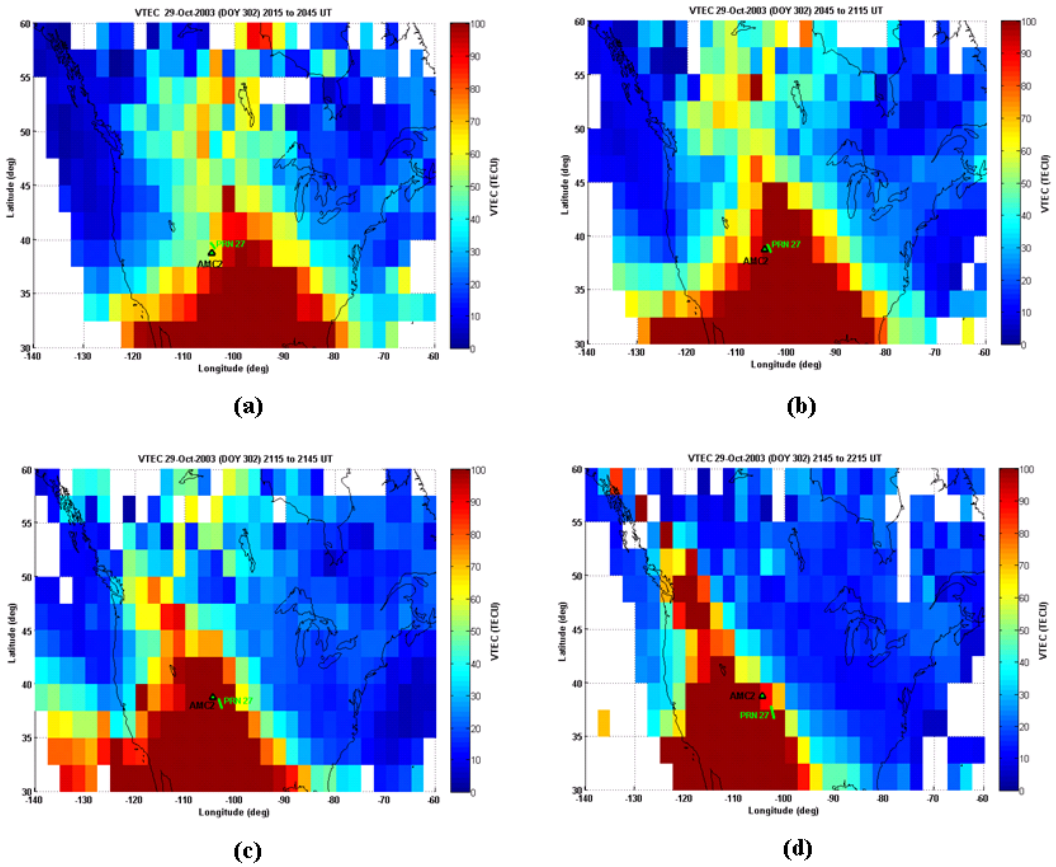

Figure 5.11: IPPs trajectories of the LOS between PRN 27 and AMC2 station

The VTEC series for PRN 27 is shown in Figure 5.12. Similar to PRN 8 observations at ALBH, two distinct walls of the plume are observed (i.e., sharp increases and decreases in TEC values). At 2000 UT, TEC values increase from ~40 TECU to ~170 TECU in one hour. A drop in TEC values occurs as the IPPs move away from the SED plume; during the period 2130 UT to 2230 UT the VTEC values dropped from ~160 TECU to ~50 TECU in one hour. Another gradient effect is observed at approximately 2245 UT.

The effects observed here are similar to those for ALBH; however the delay values are higher at station AMC2.

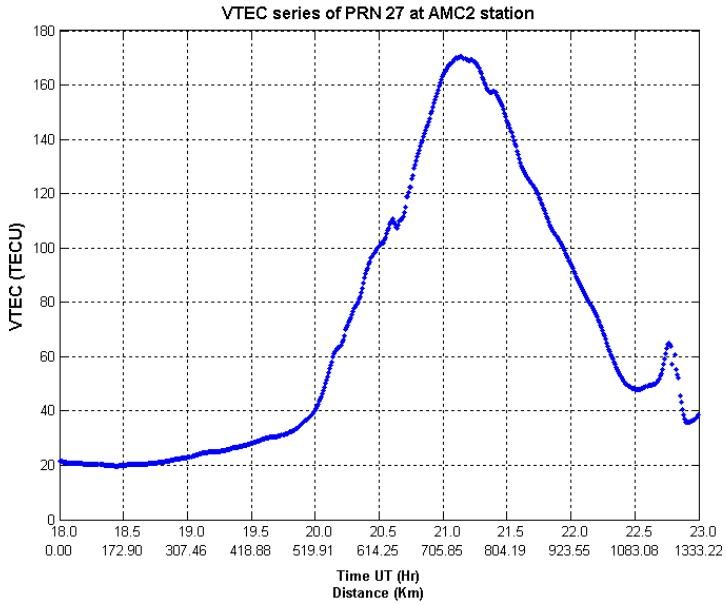

Figure 5.12: VTEC series of PRN 27 at AMC2 station

To study high frequency TEC variations for this case, a filter cut-off wave number of 0.004 km^{-1} (250 km wavelength) is chosen based on the PSD shown in Figure 5.13.

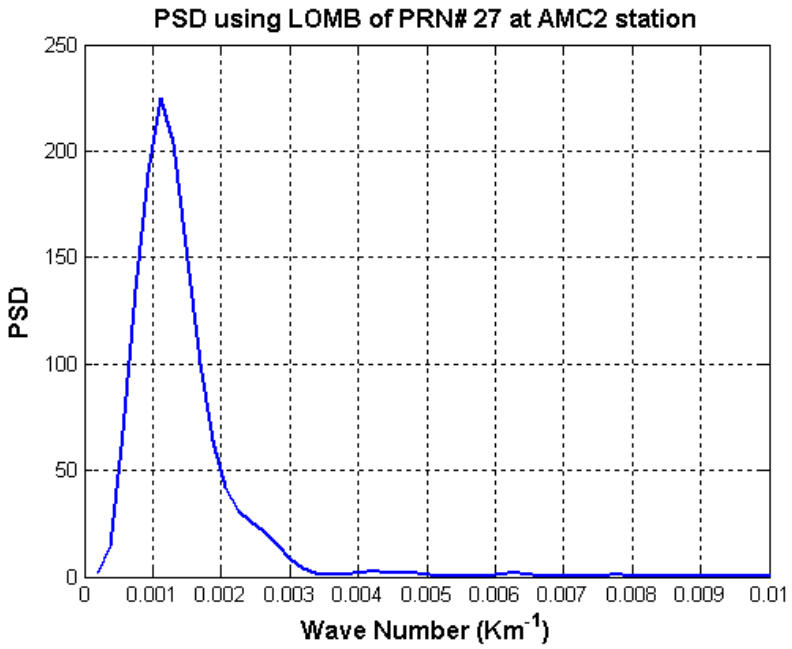

Figure 5.13: PSD of the VTEC series of PRN 27 at AMC2 station

By filtering the VTEC series, the LP and HP components (shown in Figure 5.14) are separated. Studying the HP component of the series it is observed that variations exist with amplitudes of approximately 10 TECU and an RMS value of ~ 4.4 TECU.

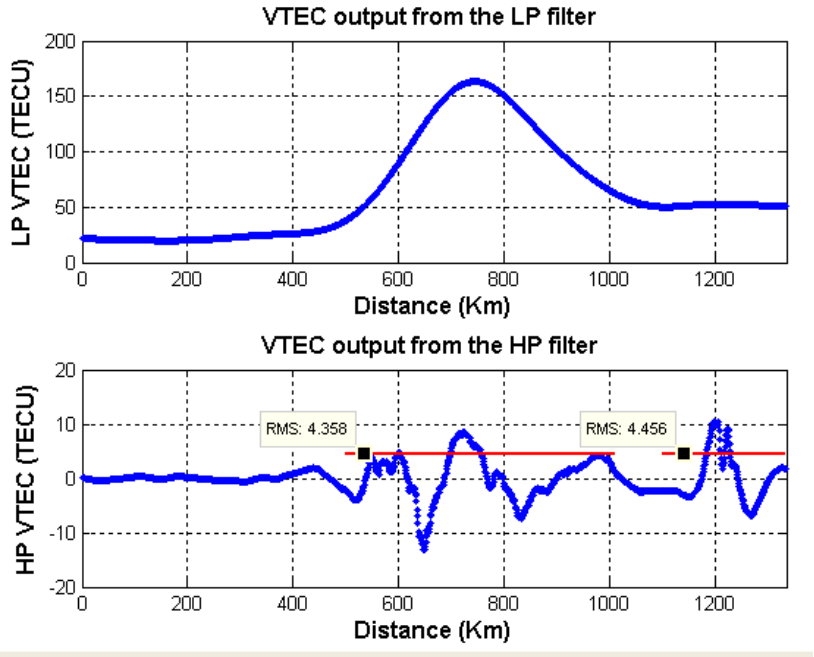

Figure 5.14: LP and HP components of PRN 27 VTEC series at AMC2 station

5.1.1.3 AMC2 – PRN 13

Another satellite is chosen for station AMC2 to study SED plume effects. PRN 13 is identified and the satellite-receiver line-of-sight enters the SED region around 2000 UT. Effects continued until 2115 UT as shown in Figure 5.15.

The VTEC values for PRN 13 are shown in Figure 5.16. Values increase from ~ 25 TECU to ~180 TECU in three hours (from ~ 1830 to 2130 UT).

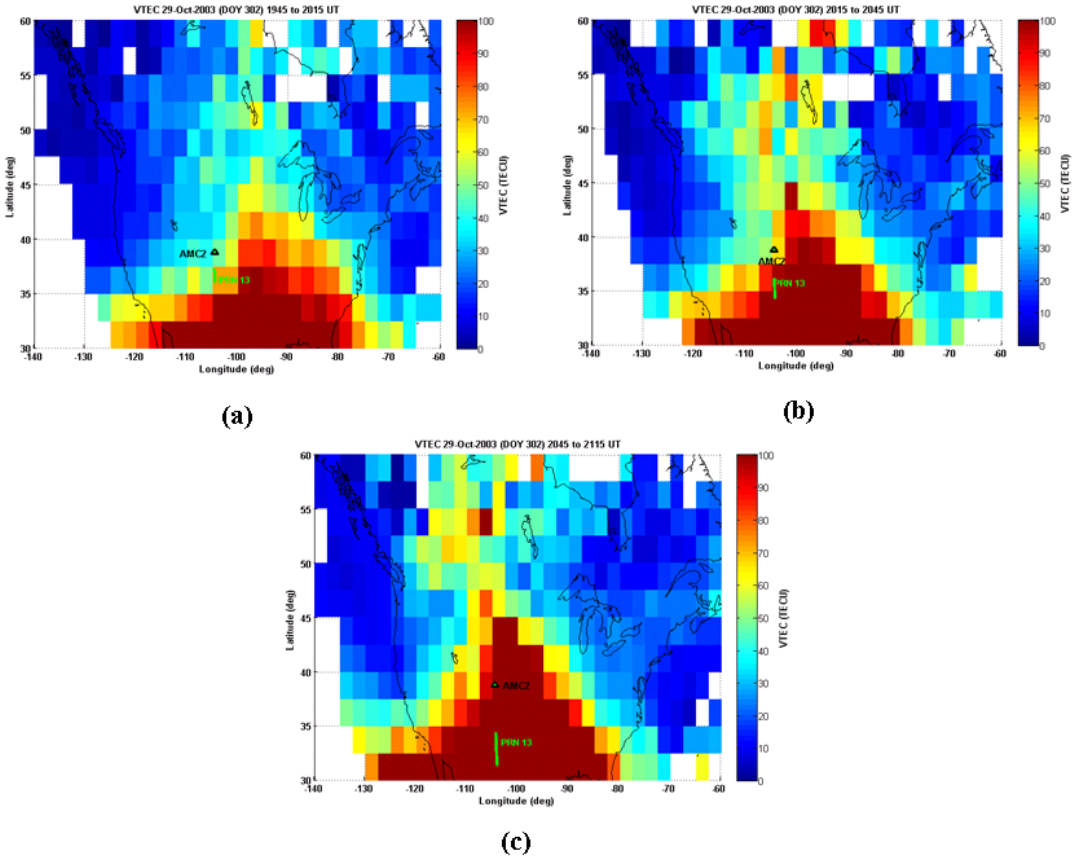

Figure 5.15: IPPs trajectories of the LOS between PRN 13 and AMC2 station

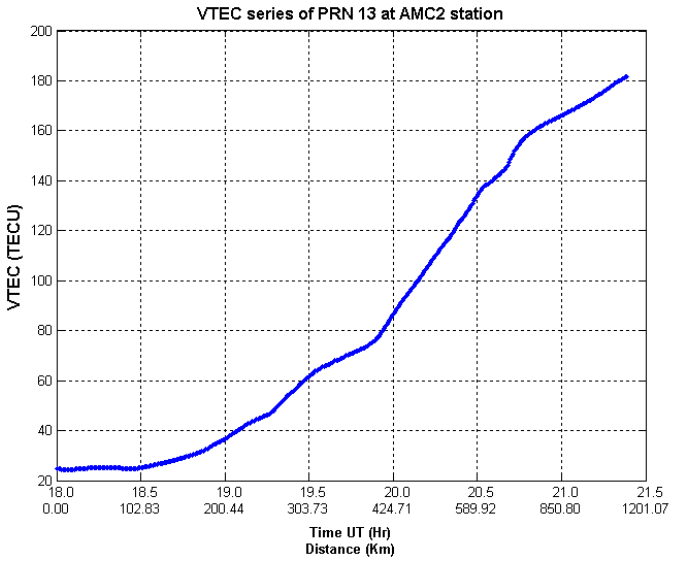

Figure 5.16: VTEC series of PRN 13 at AMC2 station

To study the high frequency component of the VTEC series, a fourth-order Butterworth filter was implemented with cut-off wave number 0.005 km^{-1} (wavelength 200 km) based on the PSD in Figure 5.17.

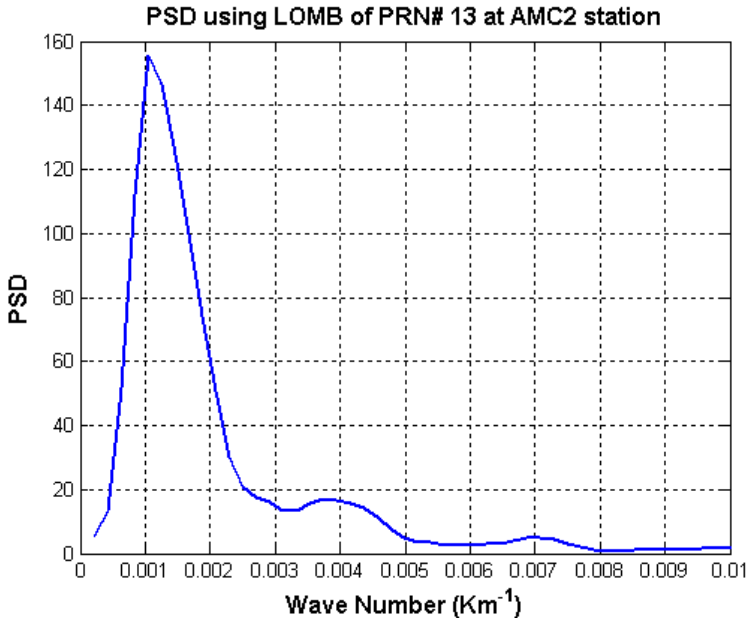

Figure 5.17 PSD of the VTEC series of PRN 13 at AMC2 station

From the high frequency component shown in Figure 5.18, it is observed that VTEC variations in this case are much lower than the previous two cases (ALBH – PRN 8 and AMC2 – PRN 27). The high frequency amplitudes are approximately 2 TECU with an RMS value of 1.02 TECU. Accordingly, it is determined that the TEC gradients and structures can vary within the SED feature.

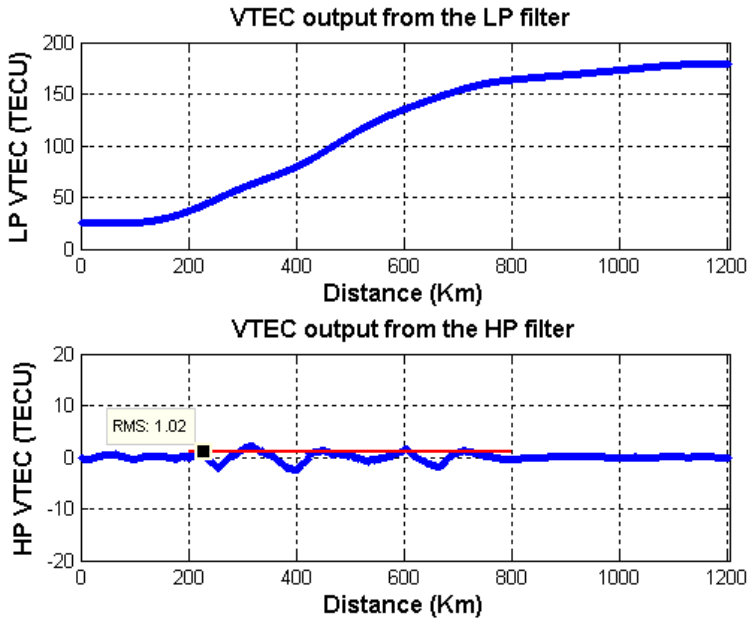

Figure 5.18: LP and HP components of PRN 13 VTEC series at AMC2 station

5.1.2 SED on 30 October 2003

On 30 October 2003, another SED was observed over North America and particularly the west coast at approximately at 2100 UT, resulting in enhanced TEC values over this region.

A spatial plot of this event for the period 2045-2115 UT is shown in Figure 5.19. This figure was generated using more than 500 GPS ground reference station observations with $2.5^{o}\times2.5^{o}$ grid resolution. This figure shows the spatial characteristics of this SED event. This time period was chosen for analysis because maximum gradients occurred. The SED plume base extended from ~-100^{o} to ~-135^{o} longitude forming a base of 35 degrees width in the western region of North America. The plume narrows at higher latitudes with approximately 25 degrees distance from the base to the top. Gradients at

the SED plume edges have widths of 5-10 degrees extending and spreading to higher latitudes.

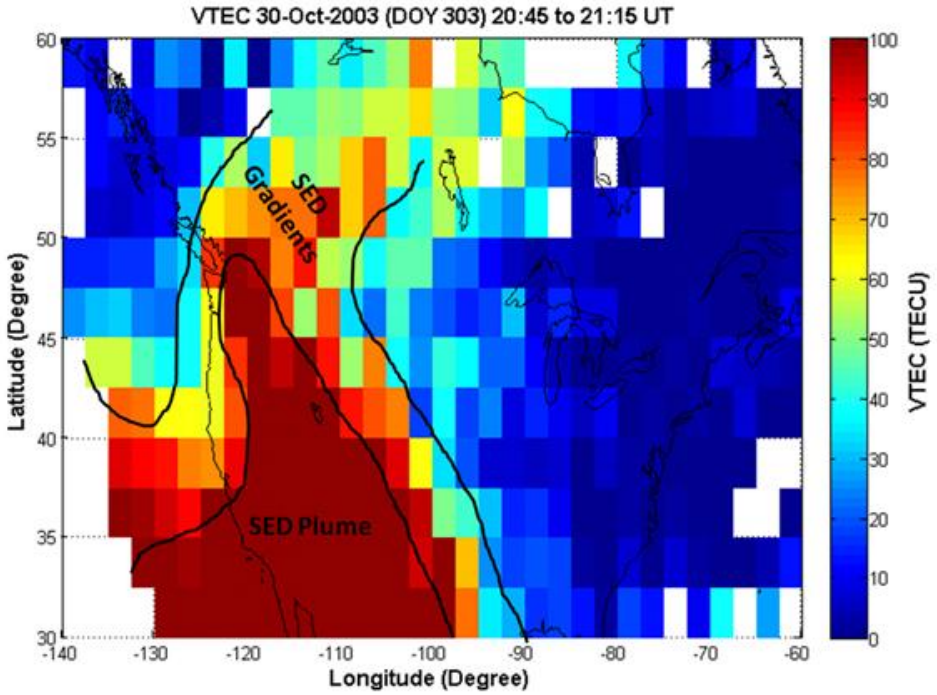

Figure 5.19: TEC map of the SED on 29 October 2003 between 2045 UT to 2115 UT

To study the effect of this SED event using TEC observations, three satellites at different stations are chosen. The three stations are ALBH (Latitude: 48.3897^{o} and Longitude:-123.4874^{o}), WILL (Latitude: 52.2369^{o} and Longitude:-122.1678^{o}), and AMC2 (Latitude: 38.8031^{o} and Longitude:-104.2546^{o}). At each station, one satellite is selected to study the SED gradients and structures.

5.1.2.1 ALBH Station – PRN 8

The VTEC series for PRN 8 is plotted as a function of time and distance in Figure 5.20.

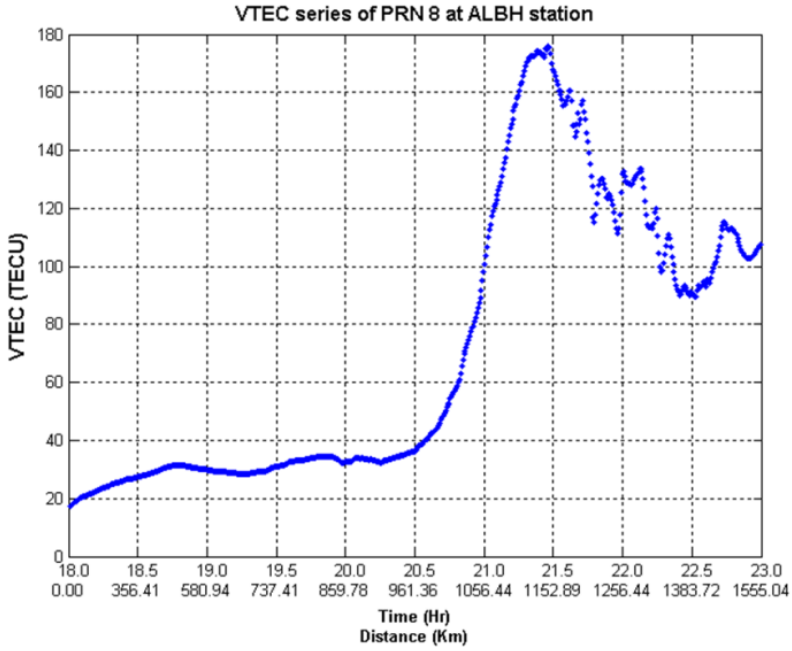

Figure 5.20: VTEC series of PRN 8 at ALBH station

Between 1800 and 2030 UT, the VTEC values are in the range 20-30 TECU which could be considered relatively quiet. At ~2030 UT, the SED plume starts to affect the satellite observations. The IPPs pass through a strong gradient and VTEC values increase from ~30 TECU to ~175 TECU within one hour. This gradient exists in a region approximately 100 km wide. Effects of the SED continued until approximately 2300 UT.

The VTEC values were high and low pass filtered using a fourth-order Butterworth filter with cutoff frequency 0.006 km^{-1} (wavelength 167 km). The cut-off frequency was determined from the PSD in Figure 5.21.

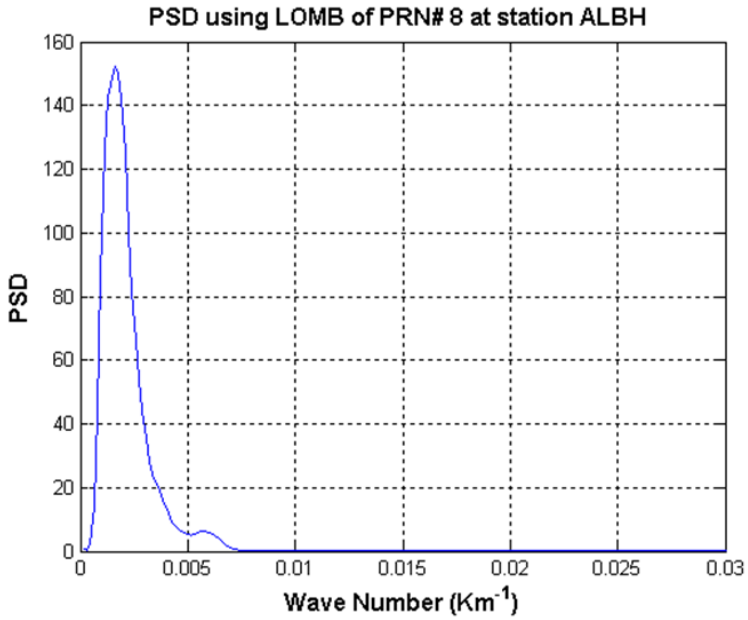

Figure 5.21: PSD of PRN 8 VTEC series at ALBH station

These HP and LP components are shown in Figure 5.22.

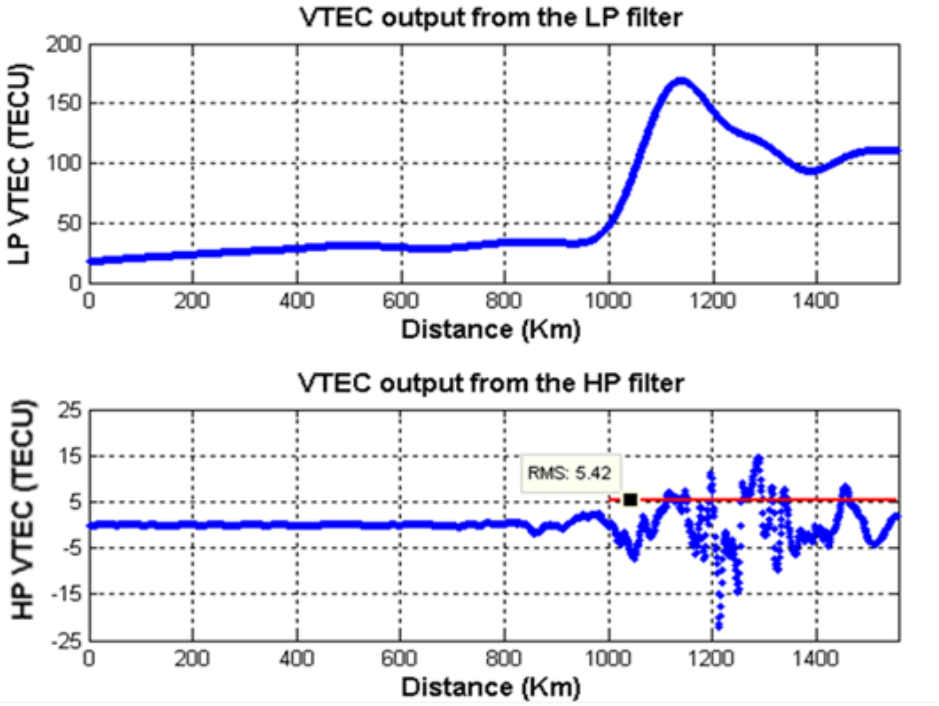

Figure 5.22: LP and HP components of PRN 8 VTEC series at ALBH station

A high RMS value of 5.42 TECU is observed for the HP component due to highly variable ionospheric structures within the SED region.

5.1.2.2 WILL Station – PRN 8

The VTEC series for PRN 8 is shown in Figure 5.23. Effects of the SED are observed at approximately 1930 UT where the satellite line-of-sight enters the region of high ionospheric activity. At approximately 2045 UT, the line-of-sight enters the SED plume and VTEC values increase from ~35 TECU to ~150 TECU. The satellite IPPs move out of the SED region 2145 UT and VTEC values decrease to ~35 TECU again.

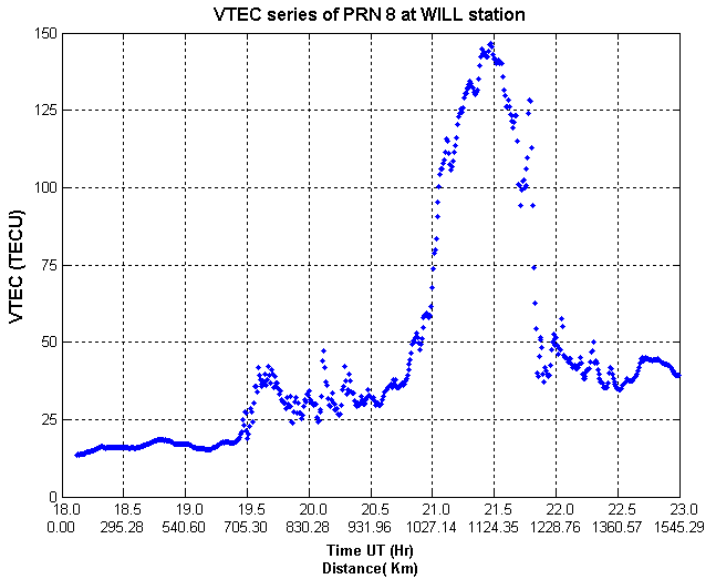

Figure 5.23: VTEC series of PRN 8 at WILL station

To study the high frequency variations, the high frequency VTEC component is separated from the low frequency component using the fourth order Butterworth filter with cut-off wave number 0.006 km^{-1} (wavelength 167 km) as chosen from the PSD shown in Figure 5.24.

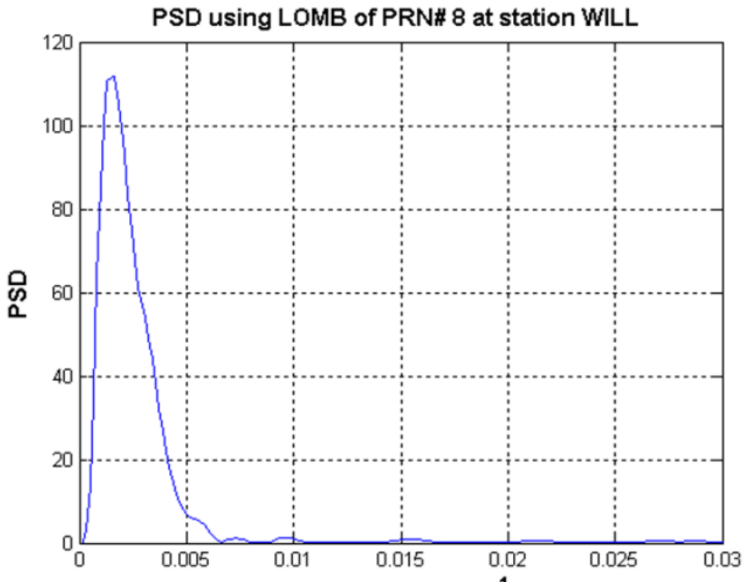

Figure 5.24: PSD of the VTEC series of PRN 8 at WILL station

The HP and LP VTEC components are shown in Figure 5.25 with the series divided into four regions. Regions one and four have low absolute VTEC values with high-frequency (short-wavelength) structure. The HP RMS values in these two regions were 4.16 and 2.545 TECU, respectively. Regions two and three include the plume and larger gradients at its edges. The HP RMS values were 6.224 and 13.4 TECU, respectively, for regions two and three.

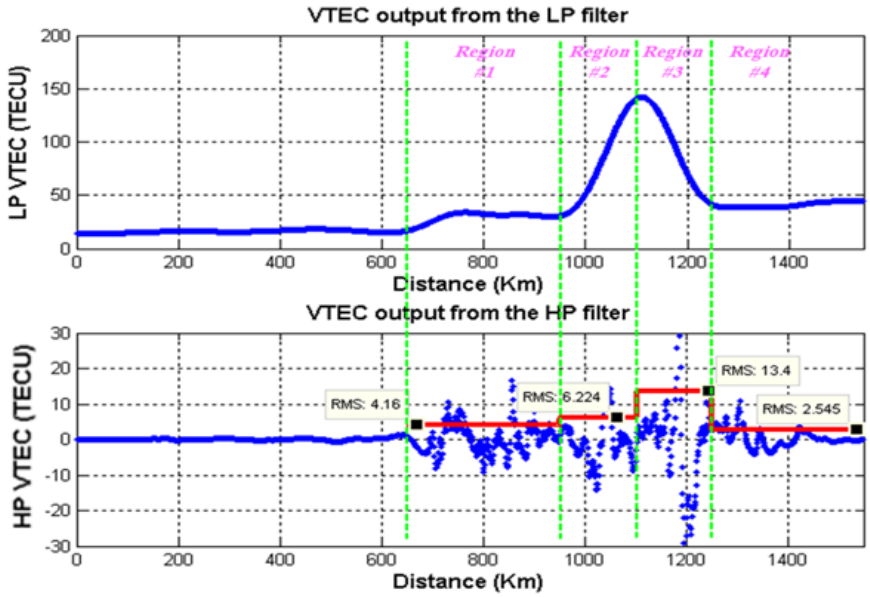

Figure 5.25: LP and HP components of PRN 8 VTEC series at WILL station

5.1.2.3 AMC2 Station – PRN 13

At 1800 UT storm effects were observed for PRN 13 observations; the VTEC value was ~70 TECU at this time, as shown in Figure 5.26.

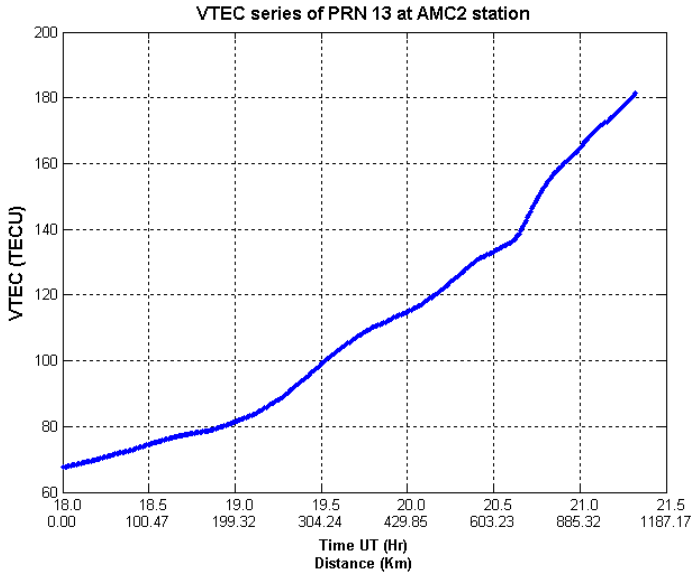

Figure 5.26: VTEC series of PRN 13 at AMC2 station

The TEC values increase smoothly since the satellite-receiver line-of-sight is inside the plume throughout the period, The VTEC value reached ~180 TECU at approximately 2115 UT. A fourth-order Butterworth filter is implemented for this VTEC series with cut-off wave number 0.005 km^{-1} (200 km wavelength) as chosen based on the PSD shown in Figure 5.27.

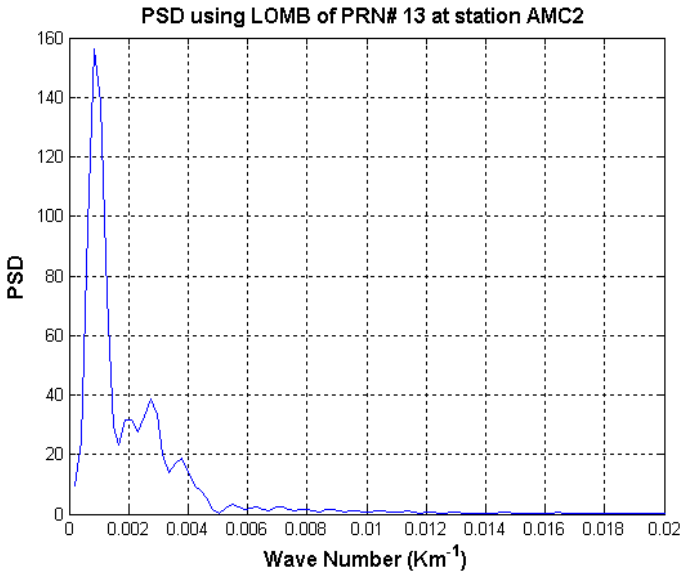

Figure 5.27: PSD of the VTEC series of PRN 13 at AMC2 station

As expected, the high frequency component (HP) does not show any high variations in Figure 5.28. The TEC variations were less than 1 TECU most of the time and the HP RMS value for this time period was 0.39 TECU.

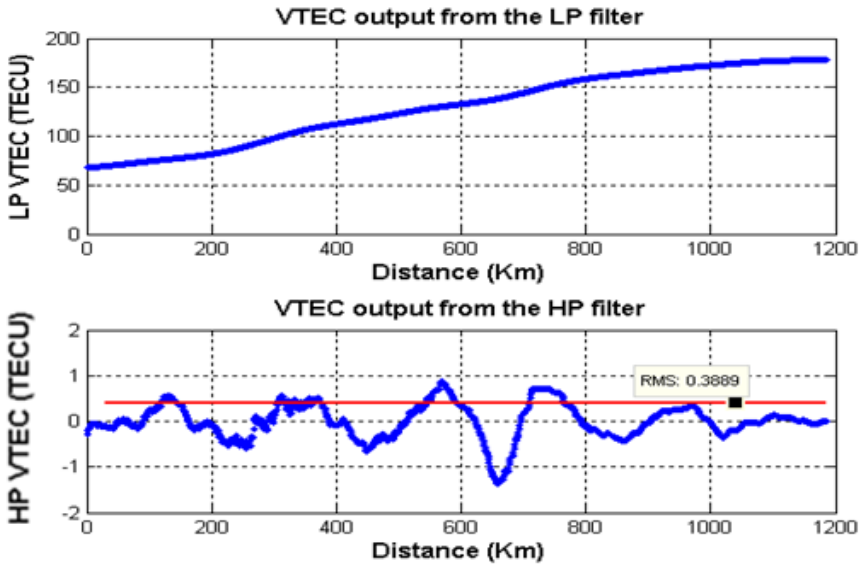

Figure 5.28: LP and HP components of PRN 13 VTEC series at AMC2 station

5.2 SED during 20 November 2003

A large geomagnetic storm occurred on 20 November 2003. This is observed in the sunspot numbers and the Kp index shown in Figure 5.29. It is noted that on 20 November the sunspot number increased significantly and the Kp index reached 9. These values indicate severe ionospheric activity event and high probability of SED.

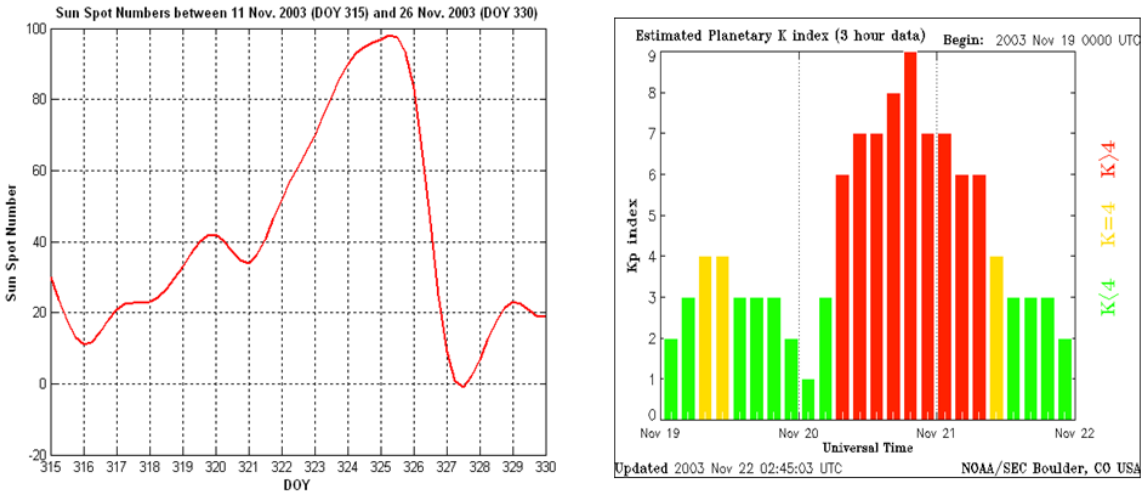

(a) (b)

Figure 5.29: The (a) sunspot number and (b) planetary Kp index during 20 November 2003 storm

Similar to the October event, SED was observed for an extended period (1900-2100 UT) on 20 November in North America. TEC maps in Figure 5.30 show the TEC observed over North America during this period. These maps are generated in the same manner as those in Section 5.1 using dual frequency GPS observations from approximately 500 stations across North America. Satellite TEC observations from each station are generated using the TECMODEL© software, and all observations are binned into $2.5^{o}\times2.5^{o}$ grids to determine spatial distribution of VTEC.

During two hours of interest (1900 to 2100 UT), the SED evolved westward and northward over North America. Between 1930 and 2000 UT, the SED reached its maximum size and gradients; therefore, this time period is chosen to study the spatial characteristics of this SED event.

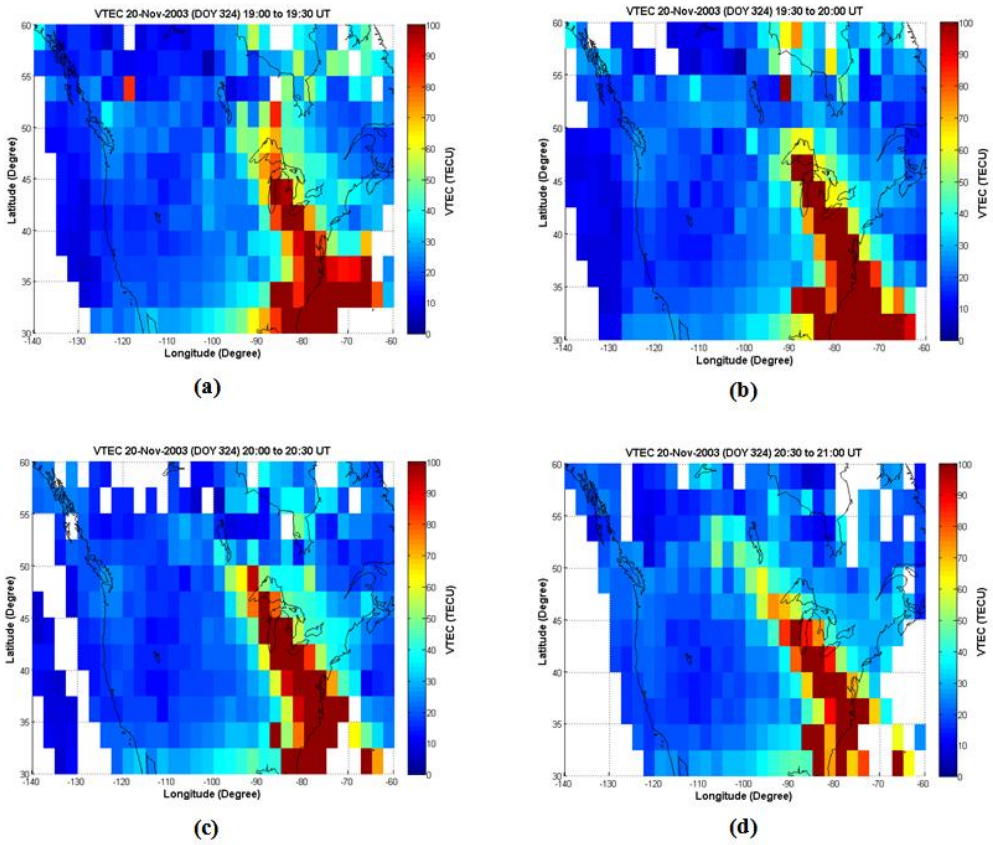

Figure 5.30: TEC maps of 20 November 2003 SED

Figure 5.31 shows the TEC map on 20 November for the time period 1930 - 2000 UT. The SED plume has a 20-degree width base extending from approximately -65^{o} to -85^{o} longitude over North America. The plume extends spatially in the northwest direction where the top of the SED plume is at approximately 45^{o} latitude (~15^{o} away from the base observed over North America). SED gradients exist in regions approximately 5-10 degrees width surrounding the SED plume extending in the North and Northwest directions. The TEC values inside the SED plume exceed 100 TECU.

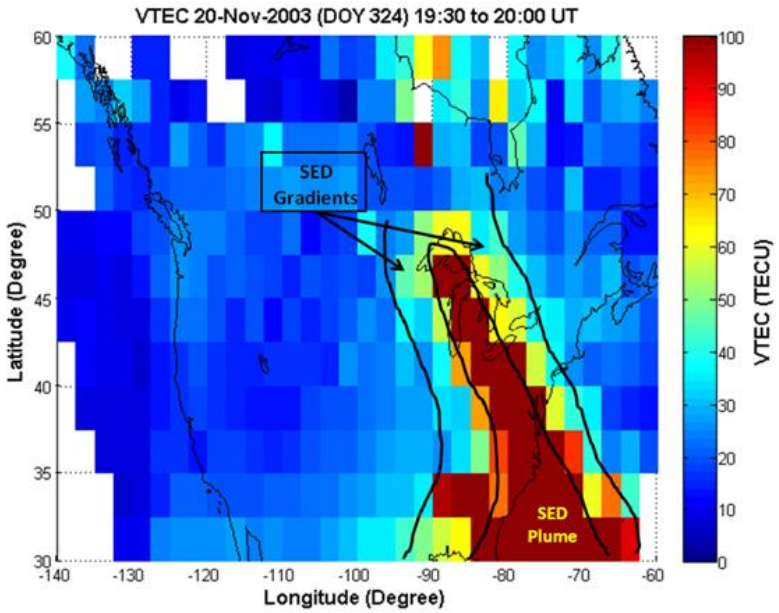

Figure 5.31: TEC map of SED on 20 November 2003 between 1930 and 2000 UT

Two different satellites observed from two different stations passed through the SED plume and its gradients: PRN 28 observed at ALGO station (Latitude: 45.9558^{o} and Longitude: -78.0714^{o}) and PRN 31 at AMC2 station (Latitude: 38.8031^{o} and Longitude:-104.2546^{o}). These satellite observations are selected for studying the TEC characteristics of the storm. The following two sections provide analysis of VTEC variations associated with the SED.

5.2.1 ALGO Station – PRN 28

The VTEC series for PRN 28 between 1900 and 2300 UT is shown in Figure 5.32. The beginning of SED effect is clearly observed at ~1915 UT where a large increase in TEC from ~30 TECU to ~100 TECU is observed. Maximum TEC values are observed at

approximately 2000 UT. One hour later, the VTEC along the satellite-receiver line-of-sight has decreased to ~45 TECU (i.e., 55 TECU difference observed in one hour).

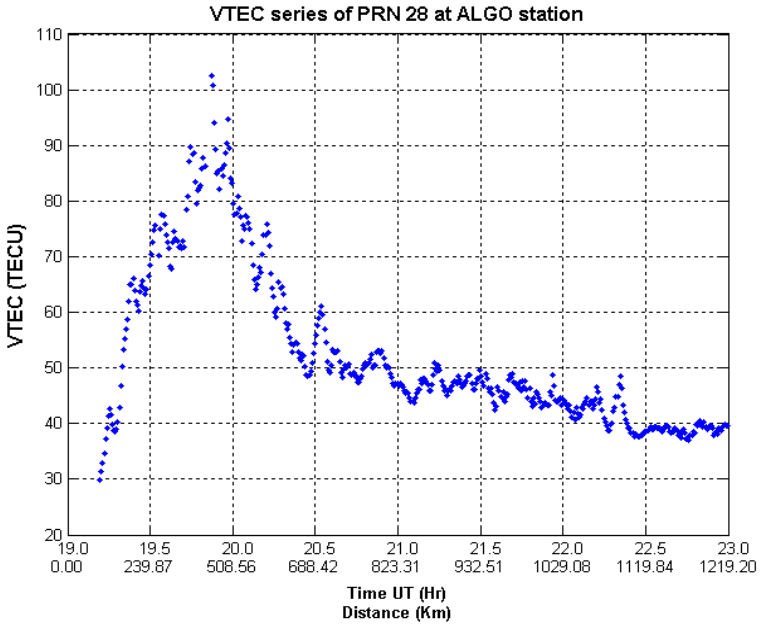

Figure 5.32: VTEC series of PRN 28 at ALGO station

A fourth-order Butterworth filter is implemented with cutoff frequency of 0.005 km^{-1} (wavelength 200 km) to study the HP and LP VTEC components will be used here as well to study the high variations of the VTEC series. The cutoff frequency was identified from the PSD in Figure 5.33.

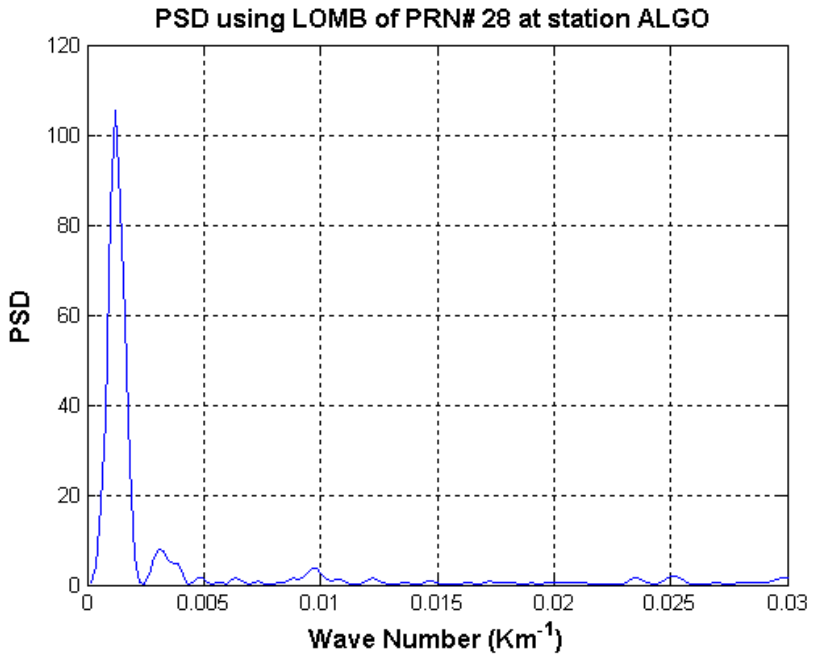

Figure 5.33: PSD of the VTEC series of PRN 28 at ALGO station

Two regions were chosen to study the SED effects. The first region includes gradients and the internal structure of the plume and the second region includes edge gradients.

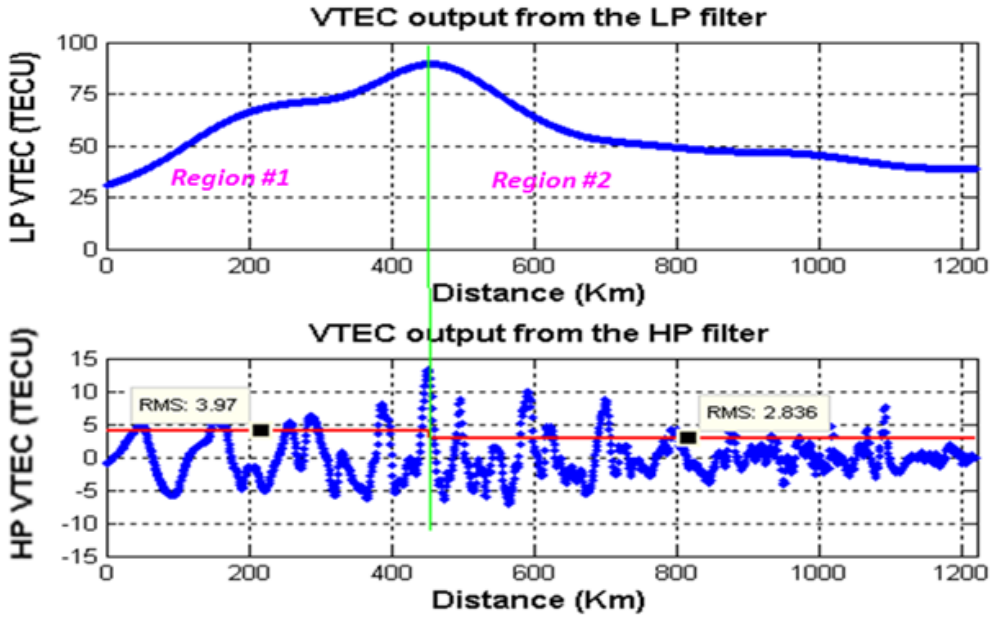

Figure 5.34: LP and HP components of PRN 28 VTEC series at ALGO station

The LP and HP VTEC components are shown in Figure 5.34. It is observed that the HP TEC series has large variations with amplitudes of 10 TECU close to the SED plume. The corresponding RMS values at the edges of the plume were 3.97 and 2.84 TECU respectively.

5.2.2 AMC2 Station – PRN 31

VTEC series for PRN 31 is shown in Figure 5.35. The gradients associated with the SED persist for two hours. TEC values increased from ~35 TECU at ~1845 UT to ~60 TECU two hours later. The VTEC series shows high VTEC fluctuations while the satellite-receiver line-of-sight moves through edge gradients and associated structures.

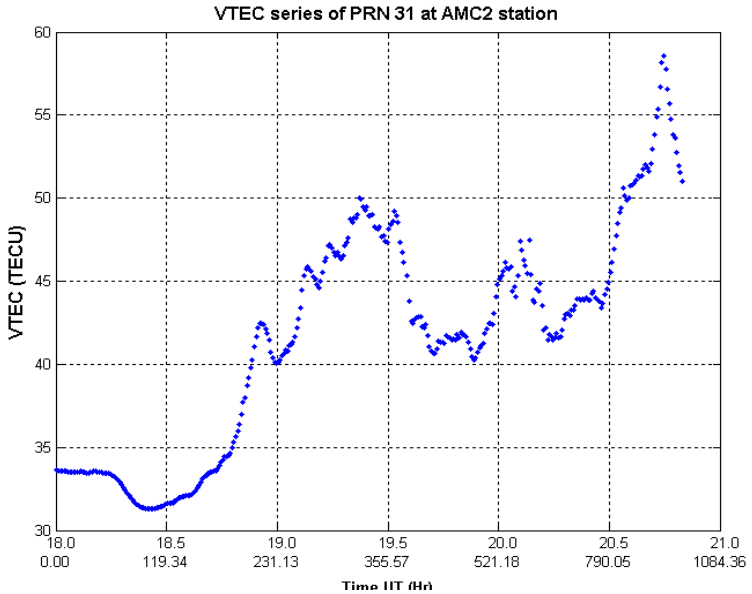

Figure 5.35: VTEC series of PRN 13 at AMC2 station

A fourth-order Butterworth filter is implemented with cut-off wave number 0.005 km^{-1} (wavelength 200 km) as chosen based on PSD shown in Figure 5.36.

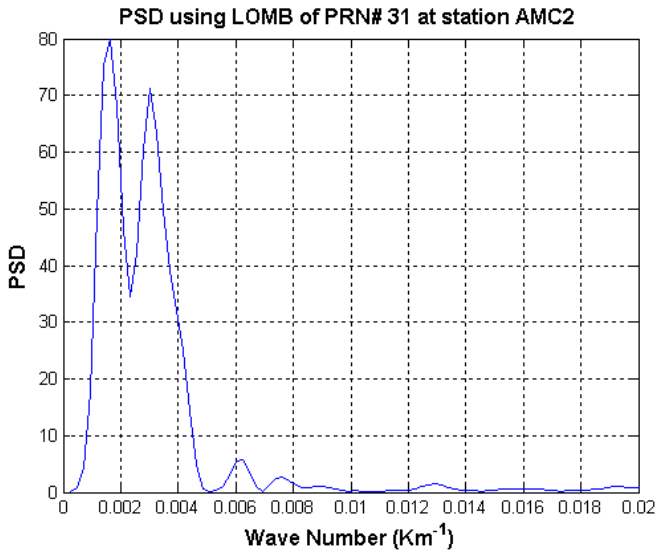

Figure 5.36: PSD of the VTEC series of PRN 31 at AMC2 station

The low and high frequency components obtained from the filter are shown in Figure 5.37. High frequency variations with 2.5 TECU amplitude are observed. The HP RMS value is 1.07 TECU. These high frequency variations are caused by structures within the large gradients of the SED plume.

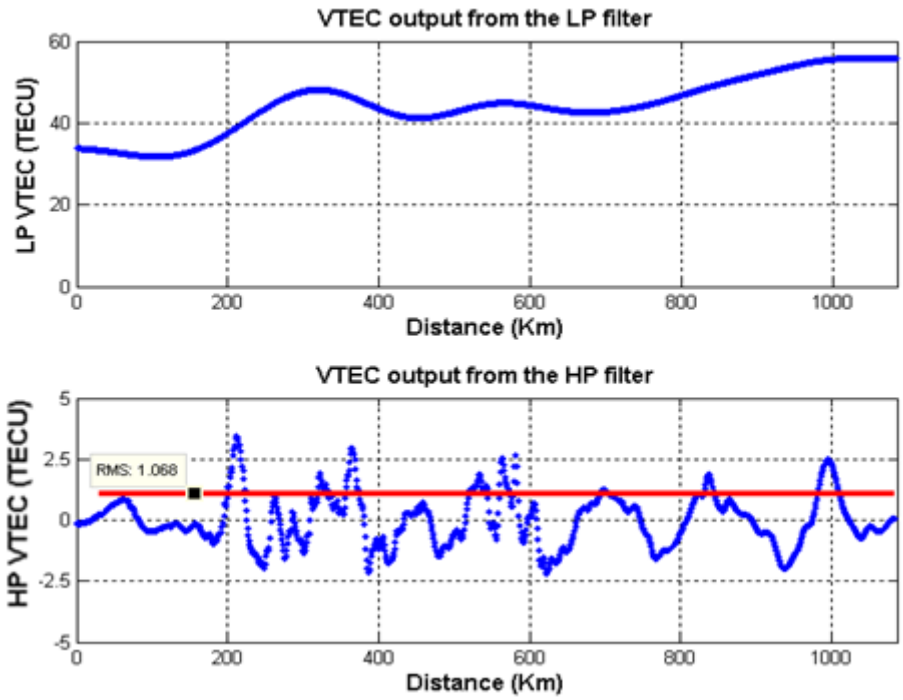

Figure 5.37: LP and HP components of PRN 13 VTEC series at AMC2 station

5.3 Analysis of Results

In order to simulate ionospheric activity at Canadian latitudes, three ionospheric SED events have been studied and temporal and spatial characteristics of TEC variations have been quantified. TEC maps were generated for North America to study temporal evolution of the SED features. Also, VTEC series were generated for individual satellite-

receiver lines-of-sight passing through the SED region. These analyses led to the following conclusions:

(1) During the SED event, large TEC values exceeding 100 TECU exist within the SED plume bounded by large TEC gradients surrounding the plume.

(2) The size of the SED plume varies with time and the severity of the SED. For the SED events on 29 and 30 October 2003, the maximum width of the SED plume base was 50 and 35 degrees respectively. For the SED event observed on 20 November 2003, the base of the plume had a maximum width of 30 degrees.

(3) The SED plume extends spatially from mid to low latitudes into westward and northward directions in the mid to high latitudes.

(4) The TEC values associated with SED periods change rapidly from low to high and from high to low values while the path between the satellite and the station pass through the edges of the plume towards or away from it. This region has high spatial TEC variations of amplitude of 0.2-0.7 TECU/km.

(5) Smaller wavelength structures exist in the SED plume and its edges. Structures with scale sizes 170-250 km have amplitudes of 10 TECU. For the three SED events, average RMS values of such variations were 2-4 TECU

5.4 Ionosphere Simulations

Based on the study of SED events capabilities are developed to simulate moderate and severe ionospheric activity over Canada. Such simulations are then used to evaluate WAAS performance under various levels of ionospheric activity. For this purpose, three

main ionospheric activity scenarios were simulated using MATLAB®. These simulations are based on the three SED events in this chapter. The MATLAB® tool was developed to control the severity and the location of these simulated ionospheric events, with the flexibility to challenge WAAS undersampling and ionospheric threat algorithms with worst-case scenarios.

The simulation is conducted as follows:

(1) The International Reference Ionosphere (IRI) model is used to generate nominal ionospheric activity over North America. The IRI model was developed by a joint working group of the International Union of Radio Science (URSI) and the Committee on Space Research (COSPAR) to produce an empirical standard model of the ionosphere, based on all available data sources for given location, time and data (Bilitza, 2011).

(2) After generating nominal conditions using the IRI model, severe ionospheric activity with realistic SED characteristics is generated superposed on the nominal ionospheric conditions to obtain a full map of the ionosphere using the MATLAB® tool.

(3) The MATLAB® tool is used to relocate, downscale, and upscale the ionospheric conditions in order to generate moderate or more severe ionospheric condition at different location based on the user's input.

The final output of this tool is a TEC map of the ionosphere over the user's defined area (as chosen with a range of the latitudes and longitudes). These TEC maps have resolution of $2^{o}\times2^{o}$ grid size to provide clear visualisation to the ionospheric conditions.

The following sections show three ionospheric conditions generated using the developed tool. These conditions are used to evaluate WAAS performance in Chapter 6. Two of these ionospheric events represent severe ionospheric activities similar to the SED events while the third one represents moderate ionospheric conditions generated by downscaling one of the simulated severe ionospheric events.

5.4.1 Severe Ionospheric Activity – Case 1

The first case is shown in Figure 5.38. This event represents severe ionospheric activity with plume and gradients similar to the SED features. This event is located over Canada between latitudes 40^{o} and 70^{o} and longitudes -80^{o} to -120^{o}.

For this case, a plume with base width of 40^{o} is generated at $\sim40^{o}$ latitude. This event is distributed spatially in northward and westward directions. Within the plume area, the TEC values generated are larger than 100 TECU (16 metres L1 range delay). Around the plume, gradients were generated to match the SED characteristics. These gradients have width of 6 to 10 degrees around the plume. The quiet area outside the plume and the gradients represents the nominal ionospheric conditions generated using the IRI model.

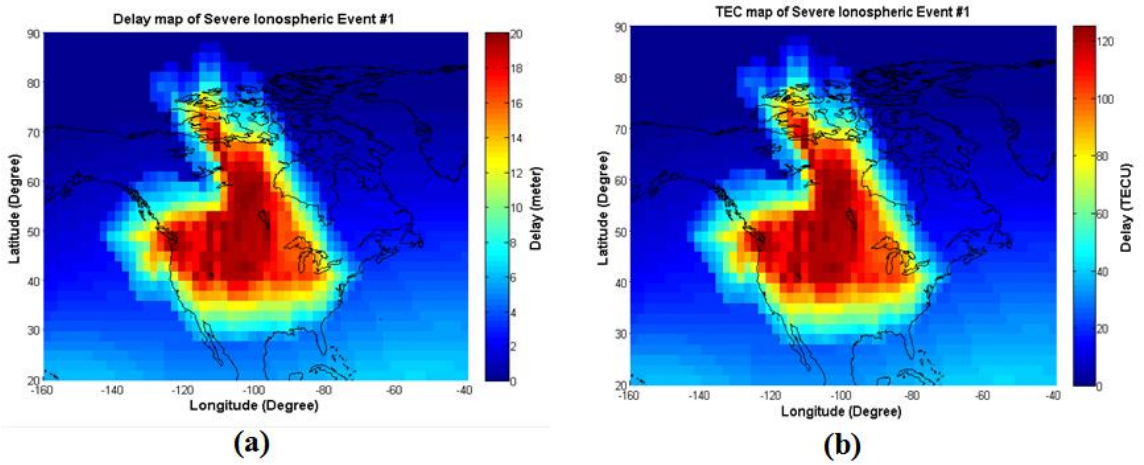

Figure 5.38: TEC map of simulated severe ionospheric activity in (a) metre scale and (b) TECU scale – Case 1

The SED feature for this case is located in the middle of Canada to create a challenging condition for WAAS over this region. WAAS has four Canadian WRSs with three located in the east. This event will challenge WAAS performance when Canadian stations minimally detect the severe ionospheric activity over the Canadian region.

5.4.2 Severe Ionospheric Activity – Case 2

The second case is shown in Figure 5.39. This is also a severe event similar to the SED. This event has the same characteristics of the SED observed on 29-30 October 2003 and generated using the MATLAB® tool as for the severe ionospheric activity in Case 1.

The centre of this event is located at lower latitudes to match the real SED event observed in October 2003. This SED has slightly extent than that for Case 1 and is distributed spatially in the north direction. The location of this event was chosen to affect the west side of North America and to cover the west coast of Canada. In this case the region of

SED is not covered by Canadian WRSs and limited observability is achieved with U.S, WRSs. The Canadian WRSs do not contribute in observing the presence of this activity. Moreover, the U.S. WRSs have limited observations contributing to WAAS detection algorithms. As a result, the WAAS expected performance could be degraded. These conditions make this event highly challenging for WAAS performance.

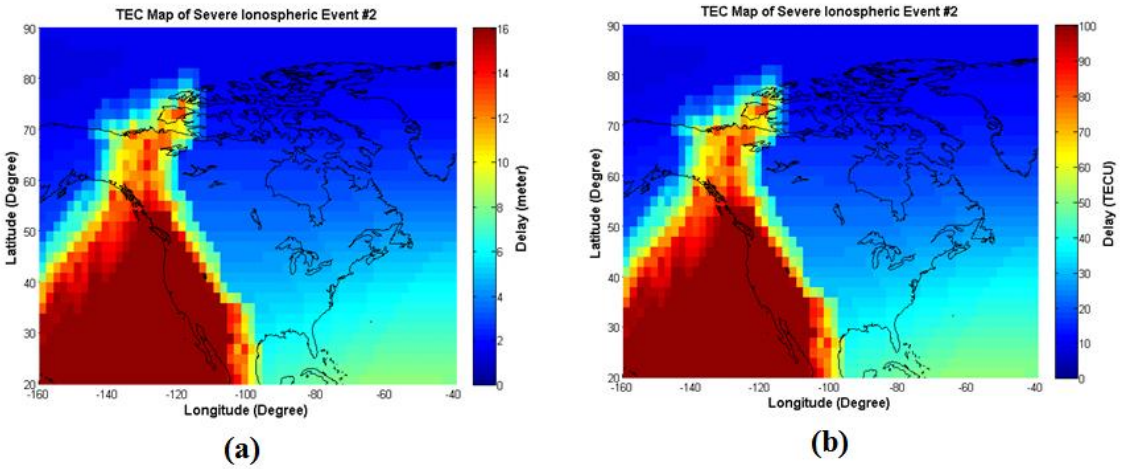

Figure 5.39: TEC map of simulated severe ionospheric activity in (a) metre scale and (b) TECU scale – Case 2

5.4.3 Moderate Ionospheric Activity

This moderate ionospheric activity has the same spatial characteristics of the severe ionospheric activity – Case 1 described in Section 5.4.1. For this case, the TEC values over the region of interest were downscaled using the developed MATLAB® tool to examine WAAS performance under moderately challenging ionospheric activities.

Figure 5.40 shows this moderate activity and its spatial distribution over Canada . While the spatial characteristics and the location of this event are the same as for Case 1, the

TEC values for the SED feature (i.e., inside the plume, the gradients, and the region outside the event) were downscaled by 60% of their original values. The maximum VTEC values inside the plume are slightly higher the 70 TECU (12 metres).

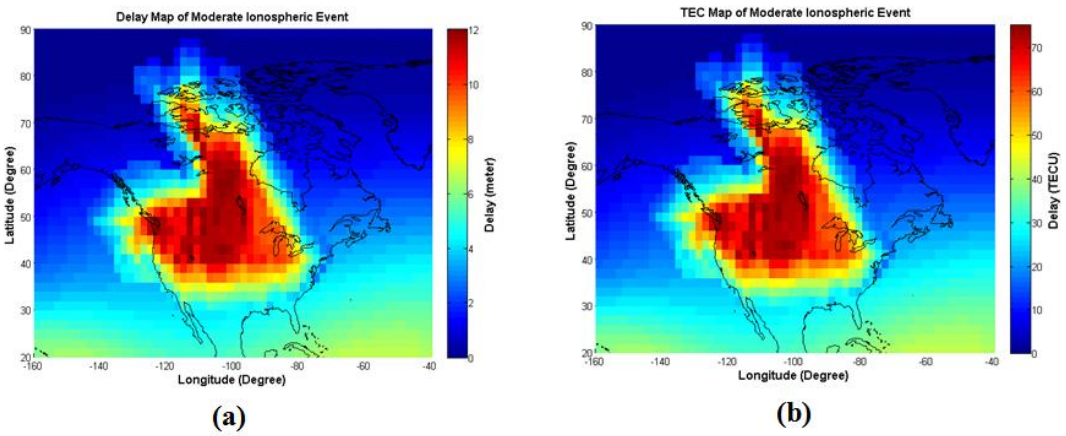

Figure 5.40: TEC map of simulated moderate ionospheric activity in (a) metre scale and (b) TECU scale

5.5 Chapter Summary

It has been discussed previously that WAAS availability and performance were degraded during SED periods of 29-30 October and 20 November 2003. In order to extend WAAS availability to Canadian latitudes, its performance under challenging ionospheric conditions similar to the SED events must be evaluated. For this purpose, this chapter provided a detailed study of the observed SED events in order to develop simulation of similar ionospheric challenges. A MATLAB® tool was specially developed to create and control these simulated scenarios. The last part of this chapter demonstrated the simulation tool for three ionospheric events (two severe and one moderate event) which will be used to evaluate WAAS performance. The next chapter will show and compare

the results obtained from WAAS planar fit and kriging algorithms for the simulated ionospheric scenarios in addition to a baseline case of nominal ionospheric conditions as generated from the IRI model.

Chapter Six: WAAS Performance Evaluation

In this chapter, various ionospheric conditions are simulated and WAAS performance is evaluated for both planar fit and Kriging ionospheric model techniques.

From each ionospheric scenario, ionospheric delay observations were simulated for all satellite-receiver lines-of-sight at 29 WRSs in Canada and the United States. GPS orbits are simulated for this purpose using the nominal 24-satellite GPS constellation. The simulated GPS observations were generated at five-minute intervals which is the regular update interval for WAAS estimates for nominal ionospheric conditions. In this chapter, only one update epoch is shown for the purpose of WAAS evaluation.

These ionospheric delay observations are provided as input to WAAS algorithms for both planar fit and Kriging model techniques in order to obtain the estimated delay, error bounds, and the VPL for each case.

In this chapter the three ionosphere simulations defined previously (Section 5.4) are implemented and WAAS performance evaluated. Accuracies of the WAAS generated ionospheric corrections are analysed in addition to magnitudes of error bounds and the VPL for each event. A comparison is conducted between the two model techniques (i.e., planar fit and Kriging).

6.1 Nominal Ionospheric Activity

Nominal ionospheric conditions are first assessed to provide a baseline reference. This ionospheric simulation and the IPP distribution for visible satellites from 29 WRSs are shown in Figure 6.1. The IPP distribution is for a five-minute interval. These data are used in the WAAS algorithms to generate ionospheric corrections at WAAS IGPs.

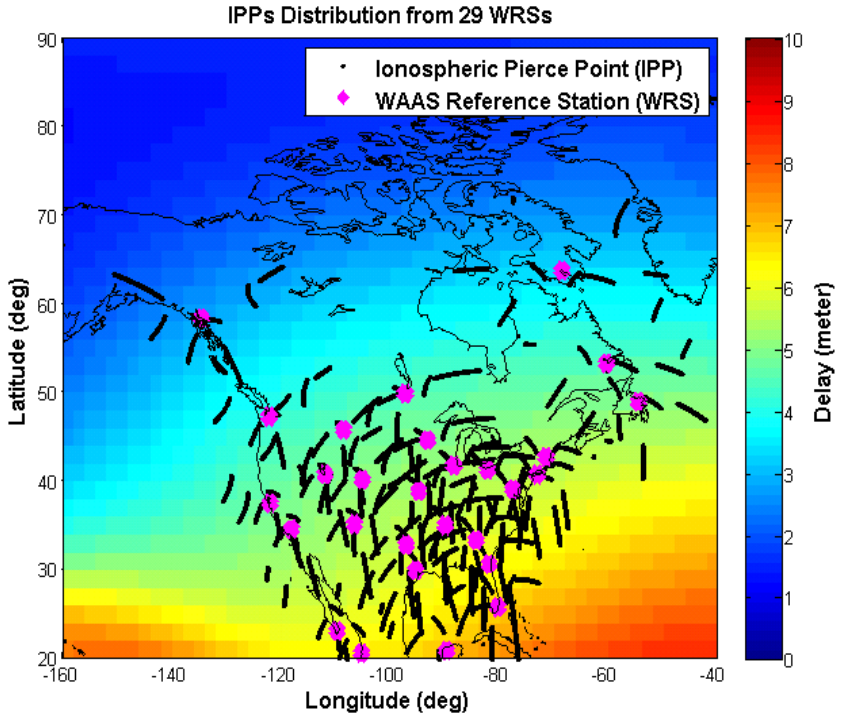

Figure 6.1: Delay map and IPP distribution of nominal ionospheric event

The ionospheric delay at each IGP over Canada is extracted from Figure 6.1and shown in Figure 6.2. Accuracies of the WAAS corrections will be assessed by comparing WAAS results at the IGPs to Figure 6.2 (truth).

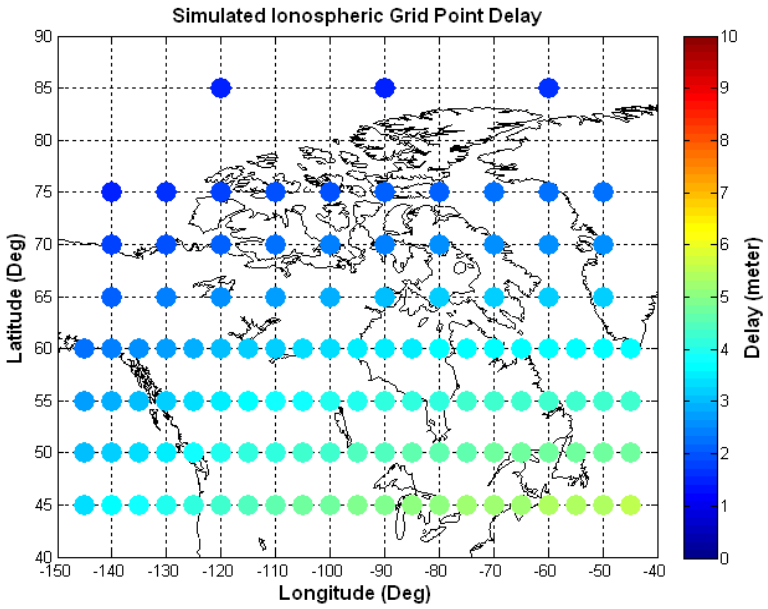

Figure 6.2: Simulated IGP delays of the nominal ionospheric activity

By processing the input observations (e.g. from Figure 6.1) using the WAAS model algorithms, the ionospheric corrections are estimated at IGPS using planar fit and kriging techniques at each IGP between latitudes 40^{o} and 90^{o}. The estimated delays from both techniques are shown in Figure 6.3 (a) and (b). At some of the IGPs represented in black, WAAS could not estimate the delay due to lack of the observations within the fit radius of each one of these IGPs. These IGPs are referred to as Not Monitored and the estimated delays are not available at these IGPs.

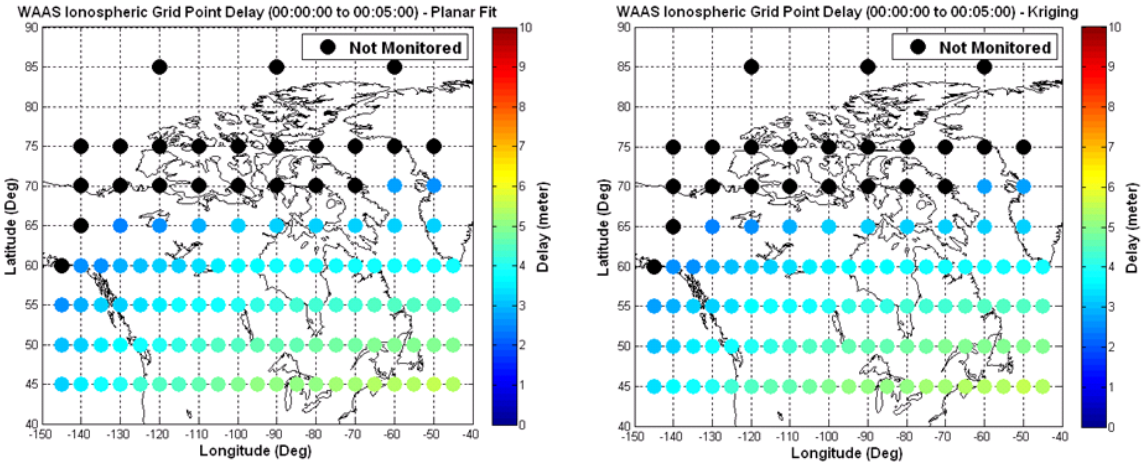

(a) **(b)**

Figure 6.3: WAAS estimated delays for nominal activity using (a) planar fit and (b) kriging techniques

To study the accuracy of the estimated delays, Figure 6.4(a) and (b) show the difference between the simulated (Figure 6.2) and the estimated delays using planar fit and kriging respectively. From the figure it is observed that the maximum error for the planar fit case is ~ 0.25 m at IGP Lat: 60^{o} and Lon: -100^{o} while the error is ~ 0.21 m for the kriging model observed at IGP Lat: 65^{o} and Lon: -100^{o}. It is also observed that there are some regions (e.g., along latitude 60^{o}) with high error values. These errors are due to the limited observability in this region (as can be noticed from Figure 6.3); this error in ionospheric delay estimation was slightly higher for the planar fit model versus kriging results.

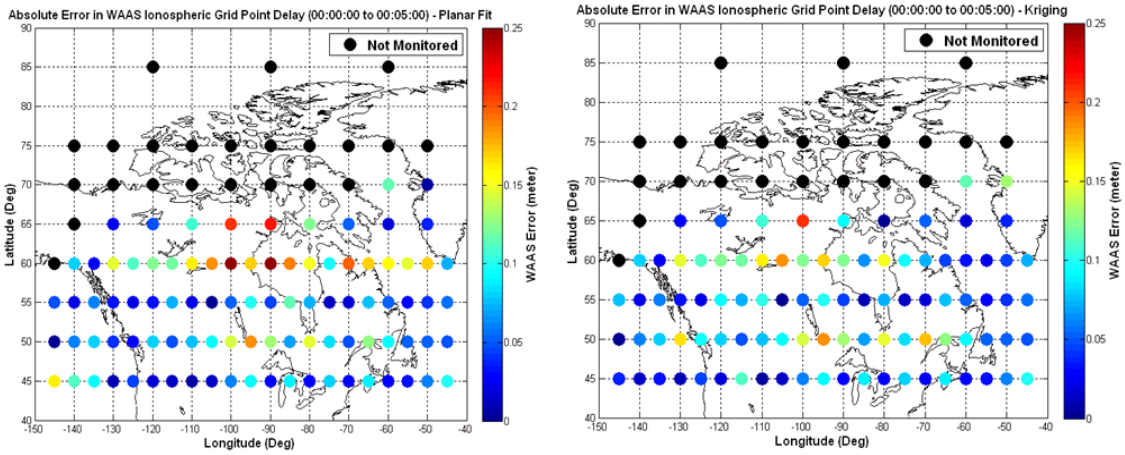

(a) **(b)**

Figure 6.4: Error in WAAS estimated delays for nominal activity using (a) planar fit and (b) kriging techniques

As mentioned previously, WAAS estimates error bounds (GIVEs) along with the estimated delays at each IGP. Figure 6.5 shows the GIVE values generated by WAAS for planar fit and kriging models. Studying this figure, one can note that in the undersampled regions, the GIVE values are more conservatives and set to higher values, 6 m and 15 m, corresponding to GIVEI of 12 and 13 respectively. In the well-sampled regions, the GIVE values are lower and below 4.5 m (GIVEI = 11). The IGPs set to Not Monitored were not used in error bound calculations and WAAS IGPs status is Not Monitored.

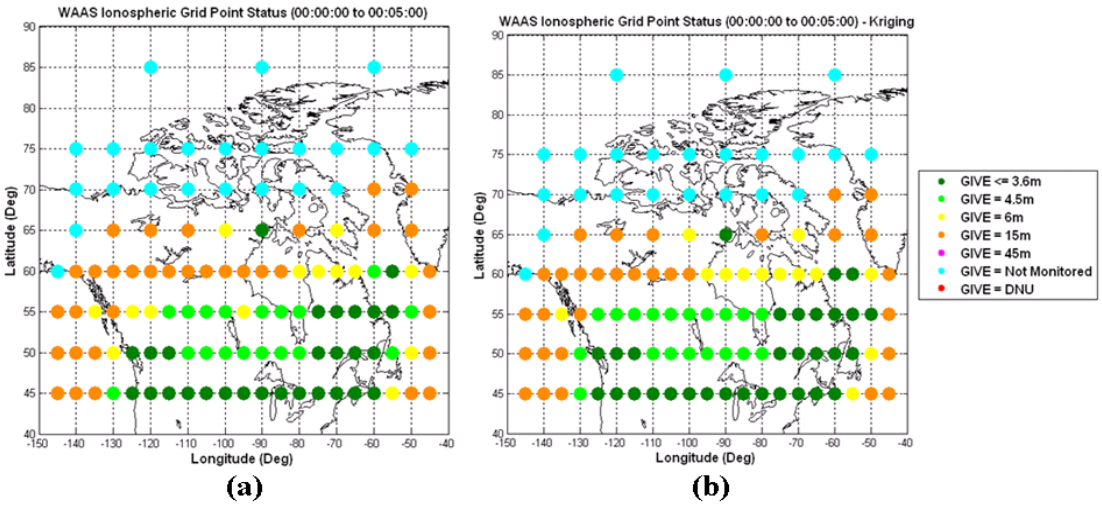

Figure 6.5: WAAS IGPs status for nominal conditions using (a) planar fit and (b) kriging techniques

To validate the results and ensure that the errors are bounded by WAAS, the difference between WAAS ionospheric delay errors (shown in Figure 6.4) and the GIVE produced by WAAS algorithms were calculated and are shown in Figure 6.6. From this figure, it is observed that the difference values (GIVE minus WAAS error) are positive at all the IGPs which mean that the GIVE values are higher than errors in the estimated delays. In other words, this means that the errors are bounded by WAAS GIVE values. Also it can be observed that larger differences exist between the GIVE and WAAS errors (~15 m) in the undersampled regions; this indicates conservative GIVE estimates.

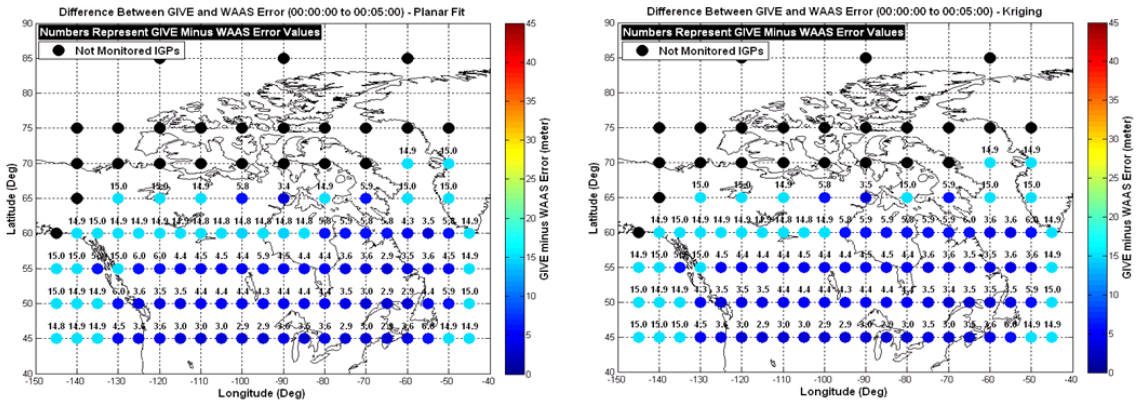

Figure 6.6: Difference between GIVE and WAAS error for nominal ionospheric conditions for (a) planar fit and (b) kriging techniques

Finally, to ensure WAAS operation and availability over the Canadian latitudes, vertical protection levels (VPL) are evaluated (see APPENDIX A) and plotted in Figure 6.7. The parameters used to calculate the protection level are as follows: earth's radius of 6378.1363 Km, ionospheric shell height of 350 Km, K_v of 5.33, $\sigma_{UDRE} = 0.91$, $\delta UDRE = 1$, Old But Active Data (OBAD) of 0, and the Root Sum Square (RSS) flag of 1. The resulting VPL values from the WAAS planar fit and kriging ionosphere model techniques are below the vertical alert limit (50 m) which means WAAS service is accepted over the Canadian latitudes. Since the VPL values obtained from the WAAS algorithm over the Canadian region are less than the VAL, it can be stated that WAAS service will be available for these nominal ionospheric conditions. In this nominal case, minimum VPL values tend to be around 25 m which can be seen in VPL plots. The higher VPL values (i.e., the red area in Figure 6.7) are around 50 m where using WAAS could be critical within this area. These high VPL values occurred due to limited observability and high GIVE values over this area.

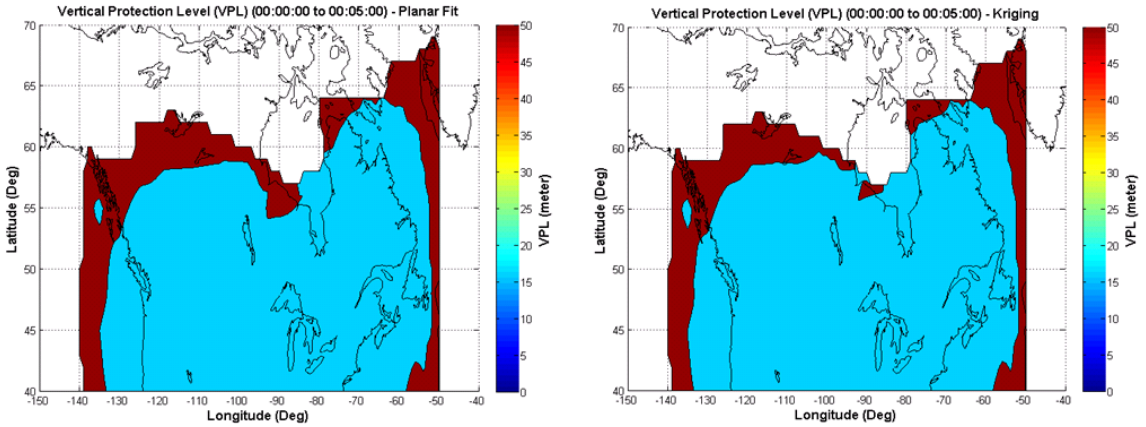

Figure 6.7: VPL for nominal ionospheric activity for (a) planar fit and (b) kriging techniques

6.2 Moderate Ionospheric Activity

In this section, the simulated moderate ionospheric storm obtained from the simulation tool is to used test WAAS performance under such conditions. Figure 6.8 shows the TEC maps of this event and the IPP distribution from the 29 WRSs in Canada and the United States.

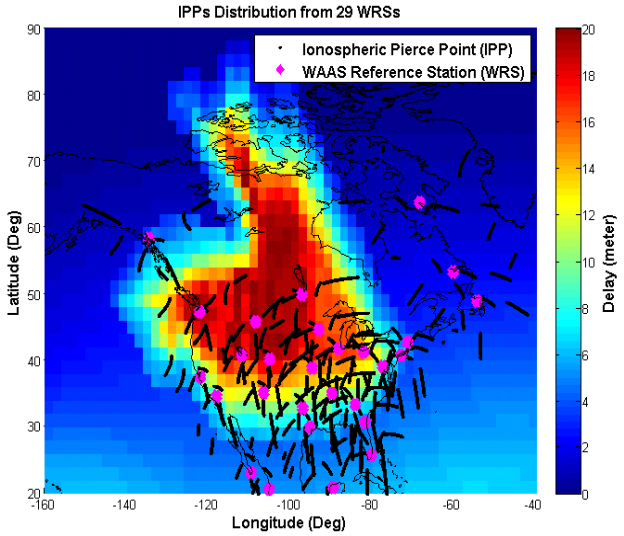

Figure 6.8: Delay map and IPP distribution for moderate ionospheric event

The simulated vertical ionospheric delay values at each IGP corresponding to this ionospheric event are extracted from the TEC map (Figure 6.8) and shown in Figure 6.9. This figure is considered "truth" for direct comparison with WAAS output ionospheric corrections at the IGPs.

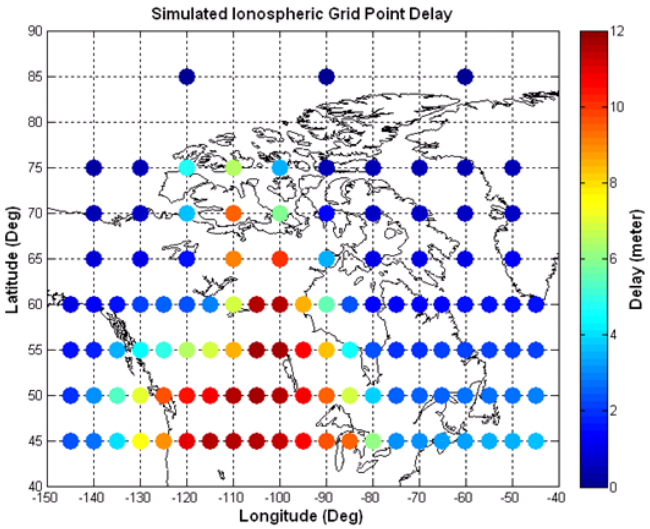

Figure 6.9: Simulated IGP delays for the moderate ionospheric activity

Ionospheric delays values at all the IPPs are used in the WAAS algorithm to estimate ionospheric corrections at the IGPs. WAAS planar fit and kriging correction estimates are shown in Figure 6.10. IGPs in black color represent the Not Monitored values where no observations were available to estimate the delay values at these IGPs. A slight difference between the estimated delays from each technique can be observed (e.g., IGPs along Latitude 55^{o}).

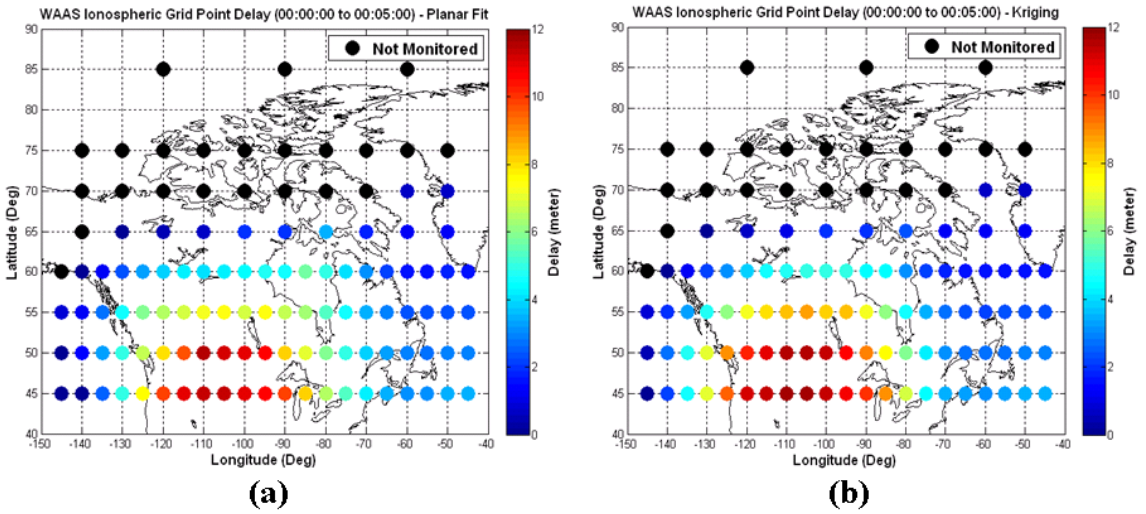

Figure 6.10: WAAS estimated delays for moderate activity using (a) planar fit and (b) kriging techniques

Differences between the simulated (truth) and the estimated delays at each IGP were calculated and are plotted in Figure 6.11 to determine accuracy for both model techniques. In general, the kriging method shows slightly better estimation accuracy than the planar fit. Most of the absolute differences between the simulated and the estimated delays were below 2 m except within the undersampled region affected by event (Lat: 55^{o} to 65^{o} and Lon: -90^{o} to -110^{o}) where the accuracy was clearly degraded and errors reached 9 m. However, the accuracy in planar fit estimate is slightly lower than for the kriging technique.

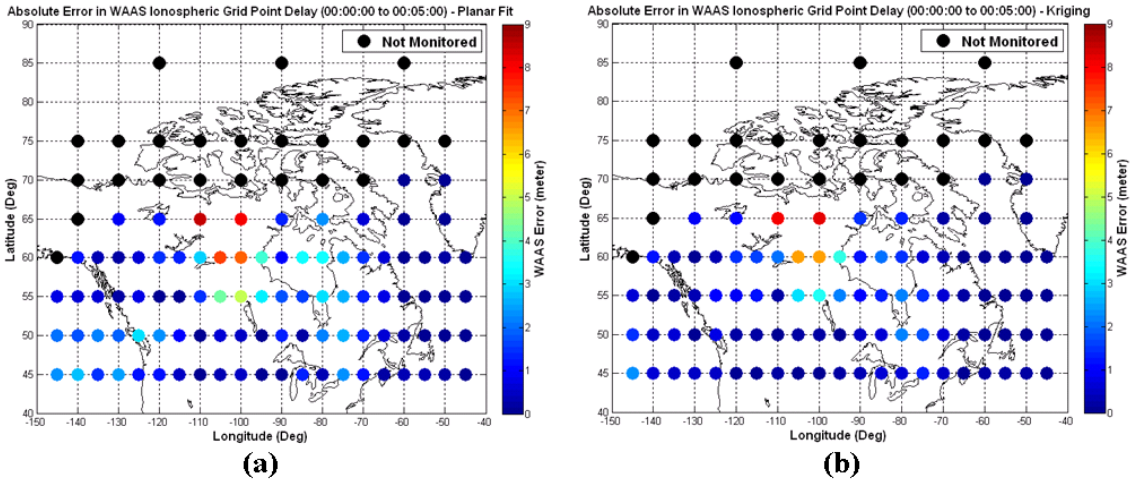

Figure 6.11: Error in WAAS estimated delays for moderate activity using (a) planar fit and (b) kriging techniques

GIVE values associated with delay estimates are also tested to ensure that these errors are bounded. Therefore, GIVEs are plotted in Figure 6.12.

Within the well sampled region of the simulated storm, WAAS set the GIVE values to less than 6 m (GIVEI below 12). On the other hand, WAAS set the error bounds to higher values reaching 15 m and 45 m (GIVEI = 13 and 14) within the undersampled regions (west and east coasts of Canada). Also, it can be observed that some IGPs that are within the well-sampled region are set to Not Monitored (GIVEI = 15). These IGPs are affected by the simulated SED event and the IGPs within this area tripped the irregularity detector (irregularity test); therefore, WAAS responded to this threat by setting the IGP to Not Monitored. Moreover WAAS was less conservative for the kriging model: some IGPs with GIVE of 45 m obtained from the planar fit were set to lower values using the kriging technique.

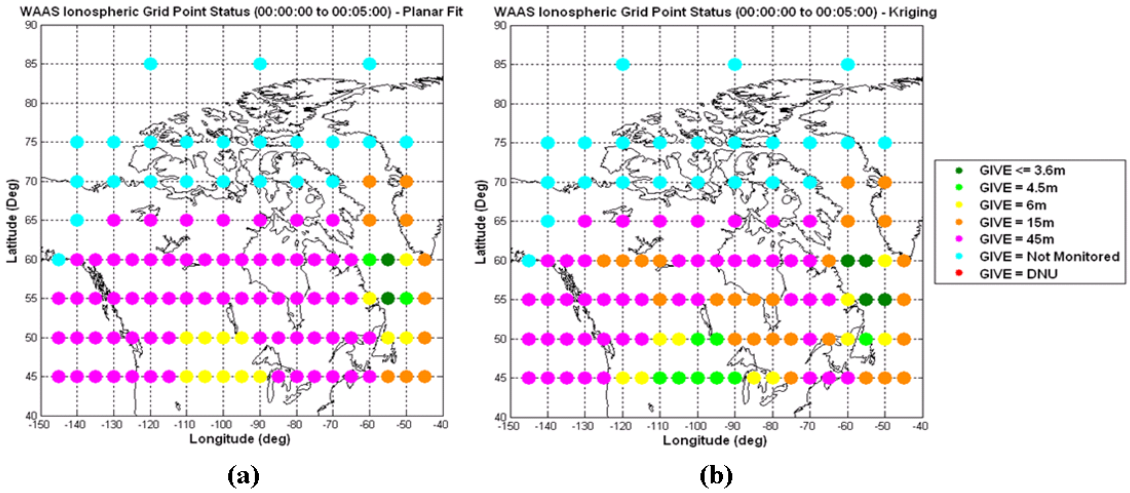

Figure 6.12: WAAS IGPs status for moderate activity using (a) planar fit and (b) kriging techniques

To ensure that WAAS errors are bounded by the GIVE values, differences between WAAS errors and the GIVE values at each IGP are plotted in Figure 6.13. From this figure it is noted that all the differences are positive which means WAAS GIVE values bounded the errors. For some IGPs, such as those in the south-west and north-east regions, differences are high since the errors are low but WAAS set GIVE values to their maximum values (i.e., 45 m).

For this case, it can be concluded that kriging estimation technique provides better performance than the planar fit technique since WAAS was less conservative in generating the error bounds for kriging particularly in the limited observability regions; this can be noted from the GIVE values in the area within Longitudes: -130^{o} to -90^{o} and Latitudes: 45^{o} to 65^{o}. Moreover, the kriging technique gives slightly better accuracy in delay (correction) estimation than the planar fit for this case.

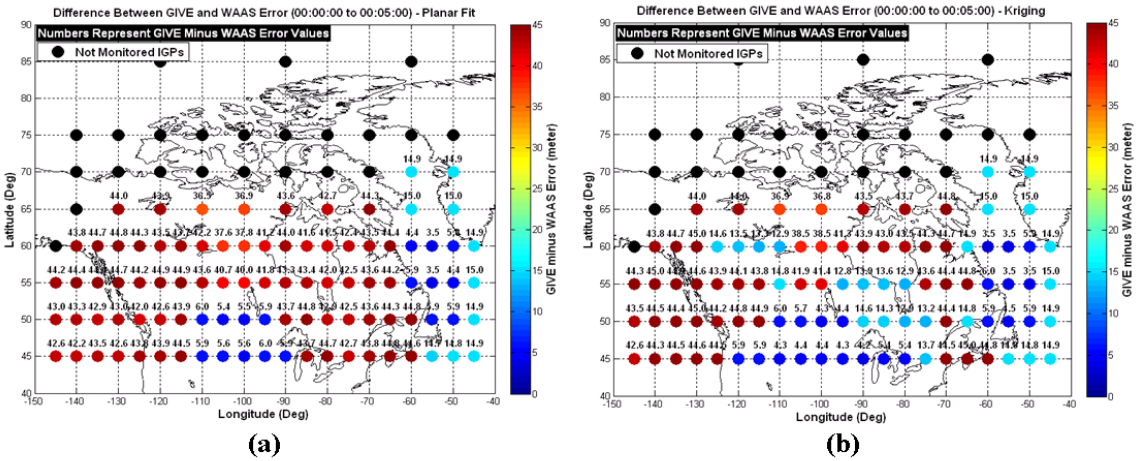

Figure 6.13: Difference between GIVE and WAAS error for moderate ionospheric activity for (a) planar fit and (b) kriging techniques

Finally, the VPL is evaluated for this event from planar fit and kriging results. The WAAS availability region with VPL values is shown in Figure 6.14. WAAS VPL values exceed the VAL in most of the available region. Using the planar fit model, WAAS service is only available within a small region over Canada (Lat: ~40^o to ~50^o, Lon: ~ -90^o to ~ -105^o); this region is slightly larger for the kriging technique. The high VPL values result from the high GIVE values generated by WAAS in addition to the degraded geometry due to using only 24 satellites in the analysis instead of the full constellation. Also it can be observed that a high structure appears in the VPL plot in Figure 6.14 which can be attributed to using only 24 GPS satellites in the analysis; this affects the geometry especially when there are only 4 or 5 visible satellites at the user's location.

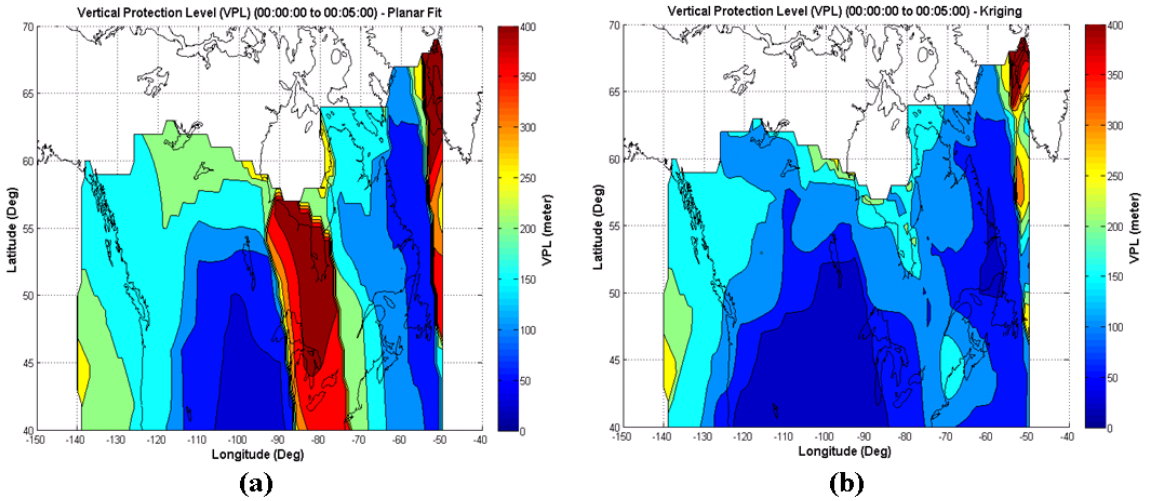

Figure 6.14: VPL for moderate ionospheric activity for (a) planar fit and (b) kriging techniques

6.3 Severe Ionospheric Activity – Case 1

In this scenario highly challenging ionospheric activity is simulated with characteristics of the SED events studied in Chapter 5. This severe simulated activity has similar spatial characteristics to the moderate event in the previous section but with higher ionospheric delay values. The TEC map and the simulated delays at the IGPs are shown in Figure 6.15 and Figure 6.16 respectively.

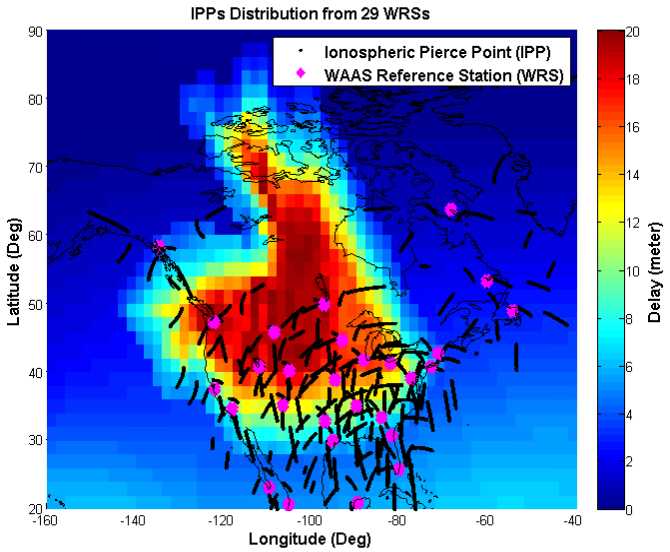

Figure 6.15: Delay map and IPP distribution for severe ionospheric event (Case 1)

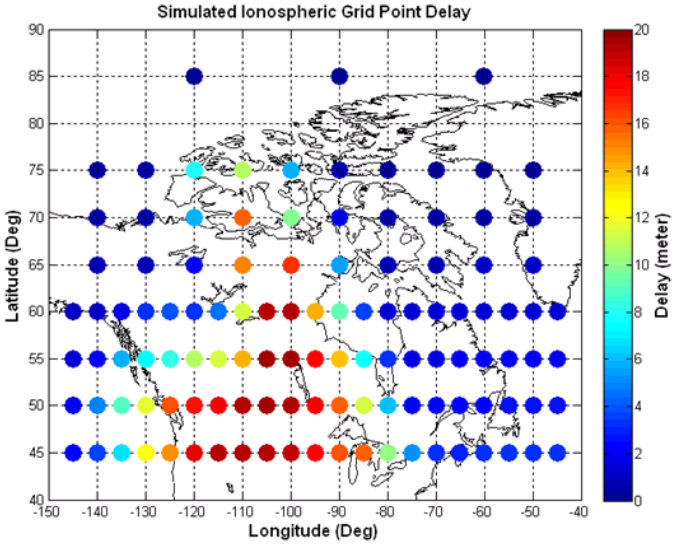

Figure 6.16: Simulated delay values at the IGPs for the severe ionospheric activity (Case 1)

Observations obtained from the 29 WRSs were provided to the WAAS algorithm with both planar fit and kriging techniques tested to estimate ionospheric delays as shown in Figure 6.17. It is observed that some IGPs are set to Not Monitored due to lack of observations in the given region.

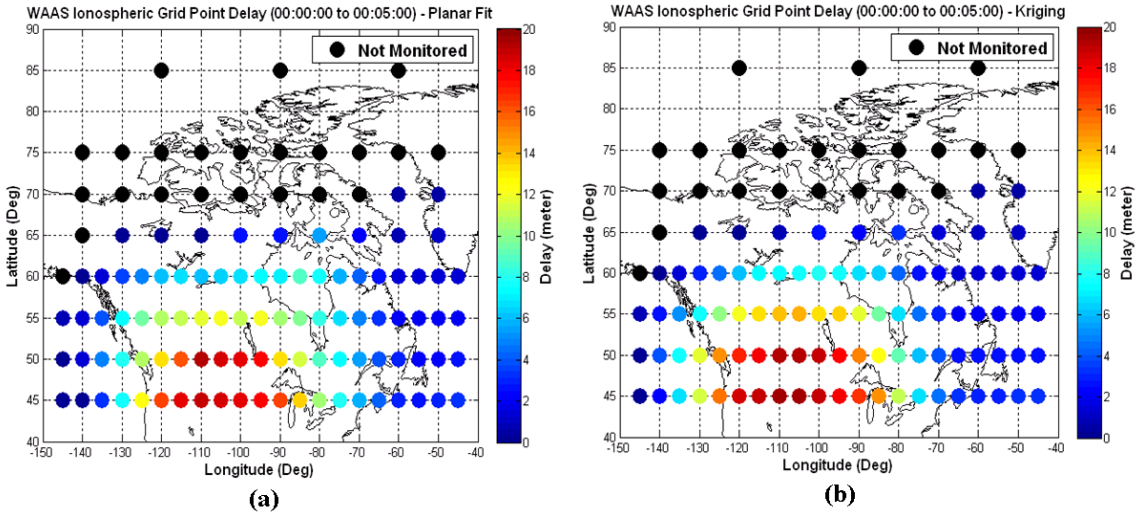

Figure 6.17: WAAS estimated delays for severe activity – Case 1 using (a) planar fit and (b) kriging technique

Similar to the moderate event, differences between simulated (truth) and WAAS estimated delays were generated to assess accuracy of the WAAS estimates. Figure 6.18 shows a spatial plot of this accuracy analysis. It is observed that within regions of limited observability (such as the region around latitudes 55^o to 65^o and longitudes -90^o to -110^o) the errors are large and reach ~ 15 m. Also, near the west coast, errors in planar fit estimated delays reached 5 m at some IGPS and were higher than for the kriging model. Similar to the previous two scenarios, kriging produces better performance in the respect that WAAS errors for the kriging model are equal or lower than planar fit errors.

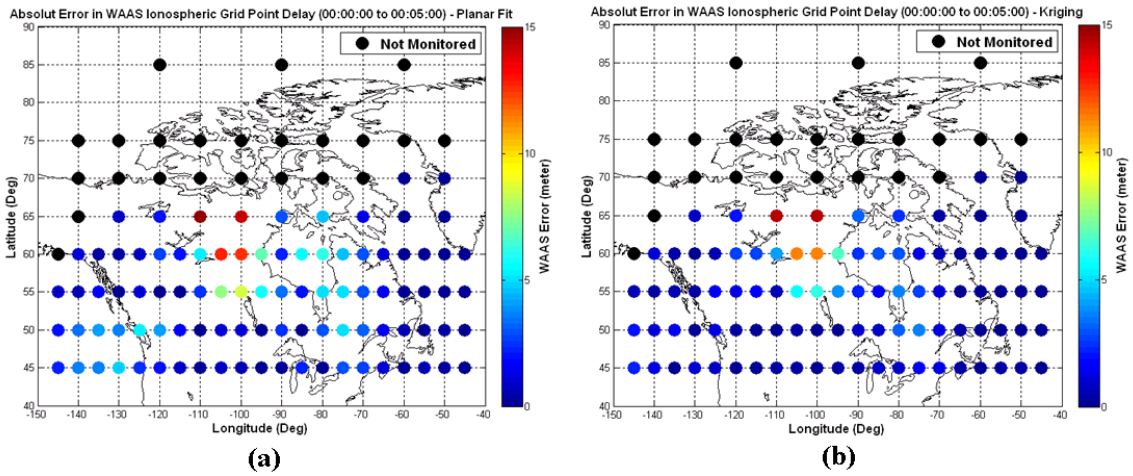

Figure 6.18: Error in WAAS estimated delays for severe activity - Case 1 using (a) planar fit and (b) kriging techniques

GIVE values for this case are shown in Figure 6.19 for both estimation techniques. For the planar fit technique, it is observed (Figure 6.19 (a)) that the irregularity detector is tripped most of the time . Almost all IGPs are set to the higher values of 45 m (GIVE index 14) for both planar fit and kriging except for some well-sampled regions were WAAS error bounds are 4.5, 6 and 15 m (GIVE index 11, 12, and 13 respectively). For the kriging techniqe (Figure 6.19 (b)) service availability was much better and there were less IGPs tripping the irregularity detector with lower GIVE values compared to the planar fit model; the kriging error bounds within this area (Lat: 40^{o} to 50^{o} and Lon: -110^{o} to -90^{o}) are set to 6 and 15 m (GIVE indices 12 and 13 respectively).

This degradation in WAAS performance is due to the severity of the event and the limited observability. The undersampling threat has an impact on WAAS performance where the error bounds are set to high values.

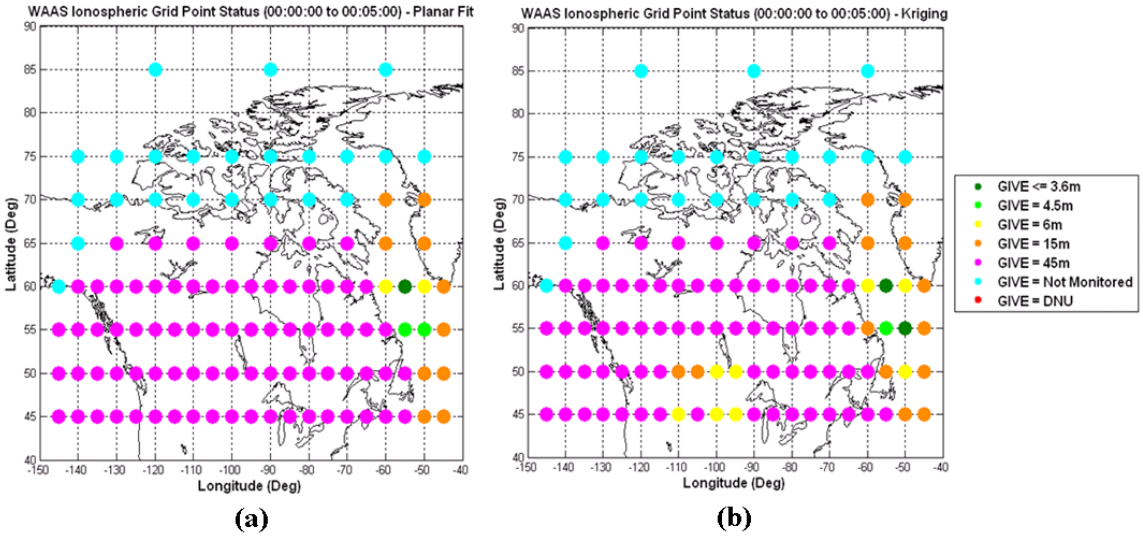

Figure 6.19: WAAS IGPs status of severe activity - Case 1 using (a) planar fit and (b) kriging techniques

To make sure that WAAS GIVEs bounded WAAS errors reliably for this case, differences between the GIVE values and estimated WAAS delay errors are generated and shown in Figure 6.20. As all the difference values are positive, it can be stated that integrity is maintained. However, in some regions where the ionosphere is highly active and the observability is limited, the GIVE values were set to maximum values which results in a large overbounding of the error itself.

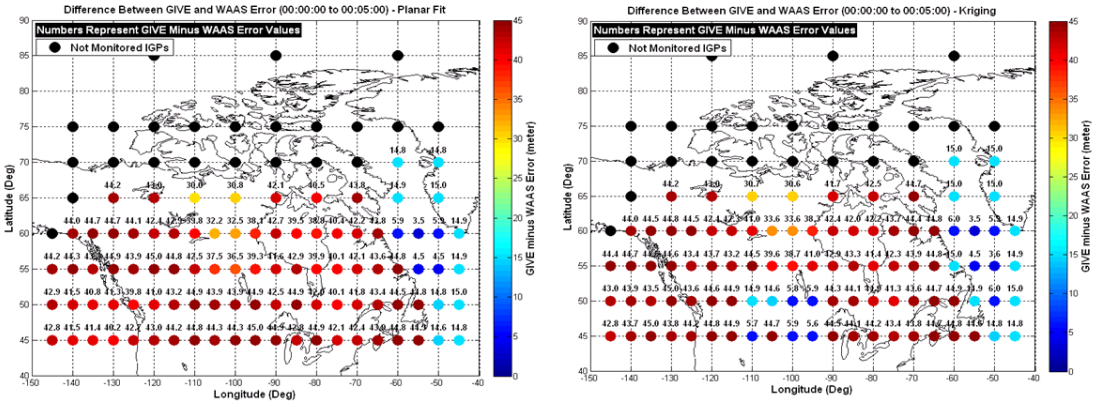

Figure 6.20: Difference between GIVE and WAAS error for severe ionospheric activity – Case 1 for (a) planar fit and (b) kriging techniques

WAAS availability was studied for this case as well, and the VPL values were calculated aa shown in Figure 6.21. For the planar fit technique, it is found that service was not available over the Canadian region except for a small area at the east coast where the GIVE values are low; this area is not affected by the simulated ionospheric storm. For the kriging technique, performance did not show any big difference; however, WAAS service is available between latitudes 40^o to 50^o and longitudes -100^o to -90^o near the east coast area. Outside the mentioned areas, WAAS is not available (service denied) since the VPL values exceed the VAL (50 m). VPL structures also appear in this case due to the degredation in satellite geometry resulting from using only 24 GPS satellites (as discussed in the previous section for the moderate case).

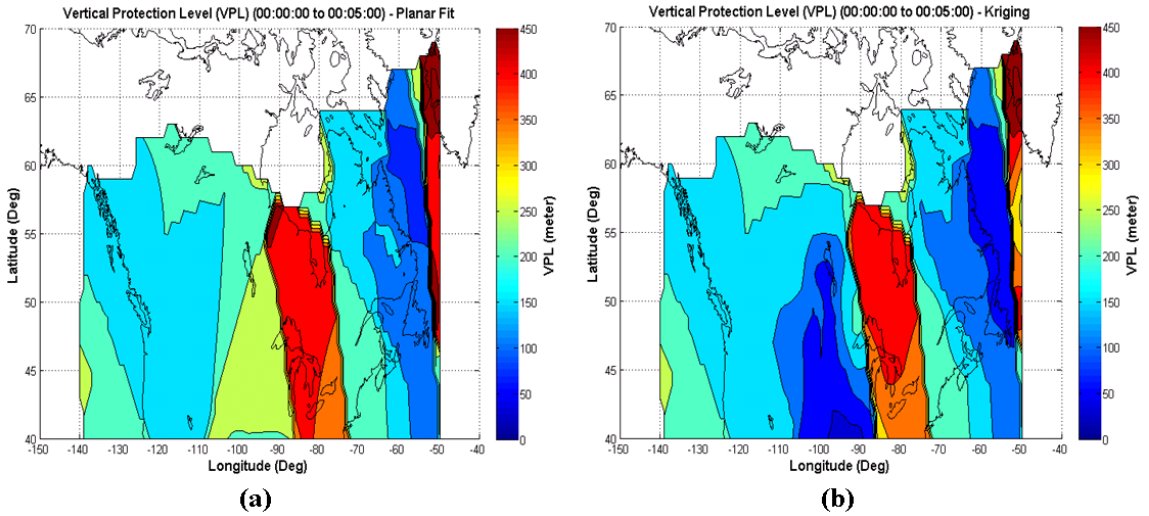

Figure 6.21: VPL for severe ionospheric activity - Case 1 for (a) planar fit and (b) kriging techniques

6.4 Severe Ionospheric Activity – Case 2

This highly challenging ionospheric activity is shown in Figure 6.22. Since the west coast suffers from limited observability, this event is located over the west coast to evaluate WAAS under worst case conditions.

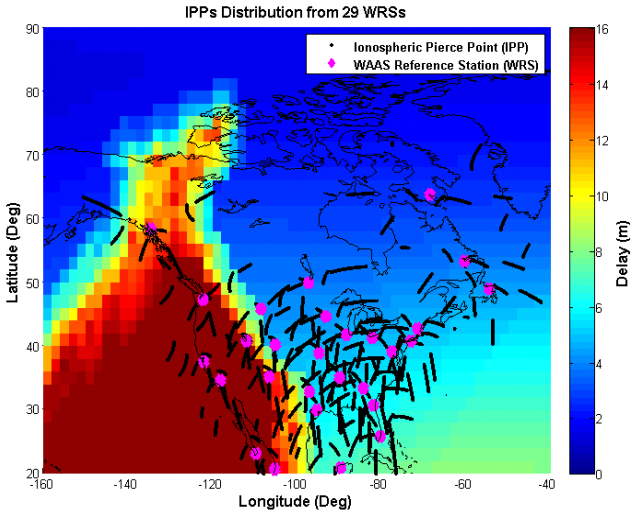

Figure 6.22: Delay map and IPP distribution for severe ionospheric activity - Case 2

This event has lower delay values than the previous severe condition where maximum ionospheric delay values are set to 16 m. The simulated delays at the IGPs over North America are shown in Figure 6.23.

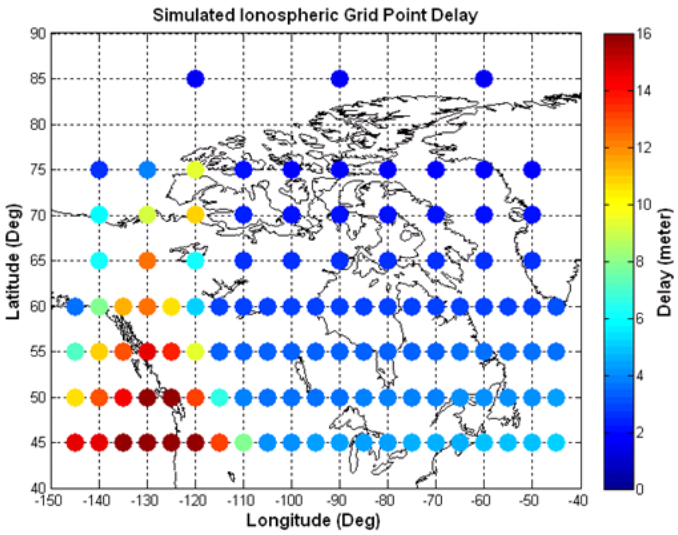

Figure 6.23: Simulated delay values at the IGPs for the severe ionospheric activity – Case 2

Analysis similar to that conducted for the three previous simulations is repeated for this event. Therefore, the ionospheric delays are simulated for the IPPs along each available satellite-receiver line-of-sight and used as input for the WAAS algorithm to estimate the ionospheric delays at the IGPs using planar fit and kriging techniques. These estimated delays are shown in Figure 6.24.

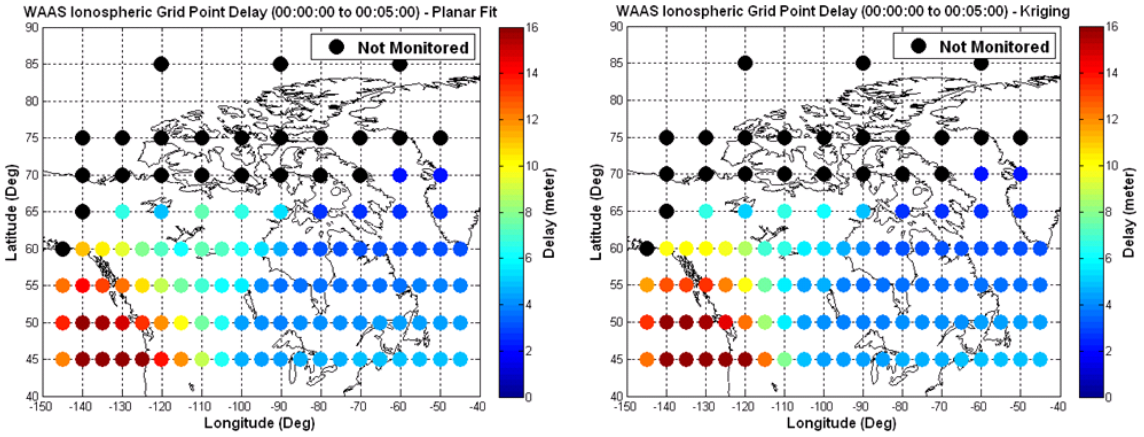

Figure 6.24: WAAS estimated delays for severe activity – Case 2 using (a) planar fit and (b) kriging techniques

To evaluate accuracy of WAAS estimated ionospheric delays, differences between simulated (truth) and the WAAs estimated delays are calculated and plotted in Figure 6.25.

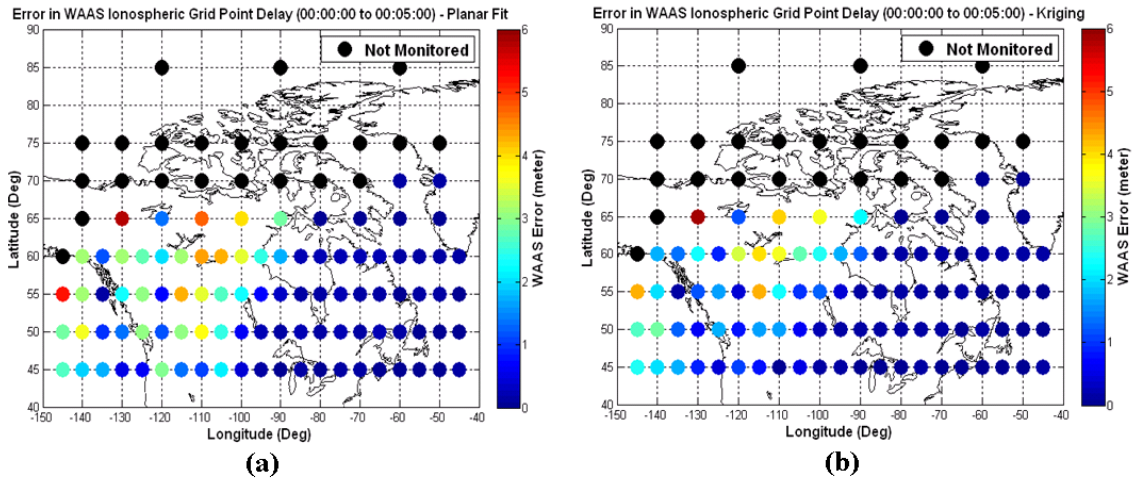

Figure 6.25: Error in WAAS estimated delays for severe activity – Case 2 using (a) planar fit and (b) kriging techniques

The effect of large ionospheric gradients in estimating ionospheric delays is clearly shown in the figure. The region of high gradients is observed between longitudes -100^{o} and -120^{o} at most Canadian latitudes. For both estimation techniques, WAAS errors vary

between 3 m and 6 m within this region. It is also observed that the kriging technique provides more accurate estimation within the well-sampled region; in the regions of low observability, the planar fit and kriging results are almost the same with slightly lower errors for the kriging estimates.

GIVE values are shown in Figure 6.26. It is observed that within the area of this event the irregularity detector has been tripped for both ionosphere model techniques and the corresponding IGPs are set to 45 m (GIVE index 14). Over the east coast, most of the IGPs are set to values less than 15 m (GIVE index below 13).

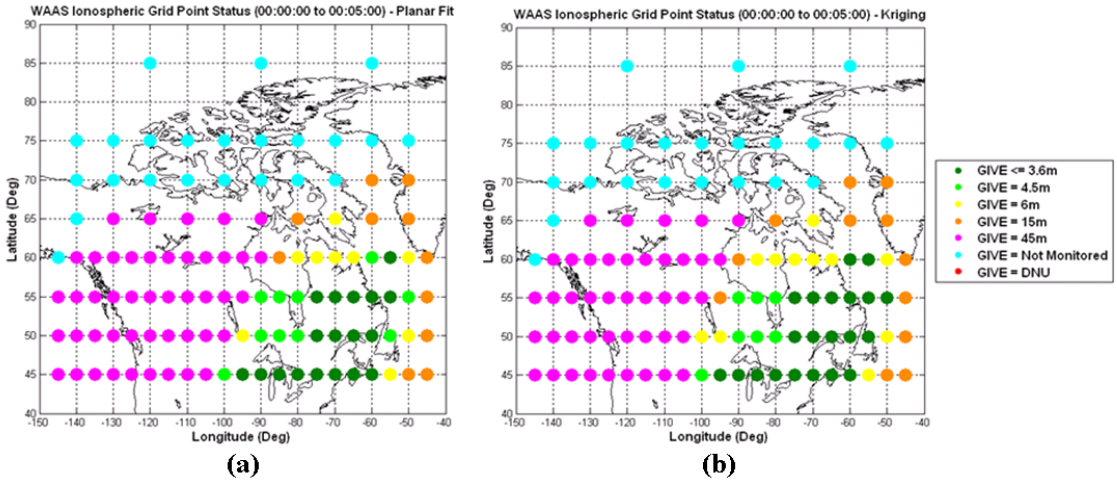

Figure 6.26: WAAS IGPs status for severe activity – Case 2 using (a) planar fit and (b) kriging techniques

To ensure that the error bounds are accurately bounding WAAS errors for this event, differences between WAAS errors and the GIVE values are calculated. For the monitored IGPs, these differences are always positive which means WAAS errors are bounded reliably. These values are plotted in Figure 6.27. Within regions affected by the SED,

WAAS is more conservative and set the error bounds to higher values with differences exceeding 40 metres.

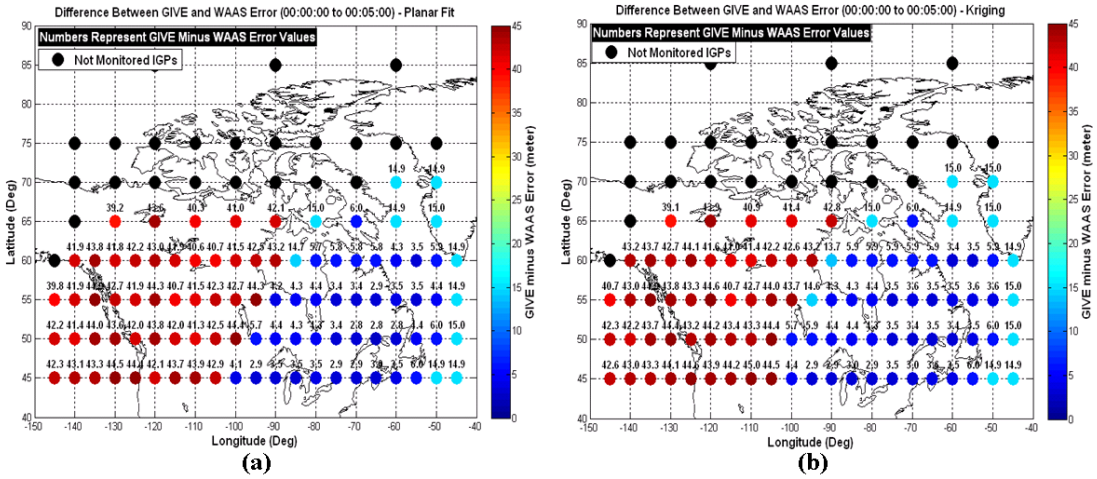

Figure 6.27: Difference between GIVE and WAAS error for severe ionospheric activity - Case 2 for (a) planar fit and (b) kriging techniques

WAAS performance is also assessed through availability and the VPL for this case. VPL was calculated for each ionosphere model technique and plotted in Figure 6.28. WAAS is not available in the regions affected by the SED plume and gradients for both the planar fit and kriging techniques. In this region the VPL values exceed the VAL (50 metre). On the other hand, WAAS is available in the eastern region between latitudes of 40^{o} and 65^{o} for both estimation techniques. A small region at high latitudes (approximately between latitudes 60^{o} to 65^{o} and near longitude -50^{o}) has high VPL values due to the limited observability. The structure in VPL values within the available area is due to using a low number of GPS satellites (24 GPS satellites) which results in poor geometry affecting the observation matrix used in VPL calculation.

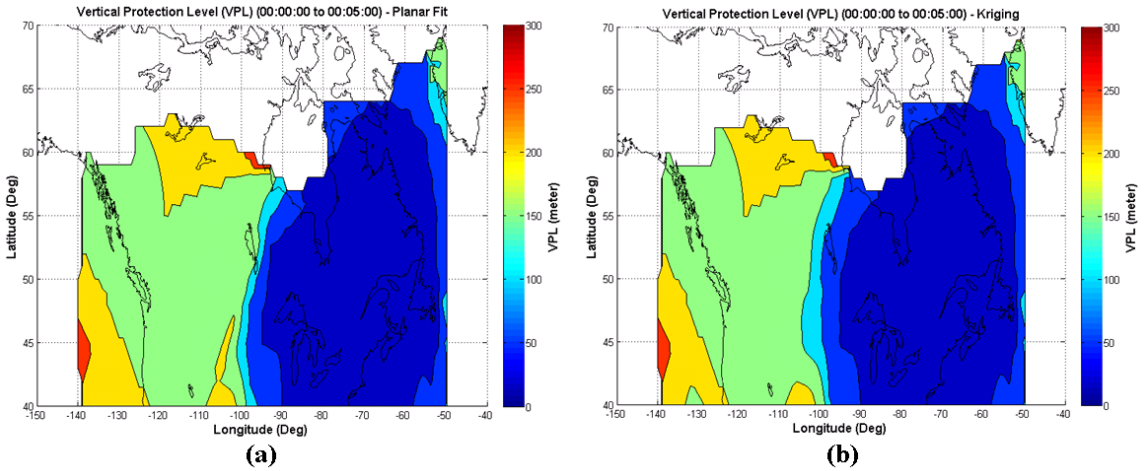

Figure 6.28: VPL for severe ionospheric activity – Case 2 for (a) planar fit and (b) kriging techniques

6.5 Summary and Results Analysis

As presented earlier in Chapter 4 and this chapter, planar fit and kriging techniques are used by WAAS to estimate the ionospheric delays at IGPs. Using these two different techniques in a WAAS performance analysis, several findings are noted:

1- The kriging technique results in slightly lower WAAS errors compared to the planar fit technique for the three ionospheric scenarios tested here. Table 6-1 summarizes the WAAS errors for both planar fit and kriging techniques.

2- Under severe ionospheric activity, the kriging model produces larger areas of available WAAS service than the planar fit model. This can be observed by comparing the VPL figures produced from both models.

3- In all cases the WAAS errors are bounded reliably and integrity is maintained under the most challenging ionospheric conditions.

Table 6-1: Maximum WAAS error difference in planar fit and kriging models

	Maximum WAAS Error (Planar Fit)	Maximum WAAS Error (Kriging)
Nominal Ionospheric Scenario	0.25 m	0.21 m
Moderate Ionospheric Scenario	8.5 m	8.2 m
Severe Ionospheric Scenario – Case 1	15 m	14.3 m
Severe Ionospheric Scenario – Case 2	5.8 m	5.9 m

Chapter Seven: Conclusions and Recommendations

This chapter summarizes the findings of this work and identifies recommendations with respect to the work objectives. The main objective of this work is to evaluate the impact of highly challenging ionospheric effects on WAAS performance over the Canadian region. This is necessary for future certification and implementation of CWAAS for aviation in Canada. A major motivation for this study is the fact that WAAS experienced a considerable degradation of availability during SED events observed in October – November 2003. Therefore, it is critical to validate Canadian WAAS operation under similar severe ionospheric conditions. This is best achieved through simulation. In addition, since there is a limited number of WRSs across Canada, there is minimal observation coverage within the Canadian region and existing reference stations are not adequate to detect ionospheric disturbances; substantial reductions in WAAS performance can occur and should be quantified.

7.1 Conclusions

This study has shown that the presence of severe ionospheric conditions will significantly degrade WAAS performance. Over the areas where ionospheric irregularities exist and/or suffer from the undersampling threat, WAAS algorithms are capable of estimating the ionospheric delays but the errors in these ionospheric corrections are high. WAAS GIVE values bound all such errors over the WAAS coverage area and these bounds are

conservative and set generally to very high values. At high latitudes, WAAS cannot estimate the ionospheric delays and "Not Monitored" flags are assigned to the IGPs in this region due to low observability.

In this study, only 29 WRSs out of 38 existing WRSs are used to evaluate WAAS performance. These WRSs located at latitudes above 20^{o} to provide realistic observability across the Canadian region. The rest of the WRSs were not used since observations from these stations do not contribute to WAAS estimations and predictions over Canada. Even in trying to achieve the best observability from the 29 WRSs, some features in the simulated severe ionospheric conditions could not be captured and WAAS errors were relatively high. Moreover, the ionospheric delays in western Canada were not estimated due to minimal observation conditions.

The GIVE values generated by WAAS are very conservative in order to bound the large errors at IGPs within regions of undersampling and large irregularities. Although WAAS generates estimates of the ionospheric delays, the GIVE values within regions of enhanced ionospheric activity are set to maximum (GIVE = 45 m) since the irregularity detector exceeded the predefined statistical threshold.

Four simulated ionospheric conditions varying in the severity and location of ionospheric irregularities are used to evaluate the current WAAS planar fit and the future WAAS Kriging models. In all scenarios, the Kriging model outperformed the planar fit. WAAS errors for Kriging approach were lower than those for the planar fit and Kriging was observed to be much more effective in detecting the presence of ionospheric

irregularities. Therefore, future WAAS service using the Kriging model will result in larger areas of service availability for Canadian users.

This work also shows the VPL values for each ionospheric scenario to determine if WAAS service is available to users. For the nominal ionospheric conditions, WAAS service is fully available over Canada. On the other hand, for the scenarios that simulate enhanced ionosphere (i.e., moderate, severe – Case 1, and severe – Case 2), the VPL values within the undersampled regions of high ionospheric delays and irregularities were inflated due to high GIVE values. These VPL values exceeded the predefined alert limit (set to 50 metres) which means that WAAS service will be denied for the users over these affected regions.

It is important to mention that the results obtained here were based on the minimum GPS constellation requirements by choosing only 24 GPS satellite. Therefore, using all the existing GPS satellites in the constellation will lead to better observability and better performance. The nominal worst case conditions were tested here.

This study has resulted in conclusions about WAAS performance and availability in Canada during enhanced ionosphere periods. The major contributions of this study are summarized as follows:

- Characteristics of previously observed SED events have been determined and quantified.

- Different realistic ionospheric conditions were simulated and tools developed to assess degraded WAAS performance.
- WAAS performance was investigated and evaluated over the Canada latitudes during nominal and enhanced ionospheric conditions for the current planar fit model and the future kriging model.

7.2 Recommendations

A major problem for the Canadian WAAS implementation is limited observability due to having only four reference stations in Canada. Severe ionospheric conditions cannot be observed and features such as SED cannot be resolved adequately. This is a concern for the approaching solar maximum 2013-2014. The sparse network and severe ionospheric conditions lead to substantial degradation in WAAS performance. As the behaviour of the ionosphere is not predictable, it is concluded that in the presence of similar conditions to those simulated here, WAAS service could be denied. One factor that could be modified is the sparse network. Adding more reference stations particularly in western Canada will improve observability which in turn improves WAAS performance and increases the area over which WAAS service is available.

References

Basu, S., Basu, Su., MacKenzie, E., Bridgwood, C., Valladares, C.E., Groves, K.M. and Carrano, C. (2010) "Specification of the occurrence of equatorial ionospheric scintillations during the main phase of large magnetic storms within solar cycle 23", *Radio Science*, vol. 45.

Béniguel, Y., Adam, J., Bourdillon, A. and Lassudrie-Duchesne, P. (2011) "Ionosphere scintillation effects on navigation systems", *C. R. Physique*, vol. 12, no. 2, March, pp. 186-191.

Bilitza, D. (2011) "*The International Reference Ionosphere (IRI)"*, [Online], Available: http://iri.gsfc.nasa.gov/ [22 June 2011].

Black, H.D. (1978) "An Easily Implemented Algorithm for the Tropospheric Range Correction", *J. Geophys. Res.*, vol. 83, no. B4, pp. 1852-1828.

Blanch, J. (2002) "An Ionosphere Estimation Algorithm for WAAS Based on Kriiging", Proceedings of ION GPS 2002, Portland, Oregon.

Blanch, J. (2002) "An Ionosphere Estimation Algorithm for WAAS Based on Kriging", *Proceedings of 15th International Technical Meeting of the Satellite Division of the US Inst. of Navigation, Portland, Oregon*, p. 816.

Blanch, J. and Walter, T. (2004) "Ionospheric EstimationUsing Extended Kriging for a Low Latitude SBAS", Proceedings of the Institute of Navigation GNSS 2004, Long Beach, CA.

Blanch, J., Walter, T. and Enge, P. (2003) "Adapting Kriging to the WAAS MOPS ionospheric grid", *ION's National Technical Meeting*, January, p. 848–853.

Blanch, J., Walter, T. and Enge, P. (2004) "Ionospheric Estimation Using Extended Kriging for a Low Latitude SBAS", *ION GNSS 17th International TechnicalMeeting of the Satellite Division*, September, p. 387–391.

Borre, K., Akos, D.M., Bertelsen, N., Rinder, P. and Jensen, S.H. (2007) *"A Software-Defined GPS and Galileo Receiver: A Single-Frequency Approach"*, 1st edition, Birkhäuser Boston.

Brunner, F.K. and Gu, M. (1991) "An improved model for the dual frequency ionospheric correction of GPS observations", *Manuscripta Geodaetica*, vol. 16, pp. 205-214.

Coster, A.J., Colerico, M.J., Foster, J.C., Rideout, W. and Rich, F. (2007) "Longitude sector comparisons of storm enhanced density", *Geophys. Res. Lett.*, vol. 34.
Coster, A., Foster, J. and Erickson, P. (2003) 'Monitoring the Ionosphere with GPS', *GPS World*, May, pp. 42-49.

Coster, A. and Skone, S. (2009) "Monitoring storm-enhanced density using IGS reference station data", *Journal of Geodesy*, vol. 83, no. 3-4, March, pp. 345-351.

Datta-Barua, S., Walter, T., Konno, H., Blanch, J., Enge, P. and Komjathy, A. (2005) "Verification Of Low Latitude Ionosphere Effects on WAAS During October 2003 Geomagnetic Storm", Proceedings of ION 2005, Cambridge, MA.

Davies, K. (1990) "*Ionospheric Radio*", London: Peter Peregrinus Ltd.

Dmitriev, A. and Yeh, H.C. (2008) "Storm-time ionization enhancements at the topside low-latitude", *Ann. Geophys.*, vol. 26, pp. 867-876.

Doherty, P., Coster, A.J. and Murtagh, W. (2004) "Space weather effects of October-November 2003", *GPS Solutions*, vol. 8, pp. 267-271.

El-Arini, B.M., Poor, W.A., Lejeune, R., Conker, R., Fernow, J. and Markin, K. (2001) "An introduction to Wide Area Augmentation System and its predicted performance", *Radio Science*, vol. 36, no. 5, p. 1233–1240.

El-Rabbany, A. (2002) *"Introduction to GPS: The Global Positioning System"*, 2nd edition, Artech House.

FAA (2007) "Federal Aviation Administration", *Satellite Navigation News*, vol. 32, November.

FAA (2011) *"Federal Aviation Administration (FAA)"*, [Online], Available: http://www.faa.gov.

Foster, J.C. (1993) "Storm Time Plasma Transport at Middle and High Latitudes", *J. Geophys. Res.*, vol. 98, no. A2, pp. 1675-1689.

Foster, J.C. and Bruke, W.J. (2002) "SAPS: A new characterization for sub-auroral electric fields", *EOS Trans AGU*, vol. 83, pp. 393-394.

Foster, J.C. and Rideout, W. (2007) "Storm enhanced density: magnetic conjugacy effects", *Ann. Geophys.*, vol. 25, no. 8, pp. 1791-1799.

Gleason, S. and Gebre-Egziabher, D. (2009) *GNSS Applications and Methods*, Artech House.

Goad, C. and Goodman, L. (1974) "A Modified Hopfield Tropospheric Refraction Correction Model", Presented at the Fall Annual Meeting American Geophysical Union, San Francisco, California.

Gonzalez, W.D., Joselyn, J.A., Kamide, Y., Kroehl, H.W., Rostoker, G., Tsurutani, B.T. and Vasyliunas, V.M. (1994) "What is a geomagnetic storm?", *J. Geophys. Res.*, vol. 99, no. A4, p. 5771–5792.

GPS WAAS PS (2008) *"Global Positioning System, Wide Area Augmentation system (WAAS) Performance Standard"*, 1st edition.

Grewal, M.S., Weill, L.R. and Andrews, A.P. (2007) *"Global Positioning Systems, Inertial Navigation, and Integration"*, 2nd edition, Wiley-Interscience.

Hargreaves, J.K. (1992) *"The Solar-Terrestrial Environment: An Introduction to Geospace - the Science of the Terrestrial Upper Atmosphere, Ionosphere, and Magnetosphere"*, New York: Cambridge University Press.

Hopfield, H.S. (1969) "Two-Quartic Tropospheric Refractivity Profile for Correcting Satellite", *Jornal of Geophysical Research*, vol. 74, no. 18, pp. 4487-4499.

Humphreys, T.E., Psiaki, M.L. and Kintner, P.M..J. (2010) "Modeling the Effects of Ionospheric Scintillation on GPS Carrier Phase Tracking", *IEEE Transactions on Aerospace and Electronic Systems*, vol. 46, no. 4, October, pp. 1624-1637.

IS-GPS-200 (2010) *"Interface Specification, IS-GPS-200", Revision E*.

Jan, J. (2003) *"Aircraft Landing Using a Modernized Global Positioning System and the Wide Area Augmentation System"*, Ph.D. Dissertation, Stanford University, Dept. of Aeronautics and Astronautics.

Kaplan, E.D. and Hegarty, C.J. (2006) *"Understanding GPS: principles and applications"*, 2nd edition, Artech House.

Klobuchar, J.A. (1987) "Ionospheric Time-Delay Algorithm for Single-Frequency GPS Users", *IEEE Transactions on Aerospace and Eectronic Systems*, vol. AES-23, no. 3, May.

Komjathy, A., Sparks, L., Mannucci, A.J. and Coster, A. (2004) "The ionospheric impact of the October 2003 storm event on WAAS", Proceedings of ION GPS 2004, Long Beach, California.

Lachapelle, G. (2008) *"Advanced GNSS Theory and Application, ENGO 625 Course Notes"*, Department of Geomatics Engineering, University of Calgary, Canada.

Misra, P. and Enge, P. (2006) *"Global Positioning System: Signals, Measurements, and Performance"*, 2nd edition, Ganga-Jamuna Press.

NAV CANADA (2004) "*NAV CANADA website"*, [Online], Available: http://www.navcanada.ca/ [29 June 2011].

Pandya, N., Gran, M. and Paredes, E. (2007) "WAAS Performance Improvement with a New Undersampled Ionospheric Gradient Threat Model Metric", ION 2007 National Technical Meeting, San Diego, CA, 291 - 304.

Rao, G.S. (2010) *"Global Navigation Satellite System"*, Tata McGraw-Hill.

Rao, B.R.K., Sarma, A.D. and Kumar, Y.R. (2006) "Technique to reduce multipath GPS signals", *Current Science*, vol. 90, no. 25, January.

Saastamoinen, I. (1973) "Contribution to the Theory of Atmospheric Refraction", *Bulletin Geodesique*, vol. 107, no. 1, pp. 13-43.

Sakai, T., Matsunaga, K., Hoshinoo, K. and Walter, T. (2008) "Modeling Ionospheric Spatial Threat Based on Dense Observation Datasets for MSAS", *ION GNSS 21st International Technical Meeting of the Satellite Division*, September, pp. 1918 - 1928.

Sakai, T., Matsunaga, K., Hoshinoo, K. and Walter, T. (2008) "Modeling Ionospheric Spatial Threat Based on Dense Observation Datasets for MSAS", *Proceedings of the 21st International Technical Meeting of the Satellite Division of The Institute of Navigation (ION GNSS 2008)*, September, pp. 1918-1928.

Skone, S. (2000) *"TEC Model, Operation Manual"*, 1st edition, Departments of Geomatics Engineering, University of Calgary.

Skone, S. (2009) *"Atmospheric Effects on Satellite Navigation Systems, ENGO 633 Course Notes"*, Department of Geomatics Engineering, University of Calgary, Canada.

Skone, S. and de Jong, M. (2000) "“The impact of geomagnetic substorms on GPS receiver performance"', *Earth Planets Space*, vol. 52, p. 1067–1071.

Skone, S. and Yousuf, R. (2007) "Performance of satellite-based navigation for marine users during ionospheric disturbances", *Space Weather*, vol. 5.

Skone, S., Yousuf, R. and Coster, A. (2004) "Performance Evaluation of the Wide Area Augmentation System for Ionospheric Storm Events", *Journal of Global Positioning Systems*, vol. 3, no. 1-2, pp. 251-258.

Sparks, L., Blanch, J. and Pandya, N. (2010) "Estimation of Ionospheric Delay Using Kriging and its Impact on WAAS Availability", *The International Beacon Satellite Symposium BSS2010, Barcelona*.

Sparks, L., Komjathy, A., Mannucci, A.J., Altshuler, E., Walter, T., Blanch, J., Bakry El-Arini, M. and Lejeune, R. (2005) "Extreme ionospheric storms and their impact on WAAS", *Pasadena, CA: Jet Propulsion Laboratory, National Aeronautics and Space Administration*.

Trauth, M.H. (2006) *"MATLAB® Recipes for Earth Sciences"*, 1st edition, Springer – Verlag Berlin Heidelberg.

U.S. DOT (1999) *"FAA Specification: Wide Area Augmentation System (WAAS)"*, FAA-E-2892B.

USNO (2011) "*The United States Naval Observatory (USNO")* , [Online], Available: ftp://tycho.usno.navy.mil [18 October 2011].

WAAS MOPS (1999) *"Minimum Operational Performance Standards for Global Positioning System/Wide Area Augmentation System Airborne Equipment"*, RTCA Inc. Documentation No. RTCA/DO-229B.

Walter, T. and Enge, P. (2004) "Modernizing WAAS", Proceedings of ION GNSS, Long Beach, CA.

Walter, T., Hansen, A., Blanch, J., Enge, P., Mannucci, T.J., Pi, X., Sparks, L., Iijima, B., El-Arini, A., Lejeune, R., Hagen, M., Altschuler, E., Fries, R. and Chu, A. (2000) "Robust detection of ionospheric irregularities", *Proceedings of the ION GPS, Salt Lake City*.

Walter, T., Rajagobal, S., Datta-Barua, S. and Blanch, J. (2004) "Protecting Against Unsampled Ionospheric Threats", *Beacon Satellite Symposium, Trieste, Italy*.

Wielgosz, P., Cellmer, S., Rzepecka, Z., Paziewski, J. and Grejner-Brzezinska, D.A. (2011) "Troposphere modeling for precise GPS rapid static positioning in mountainous areas", *Meas. Sci. Technol.*, vol. 22, no. 4.

Xu, G. (2007) *"GPS: Theory, Algorithms and Applications"*, 2nd edition, Springer.

Yousuf, R. and Skone, S. (2005) "'WAAS Performance Evaluation under Increased Ionospheric Activity'", *Procedding of ION GPS*.

APPENDIX A: Vertical Protection Level

Beside the GIVE, WAAS also published Protection Levels (PL) indices that used as reliability indicators which are real-time confidence bound on the user's position error.

As mentioned before, our concern in this work is to calculate the VPL to protect the user from potential degradation of the system. The WAAS VPL is computed by the user receiver using a bound of the corrected range measurement error for each satellite contributes to the position solution. VPL can be computed as (WAAS MOPS, 1999)

$$VPL = K_{v,PA} \cdot d_U \tag{A.1}$$

where $K_{v,PA}$ is a multiplier equals to 5.33 and

$$d_U = \sqrt{(G^T W G)^{-1}_{3,3}} \tag{A.2}$$

and

$$(G^T W G)^{-1} = \begin{bmatrix} d_E^2 & d_{EN} & d_{EU} & d_{ET} \\ d_{EN} & d_N^2 & d_{NU} & d_{NT} \\ d_{EU} & d_{NU} & d_U^2 & d_{UT} \\ d_{ET} & d_{NT} & d_{UT} & d_T^2 \end{bmatrix} \tag{A.3}$$

where G is the observation matrix and W is the covariance matrix of the errors formed by the user using the WAAS message given by

$$G_i = [-\cos El_i \sin Az_i \quad -\cos El_i \cos Az_i \quad -\sin El_i \quad 1] \tag{A.4}$$

and

$$W^{-1} = \begin{bmatrix} \sigma_1 & 0 & \cdots & 0 \\ 0 & \sigma_2 & \cdots & 0 \\ \vdots & \vdots & \ddots & \vdots \\ 0 & 0 & \cdots & \sigma_N \end{bmatrix} \tag{A.5}$$

where σ_i^2 is the variance for the satellite i. For each satellite we have

$$\sigma_i^2 = \sigma_{i,flt}^2 + \sigma_{i,UIRE}^2 + \sigma_{i,air}^2 + \sigma_{i,tropo}^2 \tag{A.6}$$

The first term, $\sigma_{i,flt}^2$ (fast and long term) includes the User Differential Range Error, which is the error due the ephemeris and clock error. The second term $\sigma_{i,UIRE}^2$ is User Ionospheric Range Error (UIRE) which is an overbound of the error remaining in the range delay once the ionospheric correction has been applied. The third term ($\sigma_{i,air}^2$) bounds the receiver's thermal noise and multipath errors. The last term ($\sigma_{i,tropo}^2$) is the confidence bound on tropospheric errors.

The following sections show the calculation of satellite variances in the covariance matrix (Jan, 2003).

A.1 Fast and Long Term Degradation Confidence

The fast and long term degradation confidence can be calculated from WAAS message as

$$\sigma_{i,flt}^2 = \begin{cases} \left[(\sigma_{UDRE}) \cdot (\delta UDRE) + \varepsilon_{fc} + \varepsilon_{rrc} + \varepsilon_{ltc} + \varepsilon_{er}\right]^2 & , \quad RSS_{UDRE} = 0 \\ [(\sigma_{UDRE}) \cdot (\delta UDRE)]^2 + \varepsilon_{fc}^2 + \varepsilon_{rrc}^2 + \varepsilon_{ltc}^2 + \varepsilon_{er}^2 & , \quad RSS_{UDRE} = 1 \end{cases} \tag{A.7}$$

where

RSS_{UDRE} is the sum square flag in WAAS Message Type 10.
$\delta UDRE$ is a factor derived from Message Type 27 or 28 and is used to adjust for user location.
ε is the Old But Active Data (OBAD).

A.2 User Ionospheric Range Error Confidence ($\sigma_{i,UIRE}^2$)

This term is calculated based on the interpolated value of the broadcast GIVE term as

$$\sigma_{i,UIRE}^2 = F_{pp}^2 \cdot \sigma_{UIVE}^2 \tag{A.8}$$

where σ_{UIVE}^2 is variance of the residual vertical ionospheric error, and F_{pp} is the obliquity factor.

$$\sigma_{UIVE}^2 = \sum_{n=1}^{j} W_n(x_{pp}, y_{pp}) \cdot \sigma_{n,ionogrid}^2 \tag{A.9}$$

Where j is number of the IGPs surrounding the IPP and $\sigma_{n,ionogrid}^2$ is the variance of the residual error at each IGP and given by

$$\sigma_{n,ionogrid} = \sigma_{GIVE} + \varepsilon_{iono} \tag{A.10}$$

A.3 Local Airborne Receiver's Thermal and Multipath Error Confidence ($\sigma_{i,air}^2$)

This term bounds the receiver's thermal noise and multipath errors which is defined in the Local Area Augmentation System Airborne Accuracy Designator (LAAS ADD) and given by

$$\sigma_{i,air}^2 = \begin{cases} \left(0.16 + 0.23e^{\left(\frac{-E_i}{19.6^o}\right)}\right)^2 & , \quad LAAS\ ADD - A \\ \left(0.0741 + 0.18e^{\left(\frac{-E_i}{27.7^o}\right)}\right)^2 & , \quad LAAS\ ADD - B \end{cases} \tag{A.11}$$

where *Ei* is satellite elevation angle.

The difference between LAAS ADD-A and LAAS ADD-B models is the early-minus-late (EML) correlator spacing for the Delay Locked Loop (DLL) detector in the receiver where EML equals 1 chip and 0.2 chip for LAAS ADD-A and LAAS ADD-B respectively.

A.4 Tropospheric Error Confidence ($\sigma_{i,tropo}^2$)

This term is the tropospheric error confidence, which is the confidence bound on residual tropospheric error. This term is calculated by

$$\sigma_{i,tropo}^2 = [0.12 \cdot m(E_i)]^2 \tag{A.12}$$

The $m(E_i)$ is the tropospheric correction mapping function for satellite elevation E_i given by

$$m(E_i) = \frac{1.001}{\sqrt{0.002001 + \sin^2(E_i)}} \tag{A.13}$$

APPENDIX B: WAAS Interpolation Algorithm

To calculate the ionospheric delay and correction at user's IPP, the user should interpolate the ionospheric corrections from the selected IGPs. Two cases can be arising depending on user's IPP location, four IGPs interpolation and three IGPs interpolation. The following two sections illustrate the interpolation algorithm for both cases.

B.1 Four IGPs interpolation

Figure B.1 below illustrate the algorithm for four IGPs interpolation

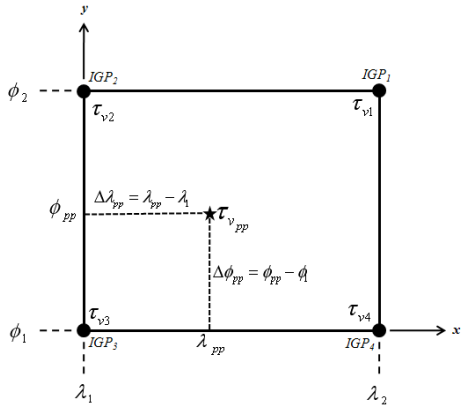

Figure B.1: Four IGPs interpolation algorithm

The formula for interpolating the vertical delay at user's IPP as a function of pierce point latitude and longitude $(\phi_{pp}, \lambda_{pp})$ given by

$$\tau_{v_{pp}}(\phi_{pp}, \lambda_{pp}) = \sum_{i=1}^{4} W_i(x_{pp}, x_{pp}) \cdot \tau_{vi} \quad \text{(B.1)}$$

where the weighting functions given by

$$W_1(x, y) = x \cdot y \quad \text{(B.2)}$$

$$W_2(x, y) = (1 - x) \cdot y \quad \text{(B.3)}$$

$$W_3(x,y) = (1-x)\cdot(1-y) \tag{B.4}$$

$$W_4(x,y) = x\cdot(1-y) \tag{B.5}$$

and

$$x_{pp} = \frac{\Delta\lambda_{pp}}{\lambda_2 - \lambda_1} \tag{B.6}$$

$$y_{pp} = \frac{\Delta\phi_{pp}}{\phi_2 - \phi_1} \tag{B.7}$$

B.2 Three IGPs interpolation

Between -75^o and 75^o latitudes, only three IGPs might be used in the interpolation to calculate the ionospheric correction as shown in Figure B.2 below.

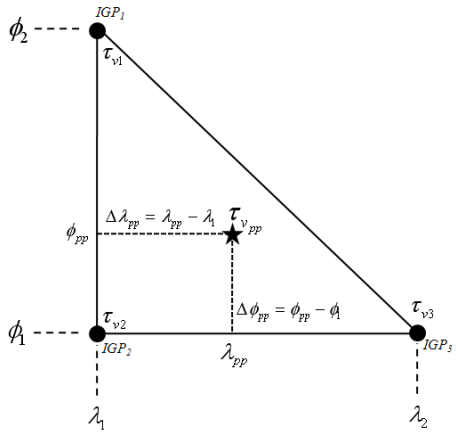

Figure B.2: Three IGPs interpolation algorithm

For this case, the interpolation algorithm used is similar to the four point interpolation algorithm discussed previously. The ionospheric delay at the user's IPP calculated through the following equation

$$\tau_{v_{pp}}(\phi_{pp}, \lambda_{pp}) = \sum_{i=1}^{3} W_i(x_{pp}, y_{pp}) \cdot \tau_{vi} \tag{B.8}$$

where the weighting functions given by

$$W_1(x, y) = y \tag{B.9}$$

$$W_2(x, y) = 1 - x - y \tag{B.10}$$

$$W_3(x, y) = x \tag{B.11}$$

and x_{pp}, y_{pp} given by equations (B.**6**) and (B.**7**) respectively.

Note that there are three more additional orientation of the triangle could be used. When using any of these orientations, IGP_2 must be at the vertex and opposite to the hypotenuse.

APPENDIX C: Lomb-Scargle Algorithm

Power Spectral Density is common analytic technique for describing periodicities in time series. The Lomb-Scargle Algorithm is a technique to obtain the PSD directly from unevenly sampled data series.

Assuming y(t) is a series with N unevenly spaced data points, the Lomb-Scargle periodogram P_x (PSD as a function of angular frequency $\omega=2\pi f > 0$) is defined by (Trauth, 2006)

$$P_x(\omega) = \frac{1}{2\sigma^2}\left\{\frac{\left[\sum_j (y_j - \bar{y})\cos\omega(t_j - \tau)\right]^2}{\sum_j \cos^2\omega(t_j - \tau)} + \frac{\left[\sum_j (y_j - \bar{y})\sin\omega(t_j - \tau)\right]^2}{\sum_j \sin^2\omega(t_j - \tau)}\right\} \quad \text{(C.1)}$$

where

$$\bar{y} = \frac{1}{N}\sum_{i=1}^{N} y_i \quad \text{(C.2)}$$

$$\sigma^2 = \frac{1}{N-1}\sum_{i=1}^{N}(y_i - y_i)^2 \quad \text{(C.3)}$$

And τ is an offset that makes PSD independent of shifting the t_j's by any constant amount.